NIST Technical Note
NIST TN 2314

Global Burning Properties of Little Bluestem, Excelsior and Douglas Fir

Kunhyuk Sung
Eric Mueller
Matthew Bundy
Marco Fernandez
Anthony Hamins

This publication is available free of charge from:
https://doi.org/10.6028/NIST.TN.2314

NATIONAL INSTITUTE OF STANDARDS AND TECHNOLOGY
U.S. DEPARTMENT OF COMMERCE

NIST Technical Note
NIST TN 2314

Global Burning Properties of Little Bluestem, Excelsior and Douglas Fir

Kunhyuk Sung
Eric Mueller
Matthew Bundy
Marco Fernandez
Anthony Hamins
Fire Research Division
Engineering Laboratory

This publication is available free of charge from:
https://doi.org/10.6028/NIST.TN.2314

April 2025

U.S. Department of Commerce
Howard Lutnick, Secretary

National Institute of Standards and Technology
Craig Burkhardt, Acting Under Secretary of Commerce for Standards and Technology and Acting NIST Director

NIST TN 2314
April 2025

NIST Technical Series Policies

NIST Technical Series Publication Identifier Syntax

Publication History
Approved by the NIST Editorial Review Board on 2024-11-13

How to Cite this NIST Technical Series Publication
Sung K, Mueller E, Bundy M, Fernandez M, Hamins A (2025) Global Burning Properties of Little Bluestem, Excelsior and Douglas Fir. (National Institute of Standards and Technology, Gaithersburg, MD), NIST Technical Note (TN) NIST TN 2314. https://doi.org/10.6028/NIST.TN.2314

Author ORCID iDs
Kunhyuk Sung: 0000-0002-0937-2332
Eric Mueller: 0000-0002-0838-6820
Matthew Bundy: 0000-0002-1138-0307
Marco Fernandez: 0000-0002-4227-8866
Anthony Hamins: 0000-0001-7531-4256

Contact Information
anthony.hamins@nist.gov

Abstract

A series of experiments was conducted to better understand the burning characteristics of three types of vegetative fuels: little bluestem grass, excelsior wood fibers, and Douglas fir trees. The measurements included the transient heat release rate (HRR) determined using oxygen consumption calorimetry, the mass loss rate, carbon monoxide (CO) and smoke yields, and the radiative emission to the surroundings. An estimate of the average radiative fraction during the fires was obtained from radiative heat flux measurements made in the far field. Experiments were also conducted on constructed excelsior bundles with controlled bulk density. The measurement results characterize the global combustion properties of the vegetative samples and offer insight into their complex burning behavior. Several key findings are reported:

1. The ratio of the peak heat release rate to the initial mass of the test specimens as a function of their moisture content was consistent with previously published fire measurements on a variety of trees and bushes. A fit to all the data showed that a power law adequately represented the results.
2. The moisture content significantly affected the radiative fraction of the Douglas fir tree fires. The radiative fraction of the Douglas fir tree fires decreased from 0.41 to 0.15 as the dry basis moisture content increased from 7 % to 85 %.
3. The mean radiative fractions for little bluestem, excelsior, and Douglas fir fires were 0.34, 0.33, and 0.29, respectively. Considering the overlapping error bars, there was no statistically significant difference among the fuel types. For the three fuel types, the average radiative fraction was 0.32.
4. The radiative fraction was observed to increase as the fire progressed from the flaming phase to the smoldering phase during the fires, suggesting that the radiative emission from the hot charring solid significantly contributed to the total radiative emission of the fire. For the excelsior fires, this effect became more significant for higher bulk densities.
5. The soot yields had a high degree of scatter with mean values of 0.46 % for bluestem, 0.11 % for excelsior, and 0.24 % for Douglas fir. The CO yields varied as a function of specimen type, with mean values of 6.2 %, 3.3 %, and 8.9 % for bluestem, excelsior, and Douglas fir, respectively. Further work is needed to improve the estimate of the soot yield since it is calculated using a mass-specific extinction coefficient typical of soot and not a value more typical of particulate matter produced during pyrolysis and smoldering combustion.
6. The peak HRR of the excelsior fires was a function of ignition orientation and bulk density. As expected, the upward spreading fires gave rise to larger peak HRRs than those spreading downward.

These measurements of global burning properties can help provide guidance to the development of wildland fire models.

Keywords: burning rate; heat release rate; radiative fraction; vegetation fires.

Table of Contents

List of Tables

List of Figures

Acknowledgments

The authors are grateful to Artur Chernovsky of NIST for outstanding help troubleshooting the data acquisition system used in the experiments described in this report and to Rodney Bryant and Nigel Amoafo-Yeboah for helpful discussions regarding the cumulative radiative fraction.

1. Introduction

According to the National Fire Protection Association (NFPA), more than half the fires reported in the USA in 2022 were outside fires, including brush, grass or wildland fires [1]. Fourteen of the 20 costliest wildland fires in the USA have occurred over the last 10 years [2]. These large fires threaten homes and communities, and research is ongoing to better understand the fire hazard.

The main objective of this study was to better understand the character of burning vegetative fuels, which is important to better understand fire hazards and to help guide and validate computational fire models of outdoor fire spread. The intensity of a fire is an important parameter for the classification of wildfire hazards. The fire heat release rate has a significant role in the spread rate of a fire, which is related to the heat and mass transfer processes that occur during burning. Wildfires emit significant amounts of carbon monoxide (CO), carbon dioxide (CO_2), and smoke, which can impact people's health far downstream of the fire. An understanding of the heat release rate of a fire and the yields of toxic combustion products is needed to better understand the impact of fire on human health.

In addition to these impacts, global burning properties are often used in Computational Fluid Dynamics (CFD) models such as the Fire Dynamics Simulator (FDS) when more detailed modeling approaches are not feasible or practical. These include a radiative fraction to correct radiative emissions from the flaming region and fixed CO and soot yields for the homogenous combustion reaction [9]. Specific values may not be available for a vegetation type of interest, so it is important to understand their range of variability as a function of plant structure and composition and the uncertainty for a single value.

The fuels selected for the study include little bluestem grass, Douglas fir trees, and constructed excelsior bundles oriented vertically or horizontally. These are three very different types of fuels in terms of their appearance. Little bluestem was selected for study as it is an important species in terms of grass-fuel fires in Texas [3-7]. Excelsior is the name given to thin strands of wood produced by shaving aspen trunks, which is often used as a packing material for fragile items. Use of excelsior can be found across wildland fire literature as it allows testing of the importance of fuel bed geometry and bulk density on the burning behavior of a thin cellulosic fuel - something that is not easily accomplished in a systematic way with natural plants [5-7]. Douglas fir is a common evergreen conifer that is easily attainable year-round and has also been used in previous studies of vegetation burning dynamics[8, 9]. Several other vegetative fuel types important to fire hazard in various regions of the country were considered for this study, such as chaparral from the western USA and saw palmetto from Florida, but they were simply not easily attainable due to cost and the availability of shipping.

This report is broken into several sections. The remainder of this introduction briefly reviews previous studies on burning the vegetative specimens tested here. Section 2 describes the experimental apparatus and methods, including the ignition method, a list of the test specimens, and the measurement methods for the moisture content, peak flame height, and CO and soot yields. Section 3 presents the experimental results, including the mass loss, the heat release rate, peak flame height, the yields of CO and soot, and an estimate of the radiative fraction. Section 4 summarizes the experimental results. Section 5 presents the references cited in this report. Appendix A presents details on the test, including the load cell type, the exhaust hood size, the heat flux gauge locations, and the camera settings. Appendix B presents uncertainty analyses of the mass loss, heat flux, and flame height measurement for each of the tests. Appendix C lists the values of the CO and soot yields, and Appendix D presents plots of the transient heat release rate, radiative heat flux, and light extinction coefficient for each of the tests.

The measurement results in this report are available as part of the NIST Fire Calorimetry Database (FCD)[10]. The FCD contains hundreds of measurement results of fire experiments conducted since 2017 at NIST's National Fire Research Laboratory (NFRL) and is used by fire scientists and fire protection engineers to support engineering analysis, including performance-based design. Measurement results included in the FCD include the transient and peak heat release rates, the total heat released, the yields of CO and soot, the initial and final specimen mass as well as a video record of the experiments. The information provided in the FCD for each dataset includes a summary of the measurement results, their uncertainty, and the experimental test conditions. The data generated from this study will be included in the FCD, which will link to this report.

1.1. Previous Studies

Although many studies of vegetation burning focus on spread rates in homogenous fuel beds, some have provided global burning properties for individual plants, including similar vegetation types to those tested here. Mell et al. [9] measured the mass loss and radiative emission from 2 m to 5 m tall Douglas fir trees. The study investigated how various factors, such as moisture content (MC) and environmental conditions, affect the heat release rate. Completeness of the burning of Douglas fir differed according to three ranges of moisture content (on a dry basis): MC_{dry} < 30 %, 30 % < MC_{dry} < 70 %, and MC_{dry} > 70 %, with the lowest moisture content trees burning well and the high moisture content trees not burning at all [11]. The results revealed that higher moisture levels significantly reduced the fire heat release rate, underscoring the importance of moisture content in wildfire management. Schneider et al. [8] tested the ability of Douglas fir trees to ignite by radiation from adjacent burning trees. They measured mass loss rates and local heat fluxes and found that moisture content affected the ignition propensity. Various studies have looked at the heat release rate of dry Christmas trees, showing that keeping a tree watered is important to reduce fire risk [12].

Overholt et al. [3, 4] measured the mass loss rate of burning single and multiple little bluestem plants in a compartment. The near-field radiative emission was also measured. The experimental results were utilized to establish input parameters for a field-scale numerical simulation of a grassland using a physics-based computational fire model. A sensitivity analysis assessed how input parameters influenced the calculated fire spread rate, revealing that the fuel's moisture content had the greatest effect on the rate of fire spread.

Babrauskas [13] surveyed several previous experimental studies on burning vegetation. Compiling results for many types of shrubs and trees showed a correlation between the ratio of the peak heat release rate to the specimen mass and the foliar moisture content.

In this study, a series of measurements were conducted to characterize the burning behavior of three vegetative types, namely, a grass (little bluestem), a tree (Douglas fir), and dry excelsior, including the mass loss rate, the yields of CO and smoke, the radiative emission to targets, and the average radiative fraction. The experiments were conducted under controlled laboratory conditions. Measurements were made of the transient heat release rate (HRR) determined using oxygen consumption calorimetry, the mass loss, and the radiative flux to targets away from the fire.

2. Experimental Methods

Fire experiments were conducted on little bluestem and Douglas fir trees and constructed excelsior bundles oriented vertically or horizontally. The experiments were conducted below the NFRL's 6 m × 6 m and 3 m × 3 m canopy exhaust hoods and calorimeters, which are described in detail by Bryant and Bundy [14].

Figure 1 shows a schematic diagram of the experimental setup under the 6 m x 6 m canopy hood. The experimental area defined by the perimeter of the canopy hoods was surrounded by a cubic enclosure made of a double-layered, fine wire mesh screen (6 mesh/cm with 83 % porosity) to reduce the impact of air currents and room ventilation. In addition, all makeup air inlet vents in the lab were closed, further reducing the effect of ambient convective currents on the fire. A large, round exhaust duct with a 0.5 m diameter was located 4.1 m above the floor. The minimum exhaust flow (approximately 1 kg/s) was utilized to minimize disturbances and reduce the influence of the exhaust on fire behavior. The radial direction (*r*) is referenced from the center line of the specimen. The vertical direction (*z*) is referenced from the top of the specimen holder for Douglas fir and little bluestem and from the bottom of the specimen for excelsior. Details on the experimental setup for heat flux gauges can be found in Section 2.7.

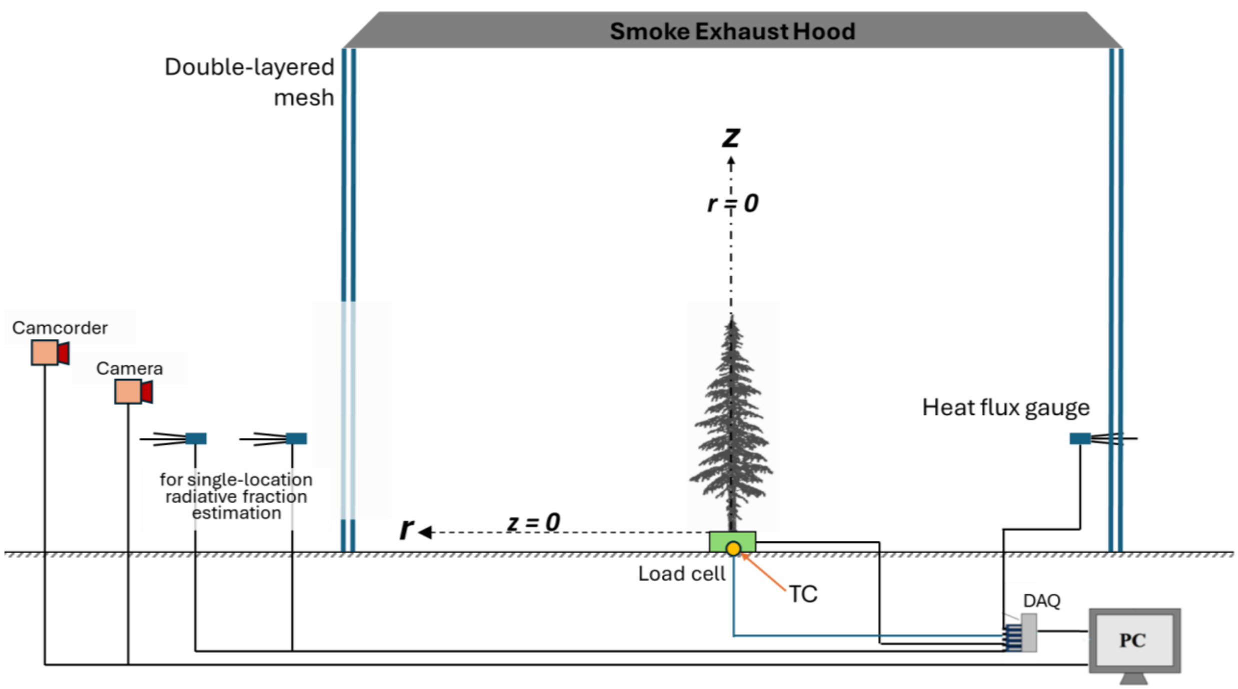

Fig. 1. A schematic diagram of the experimental setup under 6m x 6m exhaust hood.

The mass burning rate was measured using calibrated loadcells. The load cell's core temperature was measured using a K-type thermocouple to correct the mass drift due to temperature changes as described in Appendix B.1. A dry gypsum board (2 cm thick) was placed between the load cell and the specimen holder to reduce heat transfer from the fire to the load cells. Two cameras (typically a Nikon 500D and a Canon XA45) recorded the fire at 30 frames/sec. Appendix A provides supplementary details about the tests, including the load cell type, the exhaust hood size, the heat flux gauge locations, and the camera settings.

2.1. Preparation of Test Specimens

Figure 2 shows the photographs of the three types of vegetative specimens investigated in this study, which included little bluestem grass, Douglas fir trees, and excelsior. The specimens were stored in the lab until tested. The mass and moisture content (see Section 2.3) were measured before testing. The dimensions, initial (wet) mass, and moisture content of specimens are listed in Table 1. The specimens were mounted on the load cell using different methods to ensure their proper placement, which was a function of the vegetative type and the specimens' dimensions and weight.

Fig. 2. Photographs of plants before experiments: little bluestem (left), excelsior (middle), Douglas fir (right).

Table 1. Specimen dimensions, initial (wet) mass, and dry basis moisture content. The direction of flame spread is listed for the excelsior fires.

Test	Specimen	Height (cm)	Base Width (cm)	Initial (Wet) Mass (g)	Moisture Content Dry Basis (%)	Bulk Density[b] (kg/m^3)
little bluestem						
1	bluestem	80	11	85	6	na
2	bluestem	110	11	72	6	na
3	bluestem	122	11	104	6[a]	na
4	bluestem	90	11	36	6[a]	na
5	bluestem	73	11	26	6	na
6	bluestem	89	11	21	6[a]	na
24	bluestem	107	11	81	10[a]	na

Test	Specimen	Height (cm)	Base Width (cm)	Initial (Wet) Mass (g)	Moisture Content Dry Basis (%)	Bulk Density[b] (kg/m³)
25	bluestem	75	11	84	10[a]	na
28	bluestem	35	11	53	10	na
29	bluestem	75	11	103	10[a]	na
30	bluestem	71	11	29	10[a]	na
33	bluestem	50	11	53	10[a]	na
34	bluestem	40	11	56	10[a]	na
Douglas fir						
12	Douglas fir	123	21	355	16[a]	na
13	Douglas fir	94	44	298	15	na
14	Douglas fir	105	60	326	19	na
22	Douglas fir	102	70	284	8	na
23	Douglas fir	103	66	575	19	na
37	Douglas fir	120	50	522	75	na
38	Douglas fir	120	80	336	8	na
39	Douglas fir	113	70	551	35	na
40	Douglas fir	103	25	193	23	na
41	Douglas fir	120	45	733	85	na
42	Douglas fir	120	45	515	67	na
43	Douglas fir	110	70	615	6	na
44	Douglas fir	179	154	7551	10[a]	na
45	Douglas fir	146	128	5119	10	na
46	Douglas fir	146	128	6688	10	na
47	Douglas fir	146	128	5419	11	na
excelsior fires spreading upward						
9	excelsior	60	15	146	6	14
15	excelsior	60	15	149	6[a]	14
16	excelsior	60	15	66	6[a]	6
17	excelsior	60	15	57	6[a]	5
21	excelsior	60	15	59	6[a]	6
26	excelsior	60	15	148	6[a]	14
27	excelsior	120	15	267	6[a]	13
35	excelsior	60	15	95	6[a]	9
36	excelsior	120	15	124	6[a]	6
48	excelsior	60	15	148	6[a]	14
49	excelsior	60	15	146	6[a]	14
50	excelsior	60	15	202	6[a]	19
51	excelsior	60	15	212	6[a]	20
52	excelsior	60	15	205	6[a]	19
56	excelsior	60	15	28	6[a]	3
excelsior fires spreading horizontally						
31	excelsior	15	60	153	6[a]	14

Test	Specimen	Height (cm)	Base Width (cm)	Initial (Wet) Mass (g)	Moisture Content Dry Basis (%)	Bulk Density[b] (kg/m³)
32	excelsior	15	60	152	6[a]	14
excelsior fires spreading downward						
7	excelsior	60	15	143	6	13
8	excelsior	60	15	147	6	14
10	excelsior	60	15	148	5	14
11	excelsior	60	15	157	6	15
18	excelsior	60	15	59	6[a]	6
19	excelsior	60	15	61	6[a]	6
20	excelsior	60	15	58	6[a]	5
53	excelsior	60	15	225	6[a]	21
54	excelsior	60	15	212	6[a]	20
55	excelsior	60	15	204	6[a]	19

[a] Estimated.

[b] the excelsior specimens were assumed to be cylindrical (see Fig. 2).

The excelsior shavings were relatively dry, approximately cylindrical, and slender, with a 0.6 mm average diameter. The excelsior arrived in assorted lengths (1 cm to 20 cm long), all jumbled and twisted together. The excelsior specimens were strung about a metal skeleton composed of a long central vertical rod with small diameter (1 mm) steel rods threaded through the central rod in perpendicular pairs every 10 cm, starting about 60 cm above a small stand. The bulk shape of the excelsior specimen was approximately cylindrical with radii of about 7.5 cm and 60 cm in length, following the design of Ref. [6]. The excelsior specimens were arranged with different bulk porosities, which, by design, were approximately uniform over their entire length as their structure was crafted in short regular segments with the same mass loading. The excelsior specimens were “sculpted” to cover a range of bulk densities from about 5 kg/m^3 to 20 kg/m^3.

The little bluestem plants were stored until uniformly dry. A single plant comprised about 40 to 100 strands of about the same length. The strands were somewhat round, with a diameter of about 1 mm. Specimens of little bluestem were placed into an 11 cm (inner diameter, 0.25 cm wall) aluminum pipe 10.5 cm tall with the bottom end capped. The space between the roots and the holder was filled with sand. The stems of the plants were fixed using a metal wire and two vertical rods, as seen in Fig. 2. Different numbers of strands were placed in the aluminum holder, giving rise to differing initial masses. The specimens’ height was measured from the top of the specimen holder or stand to the specimen tip. The little bluestem varied in height from about 0.4 m to 1.2 m and in mass from 26 g to 104 g. The plants were dry, and the dry basis moisture content varied little, ranging from about 6 % to 9 %.

A wide range of Douglas fir trees was tested, varying from about 0.9 m to 1.8 m in height and 200 g to 6700 g in mass. The dry basis moisture content ranged from 7 % to 85 %. The shapes of the Douglas fir trees were irregular but could be idealized as conical.

2.2. Ignition Method

The ignition protocol varied among the tests. Six types of ignitor burners were used:

(A) A double-tipped propane wand made of ¼” (6.4 mm) outer diameter copper tubing with the tips separated by 5 cm to 10 cm, depending on fuel geometry; see Fig. 3. The propane flow was controlled by a rotameter (Dwyer model: # VA 20430).

(B) A single-tipped propane wand made with ¼" (6.4 mm) outer diameter copper tubing. The propane flow was controlled by a rotameter (Dwyer model # VA 20430).

(C) A U-shaped multi-port propane burner with 1 mm holes every 2.5 cm about the “U”. There was a separation of 10 cm between tips. The propane flow was controlled by a rotameter (Dwyer model # VA 20430).

(D) An 32’’ (81 cm) diameter ring burner comprised ¼ inch outer diameter copper tubing with 1 mm holes every 2.5 cm about the ring, as seen in Fig. 3. A rotameter (Dwyer model # VA 20430) controlled the propane flow.

(E) A measured amount of (100 % purity) ethanol decanted onto a circle of thin (1 mm) and 1 cm wide Kaowool sheet, forming a circle approximately 15 cm in diameter. A thin metal mesh (4 mesh/cm) was used to support the Kaowool sheet, as seen in Fig. 3.

(F) A near circular, 30” x 34” (76 cm x 86 cm) ring burner composed of two semi-circles of ½ inch (12.7 mm) outer diameter copper tubing with 2 mm holes every 4 cm. The propane flow was set by a mass flow controller (Alicat MC-series). The burner was positioned several cm above the gypsum board, which insulated the load cell, as seen in Fig. 3.

Figure 3 shows photographs of type A, D, E, and F ignitors. Table 2 lists the ignitor type (A – F), application location, ignitor power during the application, duration of the ignitor application, and the total ignitor energy applied to the specimen (equal to the product of the ignitor’s power and its duration). The associated expanded uncertainties for each experiment are also listed, representing a coverage factor of two and a 95 % confidence interval. The ignition energy was small compared to the specimen's heat release rate.

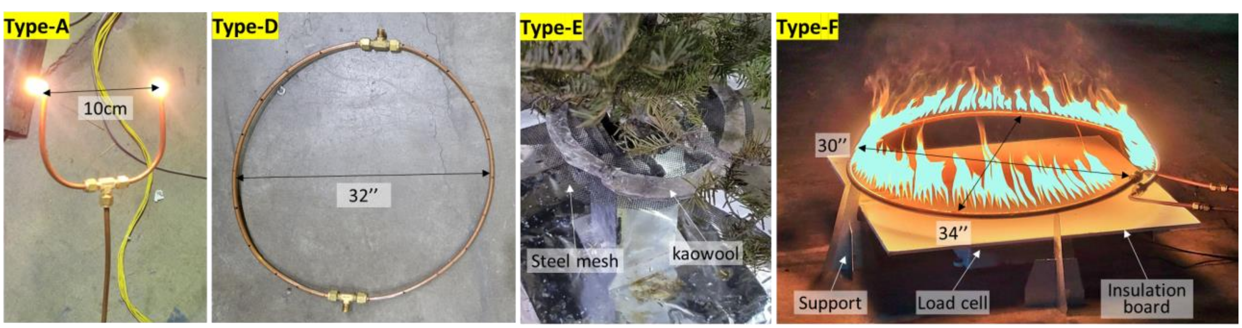

Fig. 3. Photographs of four of the ignitors used in the experiments. Ignitor types (A), (D), (E), and (F) are shown from left to right, respectively.

Table 2. Ignitor type, application location, power, duration, and total energy. The uncertainty listed represents the combined expanded (k=2) uncertainty, representing a 95 % confidence interval.

Test	Specimen	Ignitor	Ignition location	Ignition Power (W)	Ignitor duration (s)	Igniter Energy (kJ)
little bluestem						
1	bluestem	A	Bottom	114 ± 27	25.0 ± 0.5	2.08 ± 0.5
2	bluestem	B	Bottom	128 ± 19	3.0 ± 0.5	0.38 ± 0.1
3	bluestem	B	Bottom	128 ± 19	4.0 ± 0.5	0.51 ± 0.1
4	bluestem	B	Bottom	128 ± 19	3.0 ± 0.5	0.38 ± 0.1
5	bluestem	B	Bottom	128 ± 19	2.0 ± 0.5	0.26 ± 0.1
6	bluestem	B	Bottom	128 ± 19	2.0 ± 0.5	0.26 ± 0.1
24	bluestem	B	Bottom	128 ± 19	1.0 ± 0.5	0.13 ± 0.1
25	bluestem	B	Bottom	128 ± 19	1.0 ± 0.5	0.13 ± 0.1
28	bluestem	B	Bottom	128 ± 19	2.0 ± 0.5	0.26 ± 0.1
29	bluestem	B	Bottom	128 ± 19	1.0 ± 0.5	0.13 ± 0.1
30	bluestem	B	Bottom	128 ± 19	1.0 ± 0.5	0.13 ± 0.1
33	bluestem	B	Bottom	128 ± 19	1.0 ± 0.5	0.13 ± 0.1
34	bluestem	B	Bottom	128 ± 19	1.0 ± 0.5	0.13 ± 0.1
Douglas fir						
12	DF tree	C	Bottom	128 ± 19	15.0 ± 0.5	1.9 ± 0.3
13	DF tree	D	Bottom	988 ± 20	16.0 ± 0.5	15.8 ± 0.6
14	DF tree	C	Bottom	128 ± 19	7.0 ± 0.5	0.9 ± 0.2
22	DF tree	E [a]	Bottom	na	na	137 ± 27
23	DF tree	E [b]	Bottom	na	na	158 ± 25
37	DF tree	E [d]	Bottom	na	na	317 ± 6
38	DF tree	E [d]	Bottom	na	na	317 ± 6
39	DF tree	E [d]	Bottom	na	na	317 ± 6
40	DF tree	E [e]	Bottom	na	na	276 ± 6
41	DF tree	C	Bottom	988 ± 20	30.0 ± 0.9	30 ± 1.2
42	DF tree	E [d]	Bottom	na	na	317 ± 6
43	DF tree	E [d]	Bottom	na	Na	317 ± 6
44	DF tree	F	Bottom	30000 ± 600	10.0 ± 0.5	300 ± 15
45	DF tree	F	Bottom	30000 ± 600	5.0 ± 0.5	150 ± 15
46	DF tree	F	Bottom	30000 ± 600	5.0 ± 0.5	150 ± 15
47	DF tree	F	Bottom	30000 ± 600	5.0 ± 0.5	150 ± 15
excelsior fires spreading upward						
9	excelsior	A	Bottom	128 ± 19	2.0 ± 0.5	0.26 ± 0.1
15	excelsior	A	Bottom	128 ± 19	2.0 ± 0.5	0.26 ± 0.1
16	excelsior	A	Bottom	128 ± 19	1.0 ± 0.5	0.13 ± 0.1
17	excelsior	A	Bottom	128 ± 19	1.0 ± 0.5	0.13 ± 0.1
21	excelsior	A	Bottom	128 ± 19	1.0 ± 0.5	0.13 ± 0.1
26	excelsior	A	Bottom	128 ± 19	1.0 ± 0.5	0.13 ± 0.1
27	excelsior	A	Bottom	128 ± 19	1.0 ± 0.5	0.13 ± 0.1

Test	Specimen	Ignitor	Ignition location	Ignition Power (W)	Ignitor duration (s)	Igniter Energy (kJ)
35	excelsior	A	Bottom	128 ± 19	1.0 ± 0.5	0.13 ± 0.1
36	excelsior	A	Bottom	128 ± 19	1.0 ± 0.5	0.13 ± 0.1
48	excelsior [f]	A	Bottom	150 ± 45	1.0 ± 0.5	0.15 ± 0.1
49	excelsior [f]	A	Bottom	150 ± 45	1.0 ± 0.5	0.15 ± 0.1
50	excelsior	B	Bottom	128 ± 19	1.0 ± 0.5	0.13 ± 0.1
51	excelsior	B	Bottom	128 ± 19	1.0 ± 0.5	0.13 ± 0.1
52	excelsior	B	Bottom	128 ± 19	1.0 ± 0.5	0.13 ± 0.1
56	excelsior	B	Bottom	128 ± 19	1.0 ± 0.5	0.13 ± 0.1
excelsior fires spreading horizontally						
31	excelsior [c]	A	Right Bot	128 ± 19	1.0 ± 0.5	0.13 ± 0.1
32	excelsior [c]	A	Right Bot	128 ± 19	1.0 ± 0.5	0.13 ± 0.1
excelsior fires spreading downward						
7	excelsior	A	Top	128 ± 19	2.0 ± 0.5	0.26 ± 0.1
8	excelsior	A	Top	128 ± 19	3.0 ± 0.5	0.39 ± 0.1
10	excelsior	A	Top	128 ± 19	2.0 ± 0.5	0.26 ± 0.1
11	excelsior	A	Top	128 ± 19	5.0 ± 0.5	0.64 ± 0.1
18	excelsior	A	Top	128 ± 19	1.0 ± 0.5	0.13 ± 0.1
19	excelsior	A	Top	128 ± 19	2.0 ± 0.5	0.26 ± 0.1
20	excelsior	A	Top	128 ± 19	2.0 ± 0.5	0.26 ± 0.1
53	excelsior	B	Top	128 ± 19	2.0 ± 0.5	0.26 ± 0.1
54	excelsior	B	Top	128 ± 19	2.0 ± 0.5	0.26 ± 0.1
55	excelsior	B	Top	128 ± 19	2.0 ± 0.5	0.26 ± 0.1

[a] 5.1 g of Ethanol was evenly applied onto the kaowool board.
[b] 5.9 g of Ethanol was evenly applied onto the kaowool board.
[c] The excelsior in Tests 31 and 32 were oriented horizontally.
[d] 11.8 g of Ethanol was evenly applied onto the kaowool board.
[e] 10.8 g of Ethanol was evenly applied onto the kaowool board.
[f] Twin vertical excelsior "trees" were placed 15 cm apart and tested – only one burned, which is attributed to convective currents in the lab. Radiation from the first "tree" was insufficient to ignite the second one.

For the excelsior and little bluestem experiments, ignition was atypically achieved using ignitor type (A). Ignitor type (B) was used in one experiment (Test 1). The ignitor flames for the excelsior and bluestem experiments were set to approximately 1 cm in length. A rotameter was used to measure the ignitor power, which was typically 133 W. The propane ignitors were lit about 25 s before ignition of the specimen. For ignition using Ignitor type (A), the propane wand was simultaneously applied to two sides of the specimen, typically on its bottom. About one-third of the excelsior fire experiments were conducted igniting the top of the specimen as noted in Table 2. In Tests 7 and 8, the excelsior was positioned horizontally with ignition on the bottom of one end.

For the excelsior and little bluestem burns, the simple propane U-tipped ignitor C was adequate to achieve uniform burning of the specimen. Depending on the tree size, several ignition methods were tested for the Douglas fir tree experiments. For trees larger than about 1.3 m in height, ignitor type F was used. For trees less than about 1.3 m in height, ignitor types B, C, D, and E were used. The methods endeavored to ignite all sides near the specimen's bottom simultaneously. For the Douglas fir trees, symmetric ignition was not always achieved. In those few tests, the fire spread upward on one side of the tree before the other burned, obstructing some heat flux gauges.

2.3. Moisture Content Measurements

The moisture content of the specimens (on a wet basis) was measured using a moisture instrument (Arizona Instruments, Computrac Max 4000) before the burn experiments. One-gram to three-gram samples of needles and stems were collected on the test day. The moisture analyzer was programmed to run at a temperature of 110°C, with the criteria to end the moisture analysis defined as a mass rate of change of the sample of less than 0.02 %/min. The termination criteria were conservative, and tests with a more stringent (lower) rate of change termination criteria showed no discernable difference for tests using the same sample batch.

Calibration of the moisture analyzer was evaluated and found to be better than 2 % based on comparison experiments using an oven (at the same oven temperatures of 110 °C) and a precision scale (Sartorius Balance Model #GW6202) for the same sample foliage batch. Measurements using the analyzer showed a high level of repeatability (better than 2 %) for the same sample batch. The analyzer outputs the moisture content on a wet basis percentage (MC_{wet}). Measurements were then converted to a dry basis percentage using the following equation:

$$MC_{dry} = 100\ MC_{wet}/(100 - MC_{wet}) \tag{1}$$

Table 1 lists the mean dry basis moisture content value for each tree, along with its combined expanded uncertainty. The moisture content of the specimens (on a dry basis) varied from 5 % to 85 %. Table 1 shows that many samples were relatively dry, representing a worst-case condition regarding the fire's growth rate and peak heat release rate.

2.4. Heat Release Rate Measurements

The HRR of the fires was measured using the NFRL calorimetry systems. A gas sample was extracted from the exhaust hood flow, and paramagnetic O_2 measurements and non-dispersive infrared measurements of CO and CO_2 were conducted. The time response of the calorimetry system is on the order of 8 s [14]. Details about the oxygen consumption calorimetry measurement method, its calibration, and measurement uncertainty are documented in Ref. [14].

2.5. Peak Flame Height Measurements

Flame appearance was captured using a camera (Canon XA40, Canon XA45, Nikon D500) at 30 frames/sec. The video record of the flame appearance was converted to 8-bit images. The flame region was extracted from the background in each frame, considering the threshold suggested by Otsu [15], and the images were transformed into binary images.

The flame height in each frame, defined as the vertical extent of the entire visible flaming region, was corrected for image distortion caused by parallax effects due to the camera's viewing angle and position. Small, isolated regions (<500 pixels) above the intensity threshold were assumed to correspond to burning embers and were automatically filtered out of the calculation. Figure 4 shows the RGB (left) and processed binary image (right) of a fire taken from the video record of the little bluestem fire. The yellow vertical line in the binary image represents the flame height, excluding the burning embers.

Every frame extracted in the video record was analyzed using MATLAB to determine the flame height. A 1-second moving average was applied to estimate flame height changes over time. The peak flame height was defined as the average over 1 second centered at the peak of the moving average. The standard deviation of the flame height in the period is attributed to flame puffing. The average flame height uncertainty was 9 % across all tests.

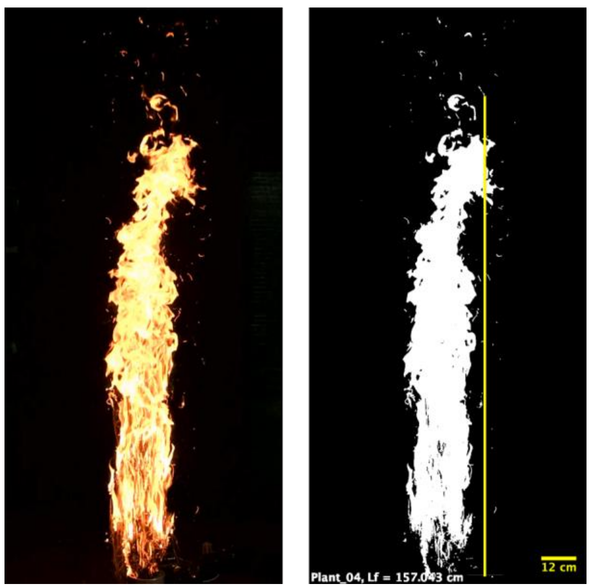

Fig. 4. The RGB (left) and processed binary image (right) of a fire taken from the video record of the little bluestem fire and the determination of the peak flame height. The yellow vertical line in the binary image represents the peak flame height.

2.6. CO and Soot Yields Measurements

Bryant and Bundy [14] describe the CO and CO_2 gas analysis measurement system, which is part of the calorimetry system. Gas was extracted from the exhaust duct stream, and the transient concentrations of CO and CO_2 were measured using non-dispersive infrared analyzers.

From the velocity and temperature measurements made in the exhaust stream, the total transient exhaust mass flow rate was determined as a function of time. The species yields are the ratio of the integrated value of the transient species mass flows to the change in the specimen mass over the duration of the experiment. A detailed discussion on the determination of the species measurements and the yield calculations is provided in Refs. [14] and [16]. The steady-state CO concentration was determined via extractive sampling and non-dispersive infrared (NDIR) measurements.

The steady-state soot mass fraction was measured in the duct using laser transmission at 632 nm using a Si photodiode detector. The light extinction coefficient, *K*, is defined as:

$$K = \frac{1}{D}\ln\left(\frac{I_0}{I(t)}\right) = \sigma_s M_s \tag{2}$$

where *D* is the exhaust duct diameter, I_0 is the laser reference intensity (determined over a 60 s period before ignition), and *I(t)* is the transient attenuated laser intensity during the fire [17, 18]. The light extinction coefficient, *K,* is equal to the product of the mass-specific extinction coefficient, σ_s, and the mass concentration of smoke, M_s. Mulholland and Croarkin [18] posit that the value of σ_s at 632 nm is nearly universal for post-flame soot equal to 8.7 m^2/g ± 1.1 m^2/g, where the error bounds represent the expanded (k=2) uncertainty (confidence interval of 95 %). Using the average value from seven studies, the soot yield here is determined by integrating the effective volume flow in the exhaust duct and application of the mass-specific extinction coefficient in Eq. (2) [17]. The assumption in the soot yield determination is that the value of σ_s for an aerosol emitted from a smoldering fire is the same as that of soot. Seader and Einhorn [19] find that σ_s for a smoldering aerosol from a variety of different materials, including wood, is about a factor of 0.58 smaller than its flaming analog, yielding a σ_s value of about 5 m^2/g. The practical challenge is that σ_s may be transient as a fire (or a portion of a burning solid) transitions from flaming to smoldering and back to flaming. Furthermore, the aerosols from these fuels may include un-combusted pyrolysis species, which are not the same as products of combustion (either flaming or smoldering). For simplicity and consistency, the soot yield reported here and in the FCD uses Mulholland's value of σ_s =8.7 m^2/g ± 1.1 m^2/g. The actual particulate matter in the fire plume was not sampled and analyzed as part of this study. It should be understood that solid phase matter that can affect the "soot" yield are decomposition products due to a time varying combination of flaming, smoldering, and pyrolysis.

2.7. Heat Flux Measurements

The radiative heat flux emitted to the surroundings was measured using wide-view angle (150°), water-cooled, Gardon-type, total heat flux gauges with faces that were 1.3 cm in diameter. Multiple gauges were used to measure the fire's heat flux distribution according to the smoke exhaust hood's size, as shown in Fig. 5.

The radial direction (*r*) is the distance from the centerline of the specimen. The vertical direction (*z*) is referenced from the top of the specimen holder for Douglas fir and little bluestem and from the bottom of the specimen for excelsior. The azimuthal angle (θ) is referenced to the middle of the opening of the double-layered mesh screen, as seen in Fig. 5, and is taken as positive in the counter-clockwise (CCW) direction. The gauge locations were selected based on laboratory confines and fire size. The locations of the gauges are listed in

Table A1. Heat flux gauges were aligned horizontally to measure the heat flux in the radial direction away from the fire at various angles from the specimen and for positions at *r/D* > 5. Additionally, both horizontal and vertical arrays of heat flux gauges were placed under a 3 m x 3 m hood to measure local heat flux distribution. A schematic and further details are available in Appendix B.3.1. The gauges were calibrated using a secondary standard in NIST's radiometer heat flux calibration facility. Voltage signals from the gauges were acquired at 1 Hz and time averaged. The measured heat flux was corrected considering the background heat flux from the surroundings, as described in Ref. [20].

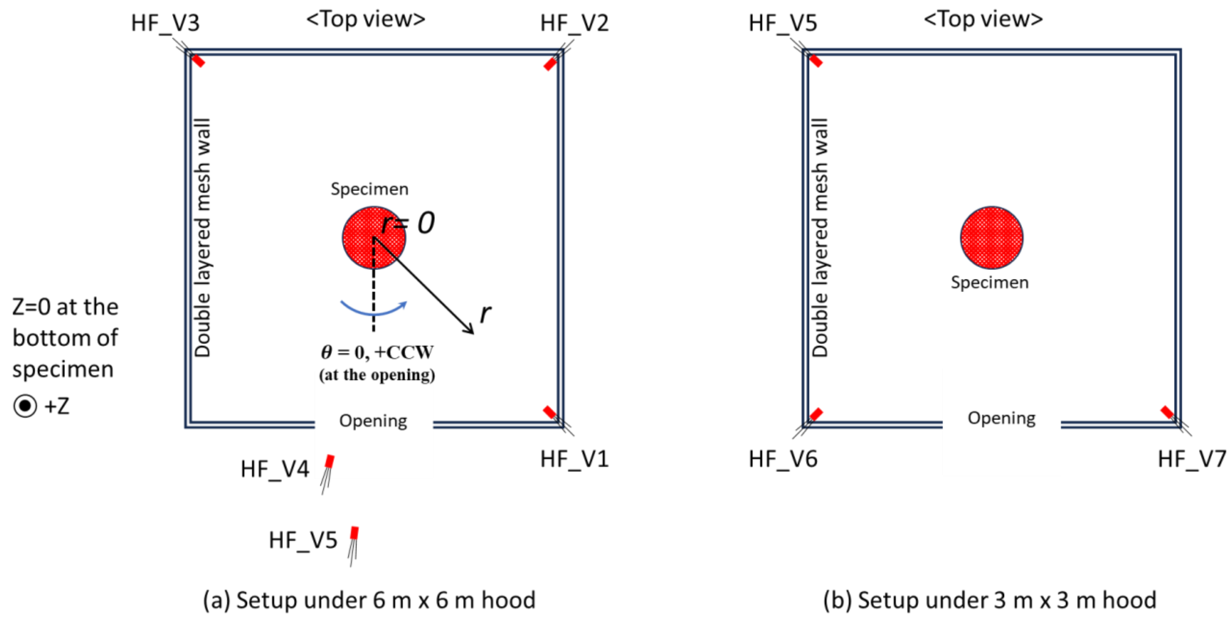

Fig. 5. Schematic diagrams of the heat flux gauge setup: (a) under the 6 m x 6 m exhaust hood. Three to five heat flux gauges were positioned at different angles about the fire; (b) under the 3 m x 3 m exhaust hood.

The radiative fraction was estimated using this approach following Modak [21], where an adequate estimate of the radiative fraction of a pool fire is sufficient for distances greater than 5 times the fire's diameter. Here, fire symmetry and radiative isotropy are assumed.

The fraction of energy radiated from the fire, χ_{rad}, is related to the overall enthalpy balance:

$$\chi_{rad} = Q_{rad}/Q \tag{3}$$

where the term Q is the heat release from the fire defined as:

$$Q = \Delta m\, H_{c,eff} \tag{4}$$

where Δm is the burning mass loss (assuming that the moisture content of unburned fuel is the same as its initial value before the fire), and $H_{c,eff}$ is the mean effective heat of combustion for each specimen type as listed in Table 3. Details are discussed in Section 3.1.

In Eq. (3), Q_{rad} represents the total radiative emission (TRE) from the fire, estimated by averaging TRE_i measured in multiple directions. Here, TRE is calculated using three to five heat flux gauges directed toward the fire from different angles (see Fig. 5). The TRE_i is the time integral of the radiative heat flux measured at suitably far distances from the fire. At the i^{th} heat flux gauge during the burning period, TRE_i during the burning period is calculated as:

$$TRE_i = 4\pi r^2 \int_{t_0}^{t_e} \dot{q}_i''\,(t)\,dt \tag{5}$$

where $\dot{q}_i''(t)$ is the radiative heat flux measured at a radial distance (r) from the fire. t_0 and t_e are the ignition and fire extinguishment times, respectively.

The burning periods were relatively short (< 4 min) for all the fires. The mean burning periods for the little bluestem, Douglas fir, and excelsior fires were 150 s, 200 s, and 120 s, respectively. The mass loss rate and heat flux change were not steady during the burning period. As an example, Figure 6 shows the total specimen (plus stand) mass as well as the heat flux measured at (r, z) = (2.14 m, 0.95 m) as a function of time in Test 9 for an excelsior specimen. Both the slope of the mass loss rate and the heat flux significantly changed during the fire.

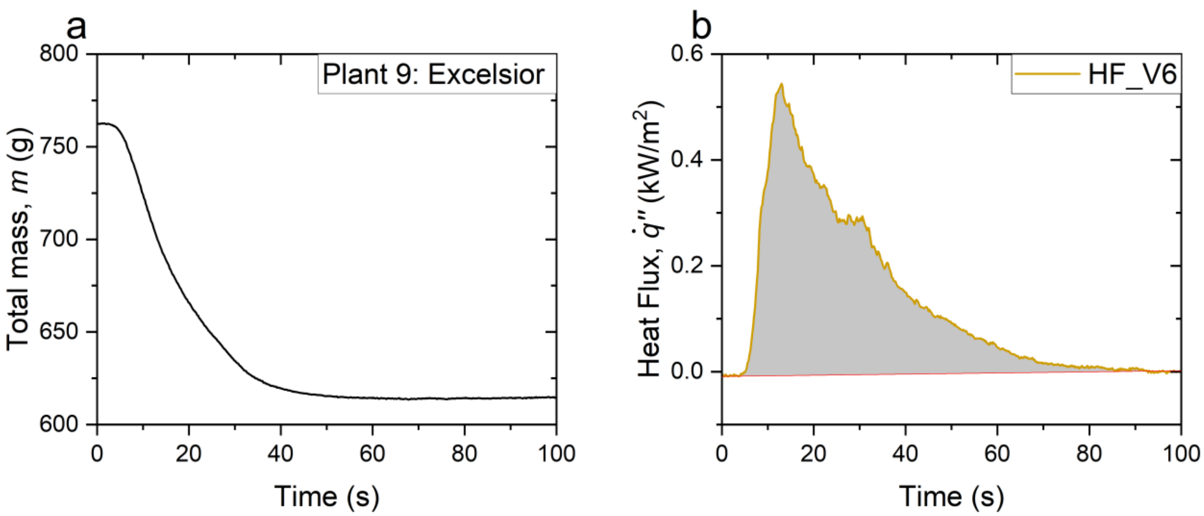

Fig. 6. (a) Total mass of the specimen and stand as a function of time during excelsior Test 9. (b) The heat flux measured at (*r*, *z*) = (2.14 m, 0.95 m) as a function of time during Test 9. The shaded area represents the integrated radiative heat flux incident on a gauge. The baseline represents a line based on measurements before ignition and after the fire extinguishment. The uncertainty in the mass and heat flux measurements are discussed in Appendix B and Appendix C.

3. Results and Discussion

3.1. Mass Loss and Heat Release Rate

The burning dry mass loss (Δm) was estimated by subtracting the specimen's water mass from the total mass loss measured using the load cell ($\Delta m_{measured}$),

$$\Delta m = \Delta m_{measured} \times \left(1 - \frac{MC_{dry}}{1+MC_{dry}}\right) \quad (6)$$

where MC_{dry} is the dry-basis moisture content of the specimen. The value of $\Delta m_{measured}$ was calculated as ($m_f - m_i$), where m_i and m_f are the initial and final mass after the experiment.

Table 3 lists the heat of combustion per unit of oxygen, the net heat of combustion per unit of fuel, and the mean measured effective heat of combustion. A heat of combustion on a per-oxygen basis of 13.23 kJ/g ± 0.66 kJ/g has been suggested as applicable for cellulosic materials with a range of stoichiometric oxygen-to-fuel mass ratios, ranging from pure cellulose to various chars [22, 23].

The net heat of combustion per unit fuel mass was obtained from literature values for the gross heat of combustion, which is typically provided by a bomb calorimeter (ASTM D5865/D5865M-19). The gross heat of combustion is then converted to a net value using the formula:

$$H_{c,net} = H_{c,gross} - 21.96h \quad (7)$$

where h is the mass fraction of hydrogen in the fuel, the equation assumes that water (as a combustion product) is entirely vapor for $H_{c,net}$.

The composition of 35 different vegetation samples from 4 references was evaluated, with the average hydrogen mass fraction found to be 6.1 % with a relative standard deviation of 12 % [24-27]. While the gross heat of combustion is often not reported with uncertainty, the standard deviation of 6 values reported for Douglas fir yielded 3 % – a relatively narrow value [11, 28, 29].

Table 3. The heat of combustion per unit mass of oxygen ($H_{c,oxygen}$), the net heat of combustion per unit mass of fuel ($H_{c,net}$), the mean measured effective heat of combustion ($H_{c,eff}$) for each vegetation type. The error bars represent the expanded (k=2) uncertainty.

Specimen	$H_{c,oxygen}$ (kJ/g)	$H_{c,net}$ (kJ/g)	$H_{c,eff}$ (kJ/g)
bluestem	13.23 ± 0.66[a]	18 ± 1[b]	14.9 ± 2.4
Douglas fir	13.23 ± 0.66[a]	21 ± 1[c]	17.5 ± 2.9
excelsior	13.23 ± 0.66[a]	18 ± 1[c]	16.9 ± 1.4

[a]Refs. [22, 23]
[b]Ref. [25]
[c]Ref. [29]

Figure 7 compares the total heat release (THR) from calorimetry determined by integrating the measured heat release rate with the ideal heat release (IHR) calculated from the product of the burning mass loss and the fuel's net heat of combustion ($\Delta m\ H_{c,net}$). As expected, the THR is consistently lower than IHR in most tests, indicating that the actual heat release is less than the ideal heat release. This can be the case due to incomplete combustion (for example, smoldering) or small unburnt portions of the vegetation that were observed to break off the specimen, falling beyond the load cell. This effect could also be due to moisture lost from any residual vegetation, which violates the assumption of Eq. (6), particularly for some of the Douglas fir samples with larger initial values of MC and more substantial residual mass.

The measured effective heat of combustion ($H_{c,eff}$), defined as THR/Δm, is calculated for each test, then averaged for each specimen type as listed in Table 3. The values for little bluestem, Douglas fir, and excelsior are 17 %, 17 %, and 4 % lower, respectively, than the heat of combustion per unit fuel mass ($H_{c,net}$) listed in Table 3. This discrepancy is noteworthy, as it indicates the influence of factors such as incomplete combustion or deviation from the assumption that the MC_{dry} is unchanged in the post-fire residual fuel mass on the relative amount of heat release measured per fuel mass loss.

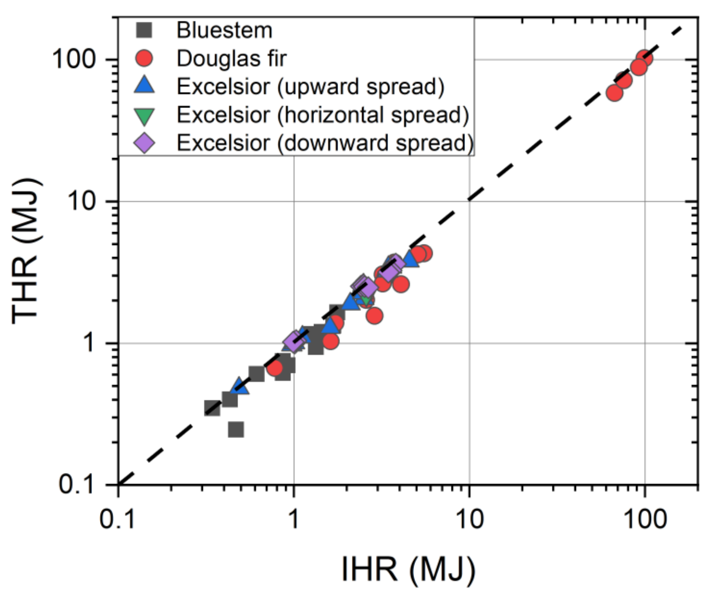

Fig. 7. Comparison of the total heat release (THR) measured using calorimetry with the ideal heat release (IHR) from the measured mass change.

3.2. Fire Appearance

Figure 8 to Figure 13 show sequential flame images in the little bluestem, excelsior, and Douglas fir fires. Figure 8 shows images of the bluestem 1 s after ignition and then the progression of the fire over its relatively short 20 s burning period. At 7 s, the fire reached its peak intensity. The flames were tall and slender, and the HRR obtained its peak value at this time. Thereafter, the flames rapidly reduced in size, the gas phase flames ended, and at about 13 s, there was a transition to a smoldering phase. The other figures also show the evolution of the fires from a moment near ignition, to the peak flame height, diminution of gas phase flames, a smoldering phase, and eventually fuel burnout. The video record for all the tests is available on the FCD.

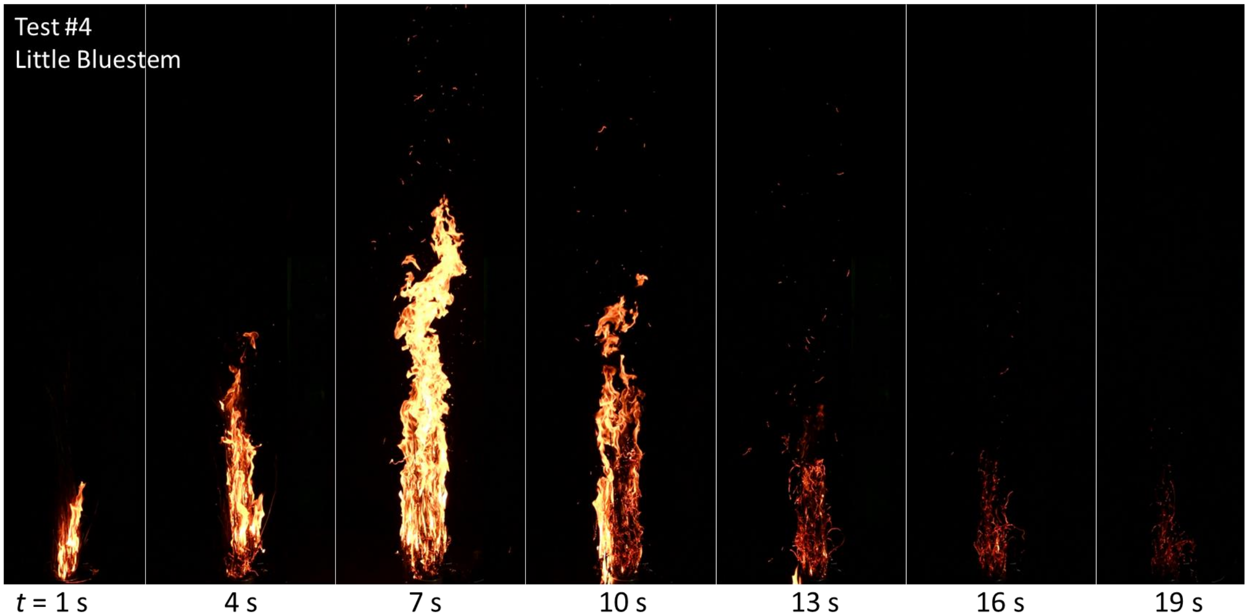

Fig. 8. Flame images as a function of time during Test 4 of a little bluestem fire.

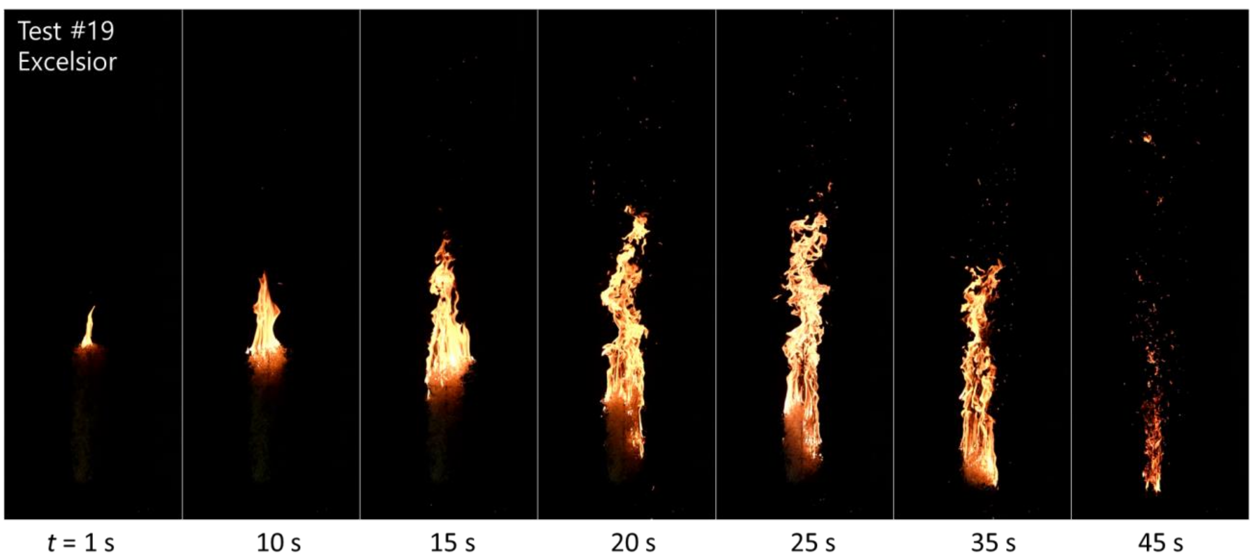

Fig. 9. Flame images as a function of time during Test 19, a low bulk density (6 kg/m^3) excelsior fire spreading downward.

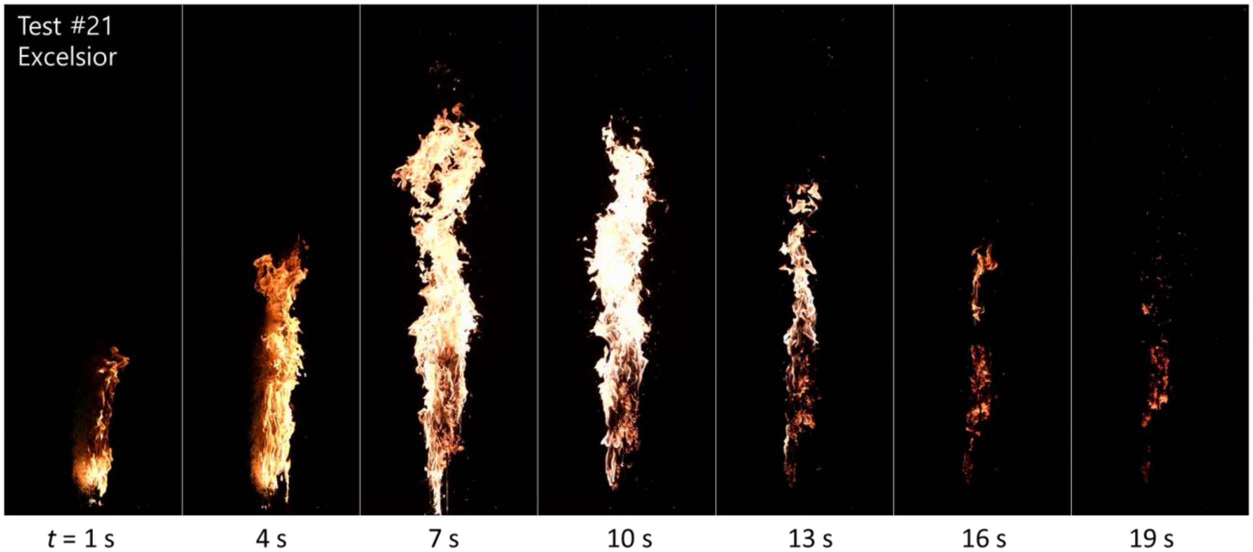

Fig. 10. Flame images as a function of time during Test 21, a low bulk density (6 kg/m^3) excelsior fire spreading upward.

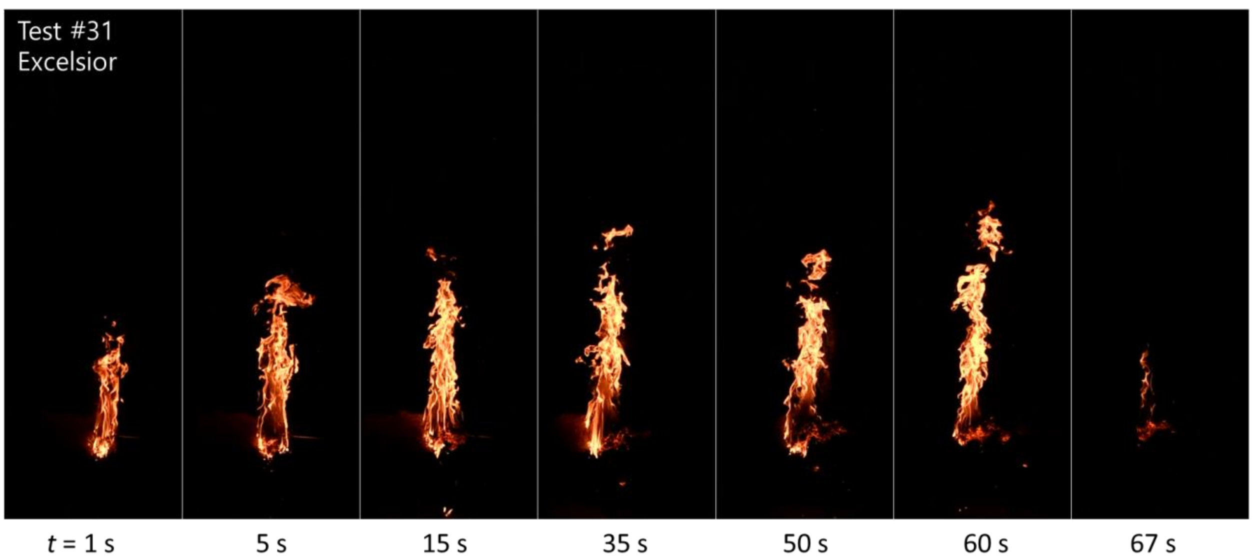

Fig. 11. Flame images as a function of time during Test 31, a moderate bulk density (14 kg/m^3) excelsior fire spreading horizontally excelsior fire. The flames are vertical and slowly spread from right to left in the images.

t = 1 s 4 s 7 s 10 s 20 s 50 s 100 s

Fig. 12. Flame images as a function of time during Test 38 of a 0.80 m tall Douglas fir tree fire.

t = 1 s 3 s 7 s 13 s 19 s 25 s 35 s

Fig. 13. Flame images as a function of time during Test 45 of a 1.46 m tall Douglas fir tree fire.

Figure 14 shows 6 moments (29 s,79 s, 82 s, 88 s, 89 s, and 93 s after ignition) during Test 53, a high-density (21 kg/m^3) excelsior bundle burning downward after ignition at its top. The first image in Fig. 14 shows the burning excelsior bundle as a dark mass behind the gas phase flames. The peak HRR occurs 74 s after ignition. At 79 s, Fig. 14 shows that the excelsior bundle appears fully engulfed in gas phase flames. At about 88 s, the HRR dropped to half its peak value and glowing combustion appeared at the base of the excelsior bundle, while gas phase flames appeared at its top. At 89 s, most portions near the middle of the excelsior bundle went dark and only a small amount of gas phase flames was visible until they completely disappeared, leaving only glowing combustion near the base of the excelsior bundle visible.

Also of note is the presence of aerosols/unburned pyrolyzate. Although the scene was intentionally underexposed, the aerosol cloud in images 3, 4, and 6 (right to left) of Figure 14 is clearly visible near the gas phase flames, which served to illuminate the cloud. At later points in the test, flaming combustion was not sustained but there was occasional re-ignition. This can be seen between 89 s and 93 s. Radiative emission from the glowing heated solid can be seen in image 5. The ratio of radiative emission from the hot smoldering solid to the gas phase radiative emission of the fire is unclear, nor is it clear how this ratio changes over time.[1] Suddenly at 93 s, the gas phase flames momentarily reignited. A plume of aerosol continued to rise about the specimen and then from 100 s to 106 s (not shown in Figure 14), reignition happened again with the appearance of gas phase flames. Additional measurements discussed in Fig. 15 provide further information about the aerosol cloud.

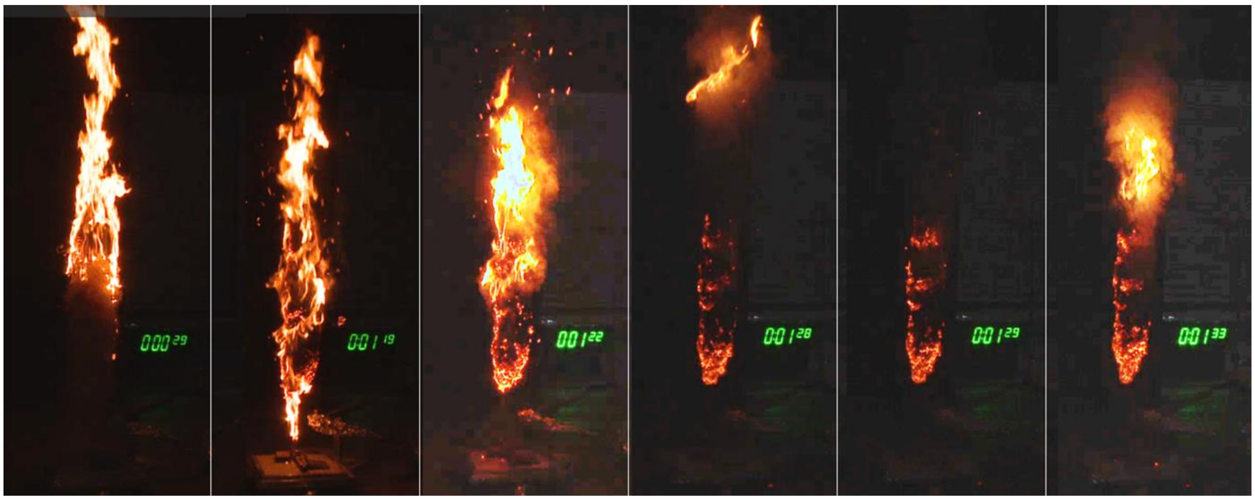

t = 29 s 79 s 82 s 88 s 89 s 93 s

Fig. 14. Flame images as a function of time during Test 53, a high-density (21 kg/m^3) excelsior fire spreading downward.

Figure 15 shows the transient HRR during Test 53. The HRR peaks at approximately 73 s and drops off precipitously when flaming combustion ends at 89 s (see images in Fig. 14). The figure also shows the transient radiative flux at Gauge HF_V1 (see Fig. 6), which roughly follows the shape of the HRR profile.

The aerosol cloud above a burning cellulosic fuel is composed of gaseous and particulate matter of various sizes [31]. Figure 15 shows the time-varying light extinction coefficient (*K*), which increased rapidly between 86 s and 88 s, fluctuated, and then rapidly decreased between 101 s and 106 s when flaming re-ignition of the aerosol cloud occurred. This can be interpreted as the hot flammable gases and particulate matter that compose the aerosol cloud undergoing combustion. Although *K* may not account for the presence of all aerosol species (e.g., gases such as carbon monoxide, carbon dioxide, and low molecular weight hydrocarbons) that are expected [31], it can be regarded as representative of the particulate matter emitted by the fire (see Section 2.6). Figure 15 also shows the modified combustion efficiency (*MCE*) defined in Ref. [32] as the ratio of the measured concentration of [CO_2] in the exhaust to the sum of the [CO] and [CO_2] concentrations. The *MCE* is a representation of unburnt gas phase species generated by the fire. When the fire reignited at 93 s and 101 s, *K* dropped, and *MCE* increased. A small jump in the radiative heat flux also appeared at 101 s. When the gas phase flames extinguished at 89 s, *K* suddenly increased, and *MCE* decreased. The relatively rapid changes in

1. This is a long standing problem [30] which cannot be solved with the instrumentation used in this study.

K as compared to *MCE* can be explained by the time constant of the measurement which is msec for a silicon diode detector and on the order of 10 s for the NDIR [CO] meter. Thus, the transient *MCE* profile results are consistent with the results for *K,* the visual observations, and the notion that the smoldering excelsior generated a heated plume of thermal decomposition products that could reignite, depending on the conditions.

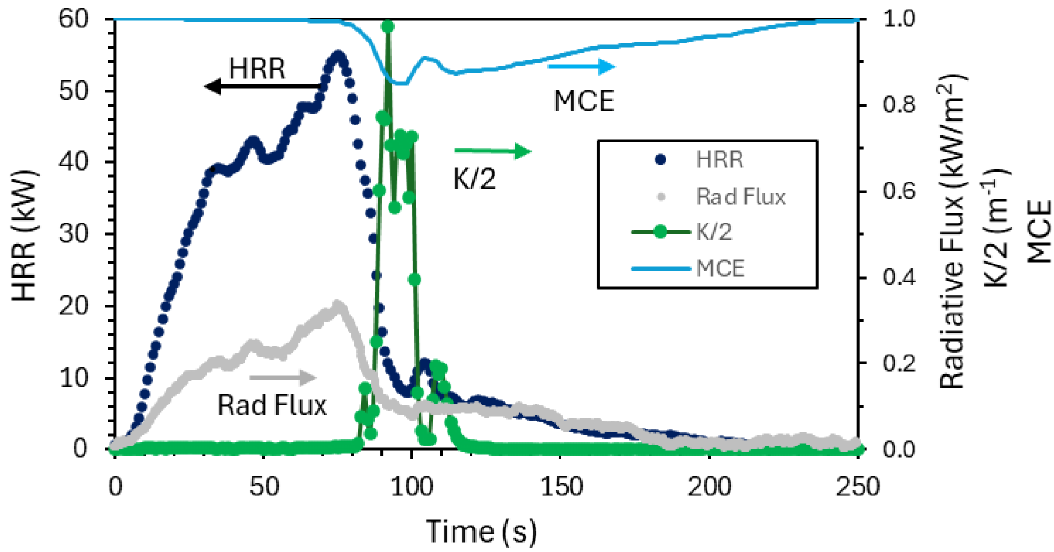

Fig. 15. The HRR as a function of time after ignition during Test 53 (left axis), a high-density excelsior fire ignited at the top and burned in the downward direction. Also shown (right axis) are the radiative flux (gauge HF_V1), the light extinction coefficient *K* (see Eq. 2) divided by 2, and the *MCE*.

It is of interest to compare the results of the high bulk density excelsior fire spreading downward in Test 53 to an analogous experiment with the fire spreading upward. Figure 16 shows such results for Test 51 (bulk density =20 kg/m^3). Here, the peak HRR occurred at about 11 s, a factor of 7 times faster than the downward spreading excelsior fire in Test 53 and with a peak value almost 30 % larger. Like the downward burning excelsior, the main peak of *K* occurred at the end of continuous flaming, at about 94 s. Reignition of the gas phase flames occurred momentarily at 97 s and the value of K dropped, only to rapidly increase when flaming disappeared a few seconds later. The value of *MCE* obtained a minimum at about the same time as *K* dropped.

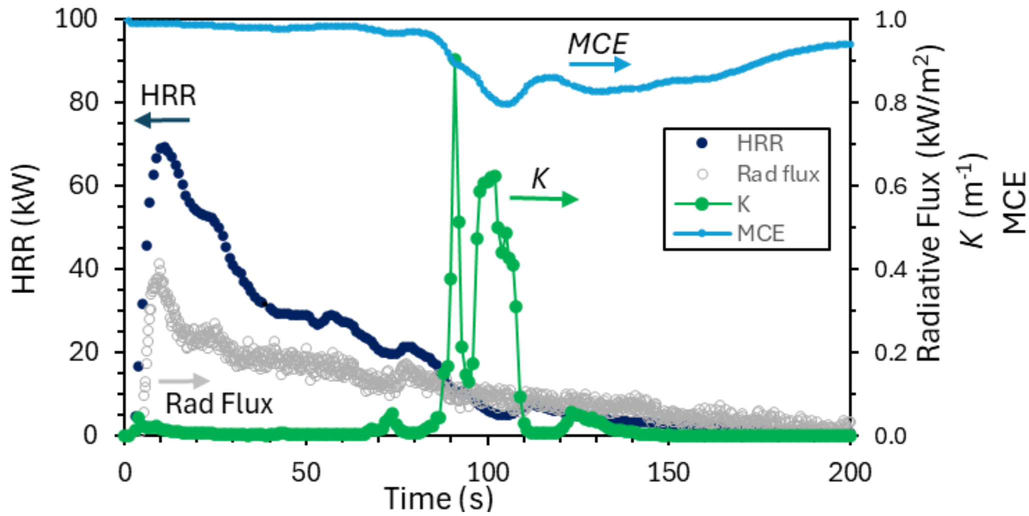

Fig. 16. The HRR as a function of time after ignition during Test 51 (left axis), a 1.46 m tall high-density excelsior fire ignited at the bottom, burning in the upward direction. Also shown (right axis) are the radiative flux (gauge HF_V1), the light extinction coefficient *K* (see Eq. 2), and the *MCE*.

The results for the largest Douglas fir tree fires are quite different than the large bulk density excelsior fires in Fig. 15 and Fig. 16. Figure 17 shows the transient HRR during Test 45, a 1.46 m tall Douglas fir tree ignited at its base. The peak fire HRR occurred at about 14 s with a value almost 50 times larger than the upward spreading excelsior fire in Test 51. This is not particularly surprising as the mass loss was a factor of 16 larger in the Douglas fir test. Unlike the upward and downward burning excelsior fires, the peak value of *K* occurred at about the same time as the peak HRR. A possible interpretation is that *K* was associated with soot escaping a fairly large fire, typical of burning hydrocarbons [18]. Smaller local maxima associated with *K* appeared at about the same time as the *MCE* minima, indicating enhanced generation of incomplete products of combustion, just as smoldering began at about 22 s after ignition (see images in Fig. 13). The radiative emission peaked at about the same time as the HRR. Appendix D provides the transient HRR, radiative heat flux, and light extinction coefficients for all the tests.

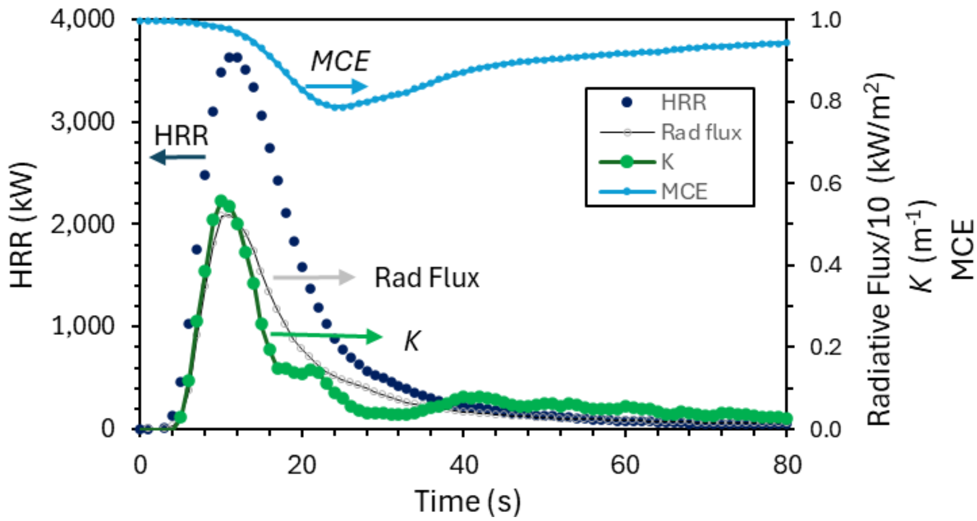

Fig. 17. The HRR as a function of time after ignition during Test 45 (left axis), a 1.46 m tall Douglas fir tree ignited at its base. Also shown (right axis) are the radiative flux divided by 10 (gauge HF_V1), the light extinction coefficient *K* (see Eq. 2), and the *MCE*.

Table 4 lists the mass loss, residual mass, duration of burning, time to the peak heat release rate and its value, and the total heat released (THR) from the fires. The THR is calculated by integrating the heat release rate profile over the entire duration of the fire.

Table 4. The mass loss, the residual mass percentage, the duration of the fire, the time to peak heat release rate, the peak heat release rate, and the total heat released (THR). See the NIST FCD [10] for uncertainty information.

Test	Specimen	Mass loss (g)	Residual mass (%)	Duration (s)	$t_{peak\ HRR}$ (s)	Peak HRR (kW)	THR (MJ)
little bluestem							
1	bluestem	80	≈0	127	16	50	1.2
2	bluestem	68	≈0	224	15	69	1.2
3	bluestem	98	≈0	146	19	81	1.7
4	bluestem	34	≈0	133	12	46	0.6
5	bluestem	24	≈0	117	11	29	0.4
6	bluestem	19	≈0	120	11	28	0.4
24	bluestem	74	≈0	62	39	46	1.1
25	bluestem	76	≈0	74	33	48	1.2
28	bluestem	48	≈0	52	34	35	0.8
29	bluestem	93	≈0	83	30	77	1.4
30	bluestem	26	≈0	37	34	26	0.4
33	bluestem	48	≈0	116	34	31	0.8
34	bluestem	51	≈0	294	32	19	0.7
Douglas fir (DF)							
12	DF tree	137	55	64	28	69	1.6
13	DF tree	153	41	104	13	203	3.1
14	DF tree	158	43	101	14	202	3
22	DF tree	178	32	147	13	188	3.8

Test	Specimen	Mass loss (g)	Residual mass (%)	Duration (s)	$t_{peak\ HRR}$ (s)	Peak HRR (kW)	THR (MJ)
23	DF tree	262	46	125	22	229	4.4
37	DF tree	123	59	113	32	84	2.1
38	DF tree	194	38	152	13	100	2.7
39	DF tree	153	63	142	18	154	2.7
40	DF tree	82	48	119	11	91	1.4
41	DF tree	37	91	292	214	12	0.7
42	DF tree	77	75	130	22	59	1.1
43	DF tree	242	58	166	13	232	4.4
44	DF tree	4726	31	306	14	7918	102.3
45	DF tree	3201	31	369	13	3632	60
46	DF tree	4394	28	389	14	5987	91.4
47	DF tree	3614	26	479	15	4688	74
excelsior fires spreading upward							
9	excelsior	137	≈0	138	17	100	2.6
15	excelsior	138	≈0	106	15	107	2.6
17	excelsior	54	≈0	88	14	74	1.0
21	excelsior	56	≈0	78	13	76	1.0
26	excelsior	139	≈0	77	34	75	2.1
27	excelsior	252	≈0	74	33	172	3.8
35	excelsior	89	≈0	62	32	82	1.3
36	excelsior	116	≈0	62	30	126	1.9
48	excelsior	139	≈0	137	29	94	2.4
49	excelsior	137	≈0	70	29	94	2.3
50	excelsior	190	≈0	215	14	75	3.2
51	excelsior	200	≈0	304	11	69	3.4
52	excelsior	192	≈0	209	13	72	3.4
56	excelsior	27	≈0	27	6	52	0.5
excelsior fires spreading horizontally							
31	excelsior	144	≈0	84	52	49	2.5
32	excelsior	143	≈0	89	79	41	2.4
excelsior fires spreading downward							
7	excelsior	134	≈0	151	48	84	2.5
8	excelsior	138	≈0	154	39	93	2.6
10	excelsior	140	≈0	102	52	72	2.5
11	excelsior	147	≈0	142	53	60	2.5
18	excelsior	56	≈0	110	32	36	1.0
19	excelsior	57	≈0	125	49	37	1.0
20	excelsior	55	≈0	117	39	41	1.0
53	excelsior	211	≈0	252	75	55	3.6
54	excelsior	199	≈0	292	51	55	3.3
55	excelsior	192	≈0	323	48	53	3.2

Fig. 18 shows that the THR is correlated to the product of the peak HRR and the experimental duration by a line in the log-log plot. A fit such as this would be expected if the HRR profiles could be approximated as triangular. Then, the THR would be proportional to the product of the peak HRR and the test duration. The fit shown in the figure does not collapse the data, suggesting that the model is imprecise, but it does roughly represent trends in the data.

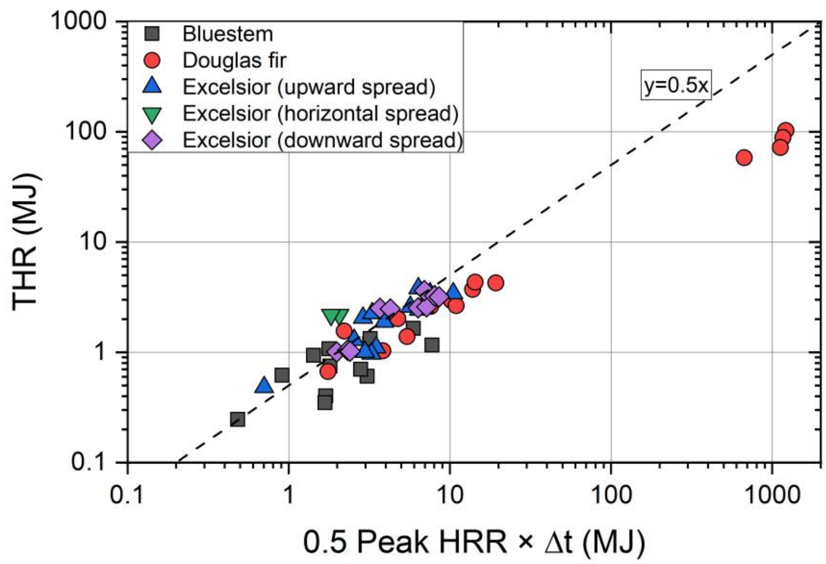

Fig. 18. The total heat released (THR) as a function of the product of the peak heat release rate (HRR) and the duration of the fire (*Δt*).

Figure 19 shows the ratio of the peak heat release rate (PHRR) to the initial mass (m_i) of the specimen as a function of the dry basis moisture content for specimens tested in the present work and for trees and bushes previously studied [13]. Vegetation with low moisture content (below 20 %) shows a much higher peak HRR/mass, indicating that the drier fuels burned more intensely, leading to a larger peak HRR. The ratio is larger than 1000 kW/kg at very low moisture content (below 10 %) for excelsior and little bluestem. As expected, the results show that the moisture content significantly affects the vegetation fires, with higher moisture content generally resulting in a lower peak HRR and fire intensity regardless of the species type.

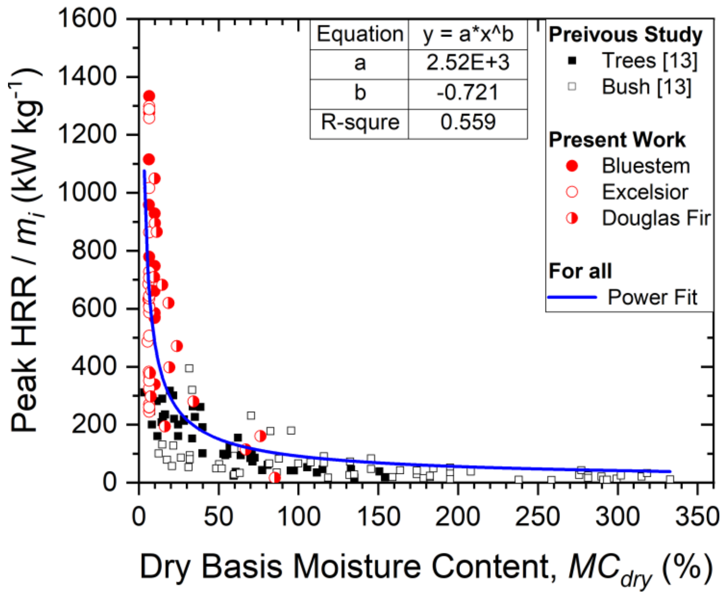

Fig. 19. The ratio of the peak heat release rate to the initial mass (m_i) of the specimen as a function of its dry basis moisture content. For comparison, previously published data presented in Ref. [13] for a variety of trees and bushes is also shown. The mean expanded (k=2) uncertainty of the ratio for all tests was estimated as 6 %.

Figure 20 shows the PHRR of the excelsior fires as a function of the specimen bulk density. As expected, the upward-spreading fires gave rise to larger PHRRs than those spreading downward. This was also the case for the horizontally oriented fires (Tests 31 and 32), which spread slower and had smaller peak HRRs than the upward-spreading fires. The fact that peak HRR does not correlate strongly with bulk density highlights the complex interaction between additional fuel mass and increased fuel packing.

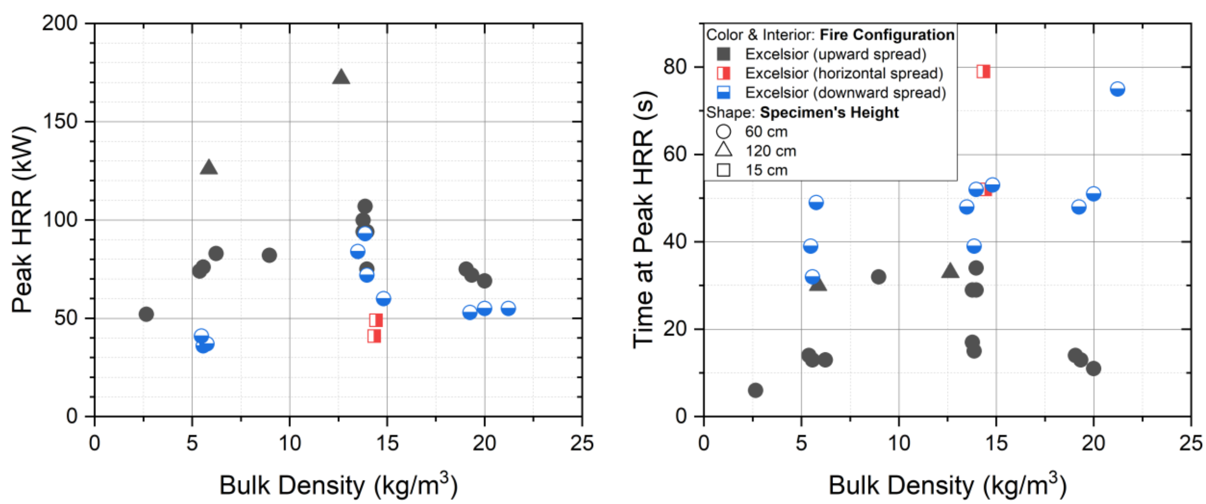

Fig. 20. The Peak HRR and Time at the peak HRR as a function of the bulk density for upward, downward, and horizontally spreading excelsior fires.

The time to reach the PHRR was 23 s ± 9 s for the upward spreading excelsior fires, almost twice as fast as the downward spreading fires (46 s ± 8 s). The horizontally spreading fires took the longest to obtain the PHRR (67 s ± 8 s) – almost three times as long as the upward spreading fires.

3.2.1. Unburnt Fuel Mass

Figure 21 shows the residual mass ratio as a function of the dry basis moisture content. The Douglas fir specimens exhibited a wide range of moisture content, spanning approximately 10 % to 85 %. The residual mass of the Douglas fir trees increased with the moisture content, indicating that the trees only partially burned. In contrast, the residual fuel mass of excelsior and little bluestem was very low, indicating that these specimens burned almost entirely, leaving only negligible remnants after the fire. Additionally, even for the driest Douglas fir trees, the residual mass was above 20%. Unlike the other specimens which were comprised entirely of thin fuel, the trees had a mixture of fuel element diameters, from needles up to the trunk size. The remaining fuel in a dry tree test is related to this distribution of sizes.

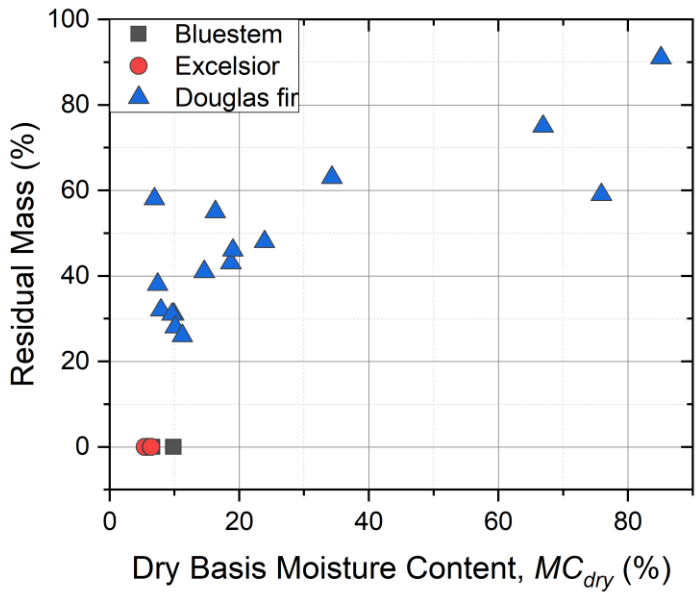

Fig. 21. Residual mass ratio as a function of the dry basis moisture content (MC_{dry}).

3.3. Peak Flame Height

Figure 22 shows an example of the similarity of RGB and processed binary images for moments during the Douglas fir Tests 42 and 43. The vertical gray bar in the binary image indicates the flame height. The visible (RGB) and processed binary images are nearly identical in flame shape and height.

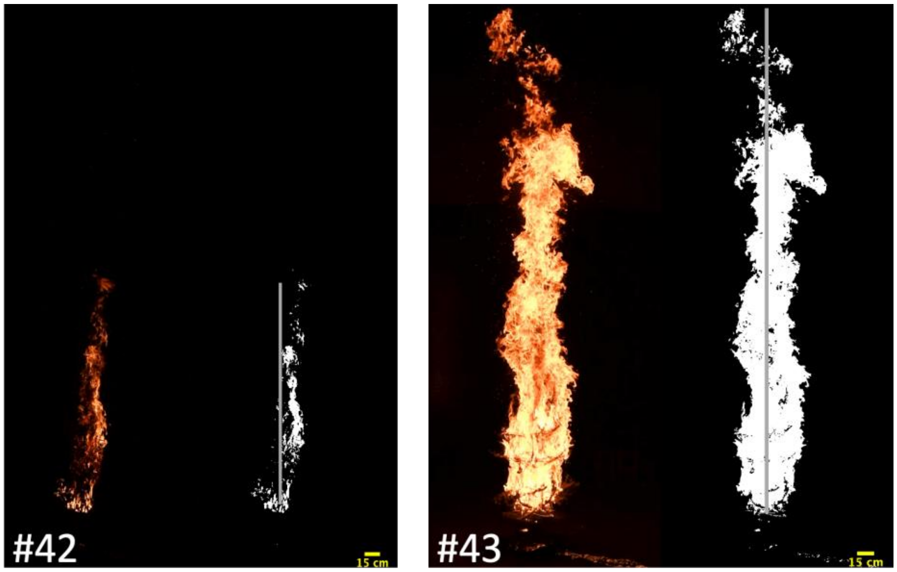

Fig. 22. The visible (RGB) and processed binary images of moments during the Douglas fir fires in Tests 42 and 43, showing the similarity in flame shape and height.

The peak flame height for the little bluestem and the Douglas fir fires is listed in Table 5. The expanded combined uncertainty averaged 20 % across all tests (see Appendix B.2).

Table 5. Peak flame height and expanded (k=2) combined uncertainty for the tests with little bluestem, Douglas fir, and excelsior. The direction of flame spread is listed for the excelsior fires.

Test	Specimen	Peak Flame Height (cm)	Flame Spread
little bluestem			
1	bluestem	148 ± 29	upward
2	bluestem	180 ± 36	upward
3	bluestem	190 ± 38	upward
4	bluestem	162 ± 32	upward
5	bluestem	127 ± 25	upward
6	bluestem	129 ± 26	upward
24	bluestem	161 ± 32	upward
25	bluestem	160 ± 32	upward
28	bluestem	161 ± 32	upward
29	bluestem	199 ± 40	upward
30	bluestem	141 ± 28	upward
33	bluestem	140 ± 28	upward
34	bluestem	106 ± 21	upward
Douglas fir			
12	Douglas fir	103 ± 20	upward
23	Douglas fir	285 ± 57	upward
37	Douglas fir	159 ± 32	upward
38	Douglas fir	245 ± 49	upward
39	Douglas fir	242 ± 48	upward

Test	Specimen	Peak Flame Height (cm)	Flame Spread
40	Douglas fir	218 ± 43	upward
42	Douglas fir	147 ± 29	upward
43	Douglas fir	299 ± 59	upward
excelsior fires spreading upward			
9	excelsior	182 ± 36	upward
15	excelsior	179 ± 36	upward
16	excelsior	172 ± 34	upward
17	excelsior	178 ± 35	upward
21	excelsior	173 ± 34	upward
26	excelsior	202 ± 40	upward
27	excelsior	273 ± 54	upward
35	excelsior	201 ± 40	upward
36	excelsior	259 ± 51	upward
48	excelsior	167 ± 33	upward
49	excelsior	151 ± 30	upward
50	excelsior	135 ± 27	upward
51	excelsior	132 ± 26	upward
52	excelsior	127 ± 25	upward
56	excelsior	137 ± 27	upward
excelsior fires spreading horizontally			
31	excelsior	151 ± 30	horizontal
32	excelsior	136 ± 27	horizontal
excelsior fires spreading downward			
7	excelsior	174 ± 35	downward
8	excelsior	174 ± 35	downward
10	excelsior	185 ± 37	downward
11	excelsior	126 ± 25	downward
18	excelsior	126 ± 25	downward
19	excelsior	126 ± 25	downward
20	excelsior	131 ± 26	downward
53	excelsior	115 ± 23	downward
54	excelsior	115 ± 23	downward
55	excelsior	109 ± 22	downward

Figure 23 shows a box and whisker plot of the peak flame height for each specimen type. The Douglas fir tree fires yielded the largest flame heights, followed by excelsior and bluestem. The two outliers in the excelsior case resulted from larger specimen height, which is twice the typical height of 60 cm.

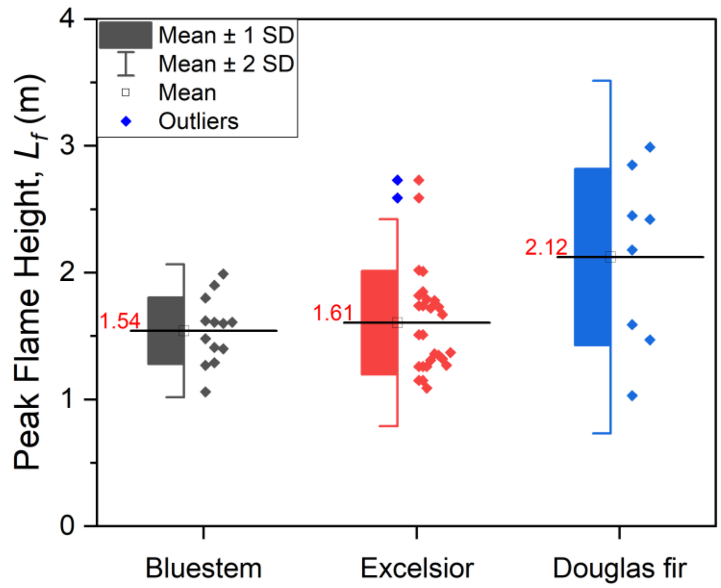

Fig. 23. A box and whisker plot of the mean peak flame height for each specimen type.

Figure 24 shows the peak flame height and the normalized peak flame height by the specimen's height (L_f/H) as a function of the specimen's moisture content. The peak flame height decreased as the specimen's moisture content increased. Comparing the results of Test 39 and Test 43, the Douglas fir trees were similar in size and mass (see Table 1), but the residual mass in Test 39 was 11 % larger than in Test 43, primarily due to the specimen's large moisture content. The peak flame height in Test 39 was about 40 % smaller than in Test 43.

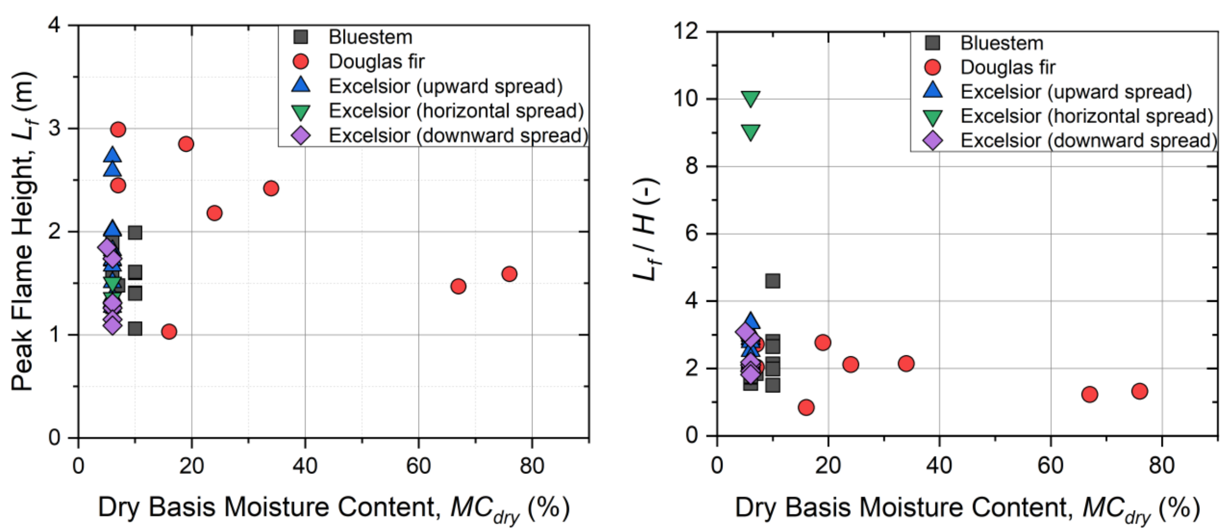

Fig. 24. The peak flame height (left) and the peak flame height (L_f) normalized by the specimen's height (right) as a function of the specimen dry basis moisture content.

Figure 24 shows the normalized peak flame height by specimen's height. The range and mean values for each specimen are listed in Table 6. For excelsior tests, the peak flame height in upward fire spreading is higher, compared to downward fire spreading, because the flame at the base initiates heating of the fuel, facilitating rapid fire propagation, resulting in a notably substantial maximum flame height.

Table 6. Peak flame height normalized by initial specimen height (L_f/H).

Specimen	L_f (m)		L_f/H (-)		Tests, *N*
	Range	Mean ± SD	Range	Mean ± SD	
bluestem	1.1 - 2.0	1.5 ± 0.3	1.5 - 4.6	2.2 ± 0.8	13
Douglas fir	1.0 - 3.0	2.1 ± 0.7	0.8 - 2.8	1.9 ± 0.7	8
excelsior (upward spread)	1.3 - 2.7	1.8 ± 0.4	2.1 - 3.4	2.7 ± 0.4	15
excelsior (horizontal spread)	1.4 - 1.5	1.4 ± 0.1	9.1 - 10.1	9.6 ± 0.7	2
excelsior (downward spread)	1.1 - 1.9	1.4 ± 0.3	1.8 - 3.1	2.3 ± 0.5	10

Figure 25 shows the peak flame height and the normalized peak flame height by the specimen's height (L_f/H) as a function of the bulk density of excelsior. Examining the 60 cm samples, the maximum flame heights are found at the intermediate range of bulk densities tested. This demonstrates a competing effect between the increasing bulk density leading to an increasing amount of fuel (larger flame height) and a decreasing porosity (less efficient burning and less flow within the fuel, leading to a smaller flame height). This matches the behavior observed with the peak HRR in Fig. 20.

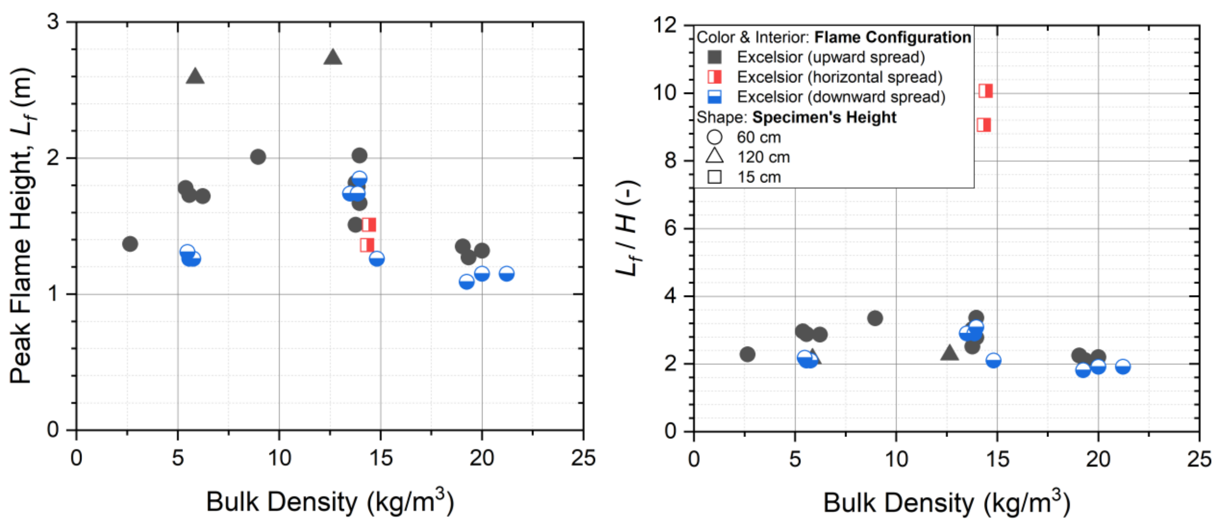

Fig. 25. The peak flame height (left) and the peak flame height (L_f) normalized by the specimen height (right) as a function of the excelsior bulk density.

3.4. CO and Soot Yields

The mean and range of CO and soot yields by specimen type are listed in Table 7, and the yield measurements in each test are listed in Table C1. Each of the individual test results is tabulated in Appendix C. Douglas fir trees had the largest mean CO yield, which was 9 % on -average, followed by little bluestem at 6 % and excelsior at 3 %. The ranges of CO yield results were similar for the three fuel types, varying from about 63 % to 214 % of the mean value.

Table 7. Mean and range of CO and soot yields by specimen type. The ratio of the mean values is also listed.

Specimen	Y_{CO} (kg/kg x 10^{-3})		Y_{SOOT} (kg/kg x 10^{-3})		(Y_{CO} /Y_{SOOT})
	Mean	Range	Mean	Range	Mean
little bluestem	61.9	42 to 88	5.03	0 to 21	12
excelsior	37.7	19 to 85	3.45	0 to 15	11
Douglas fir	89.1	58 to 120	4.12	1.7 to 11	22

The soot yields did not follow the same trend as the CO yield. Little bluestem had the largest mean soot yield, which was 0.50 % on average, followed by Douglas fir at 0.40 %, and excelsior at 0.35 %. The range of soot yields was much broader than the CO yields, varying from about 15 % to 2630 % of the mean for little bluestem. The range of soot yields was also appreciably larger than the CO yields for the other two fuel types.

The large number of experiments conducted in this study revealed the variation in the CO and soot yield results for all three fuel types. The results are consistent with yields measured in fires burning large (5 m) Douglas fir trees [33]. The CO and soot yields are both significantly larger than small (10 cm diameter) pool fires burning simple two and three carbon hydrocarbons with the ratio of CO to soot more than 30 times larger than in hydrocarbon fires [34]. This may be attributed to the smoldering of the cellulosic fuels investigated in this study, which can produce relatively large amounts of CO compared to flaming fires [35].

Figure 26 shows the soot yield as a function of the bulk density for all the excelsior fires. Excelsior fires with higher bulk density tend to produce greater soot yields than those with lower bulk density. Visible observation suggests that the yields are mainly associated with thermal decomposition in the absence of flames. Since, the soot yield is calculated using a mass-specific extinction coefficient typical of soot (σ_s) and not a value more typical of particulate matter produced during smoldering combustion, the uncertainty may actually be about a factor of two larger than shown in Fig. 26 (see Section 2.6 for a detailed discussion of the optical extinction coefficient).

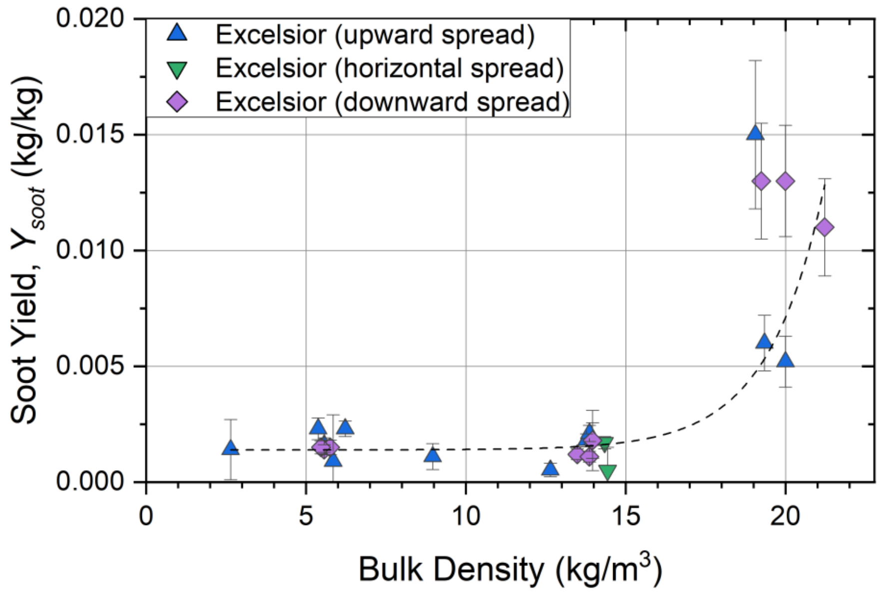

Fig. 26. The soot yield as a function of the bulk density for all the excelsior fires. The error bars represent the combined expanded (k=2) uncertainty.

3.5. Radiative Fraction

Fig. 27 shows a box and whisker plot of the radiative fraction for each vegetation type and also a plot of the radiative function of the dry basis moisture content. The mean, standard deviation, and range of the radiative fraction and the specimen's dry basis moisture range are also listed in Table 8. The radiative fraction for each test is listed in Table B2 in Appendix B.3. The mean values of the radiative fractions for the little bluestem, excelsior, and Douglas fir are 0.34, 0.33, and 0.29, respectively. Douglas fir trees had a wide dry basis moisture content range (7 % to 85 %). The radiative fraction decreased from about 0.41 to 0.15 as the moisture content increased, as seen in the right-hand plot of Fig. 27. This trend is consistent with the peak flame height, which also decreased with increasing moisture content, as seen in Fig. 24. The error bars for each χ_{rad} measurement in Fig. 27 represent the standard deviation of the radiative fraction measured using multiple heat flux gauges for each test. Larger values of the error bars indicate that the radiative flux to the surroundings was asymmetric, suggesting obstruction of the specimen's radiative flux to the surroundings on one or more sides of the specimen. The largest error bars are generally associated with larger values of specimen moisture content. In the larger moisture content tests (MC_{dry} > 60 %), ignition was typically not symmetric, leading to more burning on one side of the tree but not simultaneously on all sides. In these tests, the non-burning branches of the tree absorbed a portion of the radiative emission. Eliminating the tests in which there was only partial burning, the average radiative fraction is 0.32 ± 0.06.

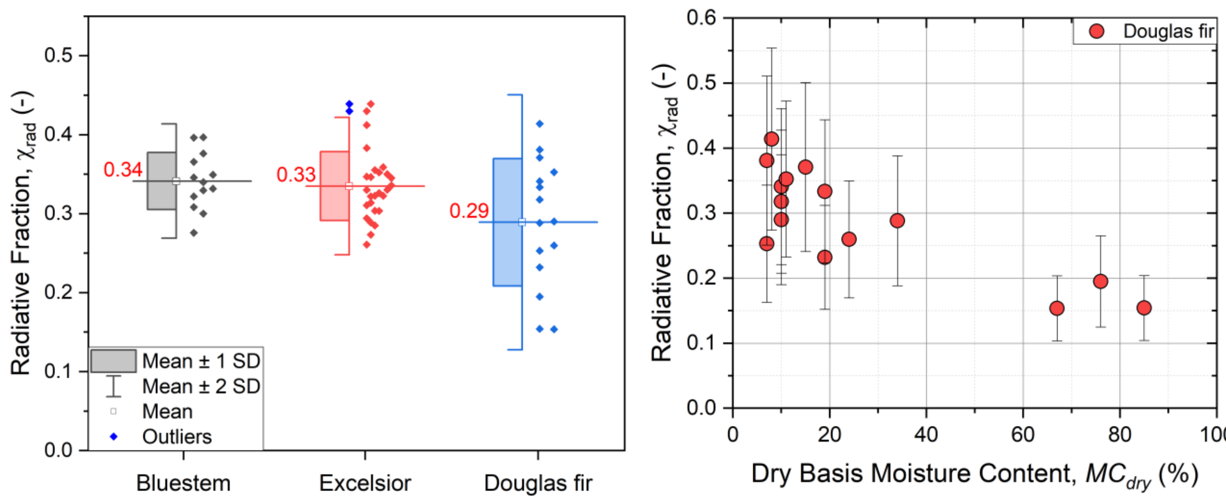

Fig. 27. A box and whisker plot showing the mean radiative fraction and its standard and expanded (k=2) deviation for each vegetation type (left), and the mean radiative fraction as a function of dry basis moisture content for Douglas fir fires (right). The error bars represent the expanded (k=2) uncertainty (95 % confidence interval).

Table 8. The mean, standard deviation, range of radiative fraction (χ_{rad}), and specimen's dry basis moisture content (MC_{dry}) range.

Specimen	χ_{rad} (-)	Range (-)	MC_{dry} Range (%)
bluestem	0.34 ± 0.11	0.28 - 0.40	6 - 10
Douglas fir	0.29 ± 0.10	0.15 - 0.41	6 - 85
excelsior (upward spread)	0.32 ± 0.06	0.26 - 0.41	6
excelsior (horizontal spread)	0.28 ± 0.06	0.27 - 0.29	6
excelsior (downward spread)	0.36 ± 0.07	0.32 - 0.44	5 - 6

Figure 28 shows the radiative fraction as a function of the bulk density of excelsior for the different test configurations involving the flame spread direction and the specimens' vertical extent (or height). The radiative fraction was about constant for bulk densities below 15 kg/m^3. For larger bulk densities, the radiative fraction increased and obtained a maximum value of 0.45, regardless of the flame spread direction or the specimen's height. It's helpful to recall that the higher bulk density excelsior fires tended to generate larger soot yields than the lower density fires, as shown in Fig. 26. However, as discussed above, this yield is not only a measure of soot, so the larger values do not necessarily correlate to higher emission from soot particles in the luminous flame.

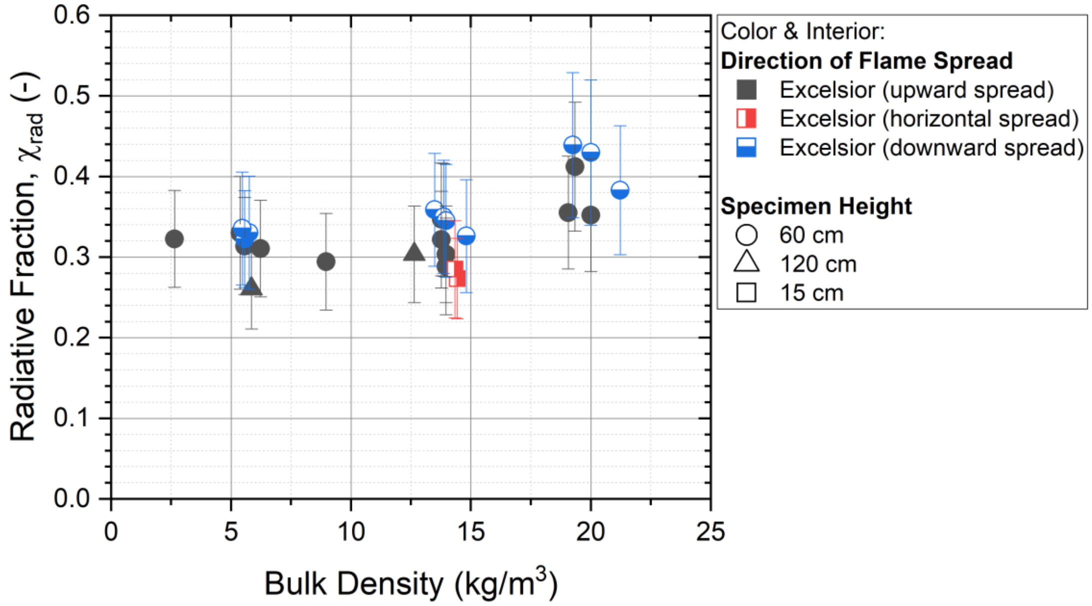

Fig. 28. Radiative fraction as a function of the bulk density of excelsior for the different flame spread directions and initial specimen vertical extent or height.

For a significant portion of these tests, there was a long period of smoldering after flaming combustion disappeared. The video record reveals the times when flaming combustion began and ended. The video record, however, is not particularly helpful in identifying the beginning of smoldering combustion. Smoldering can occur over a portion of the burning solid, even while gas phase flames are simultaneously occurring elsewhere. The gas phase flames are so bright, they could mask portions of the burning solid that may be smoldering. Although it's not possible to separate the purely gas-phase radiative emission from emission by a hot charring or smoldering solid using the current instrumentation, examining the change in the radiative fraction over different cumulative periods[2] provides insight on the character of these two distinct modes of combustion. Considering Eqns. (3) - (5), the cumulative radiative fraction, $\chi_{rad}(t_w)$, is defined as:

$$\chi_{rad}(t_w) = \frac{4\pi r^2 \int_{t_0}^{t_w} \overline{\dot{q}_i''}\,(t)\,dt}{[\mathrm{m}(t_w)-\mathrm{m}(t_0)][1/(1+MC_{dry})] \times H_{c,eff}} \quad (8)$$

where t_0 is the ignition time, t_w is the duration of the cumulative period, $m(t_w)$ is the measured mass at time t_w, $\overline{\dot{q}''}$ is the average value of the transient heat flux measured using multiple gauges, and $H_{c,eff}$ is the mean effective heat of combustion for each specimen type as listed in Table 3. The cumulative radiative fraction at the end of the experiment was identically equal to the radiative fraction listed in Table B2.

Figure 29 shows the evolution of the cumulative radiative fraction during Test 53, the high bulk density downward spreading excelsior fire presented in Fig. 14 and Fig. 15. The end of gas phase flames in the test is seen in the video record (Fig. 14) and corresponds to the time when

2. The authors are indebted to Rodney Bryant and Nigel Amoafo-Yeboah of NIST for suggesting this approach.

the heat release rate dropped to one-half of its peak value. In Test 53, the cumulative radiative fraction at the end of the flaming period ($\chi_{rad,f}$) was about equal to 0.29, a factor of 1.3 lower than the cumulative radiative fraction at the end of the test, which asymptotically reached 0.38 ± 0.04. Similar trends are observed in the little bluestem and Douglas fir fires as seen in Fig. 30 and Fig. 31.

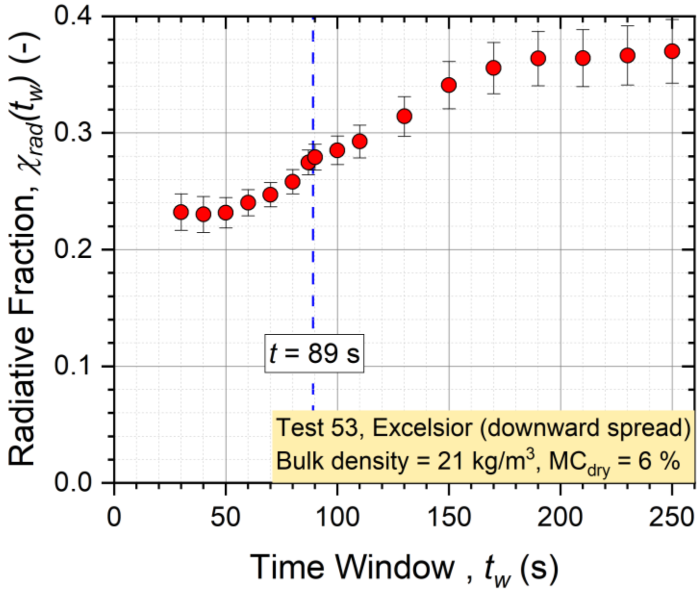

Fig. 29. The cumulative radiative fraction as a function of the time window size in Test 53. The error bars indicate the standard deviation of the radiative fraction obtained from multiple heat flux gauges. The dashed vertical line at 89 s represents the end of the period of gas phase flaming (see Fig. 14).

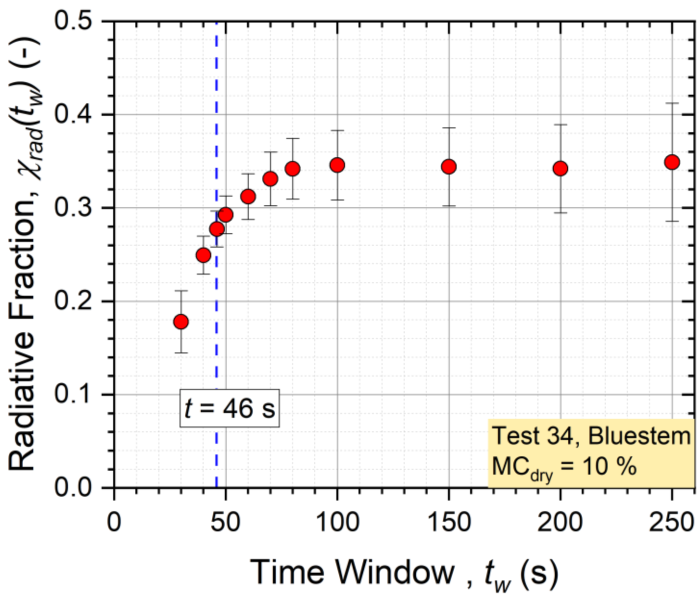

Fig. 30. The cumulative radiative fraction as a function of the time window size in Test 34. The error bars indicate the standard deviation of the radiative fraction obtained from multiple heat flux gauges. The dashed vertical line at 46 s represents the end of the period of gas phase flaming.

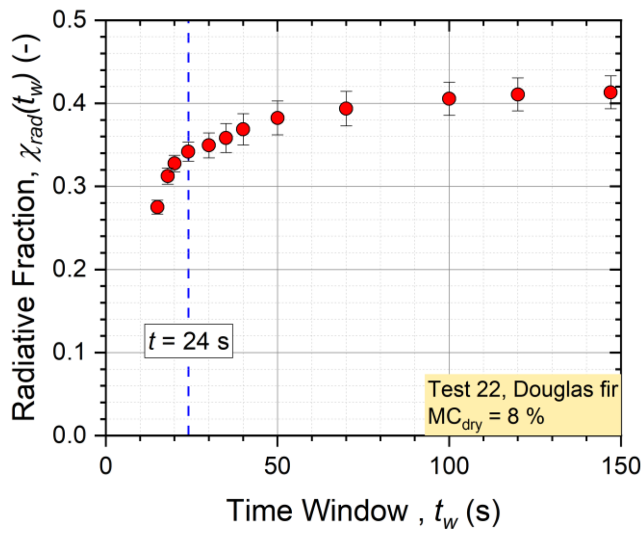

Fig. 31. The cumulative radiative fraction as a function of the time window size in Test 22. The error bars indicate the standard deviation of the heat flux which was measured by multiple heat flux gauges. The dashed vertical line at 24 s represents the end of the period of gas phase flaming.

Figure 32 shows the mass loss and radiative heat flux as a function of time in Test 53, the downward burning high-density excelsior fire. During the purely smoldering phase which started at about 89 s after ignition (see images in Fig. 14), the heat flux remained at approximately 30 % of its peak value until 140 s. At the same time, the mass loss was around 10 % of the initial mass of the specimen. This result provides an explanation as to why the cumulative radiative fraction increased with the expanding time window (t_w) in Fig. 29. Thus, the hot smoldering excelsior in Test 53 significantly influenced the radiative fraction result even though the total integrated emission during the flaming period is much larger than during the smoldering period.

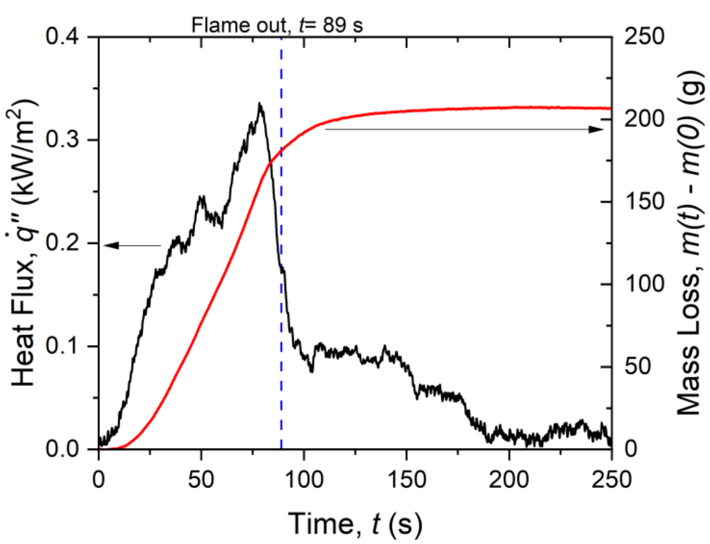

Fig. 32. Radiative heat flux (left axis; measured using Gauge HF_V1) and the mass loss (right axis) as a function of time in a high bulk density downward spreading excelsior fire (Test 53). The dashed vertical line at 89 s represents the end of the period of gas phase flaming (see Fig. 14).

Figure 33 shows the ratio of the cumulative radiative fraction during the flaming period ($\chi_{rad,f}$) to the radiative fraction over the entire burning period (χ_{rad}) as a function of the bulk density for the excelsior fires. As the bulk density increased, the ratio of $\chi_{rad,f}$ to χ_{rad} decreased, indicating that the radiative fraction increased from the early burning phase when flaming was evident as compared to the entire burning period.

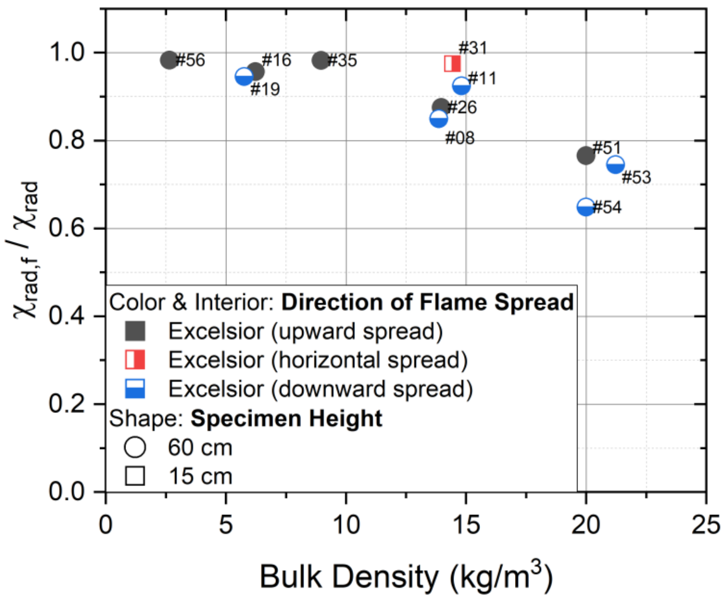

Fig. 33. The ratio of the cumulative radiative fraction during the period of gas phase flaming to the cumulative radiative fraction for the entire experiment as a function of the bulk density of the excelsior fires. The flame symbols are categorized by the fire spread direction and the specimens' initial vertical extent.

4. Summary and Conclusions

A series of measurements were conducted to better understand the burning characteristics of three types of vegetative fuels: little bluestem grass, excelsior wood fibers, and Douglas fir trees. The measurements included the transient heat release rate (HRR) determined using oxygen consumption calorimetry, the mass loss rate, the yields of CO and smoke, and the radiative emission to the surroundings. An estimate of the average radiative fraction during the fires was obtained from radiative heat flux measurements made in the far field. Experiments were also conducted on extensions of excelsior positioned horizontally and vertically with controlled bulk density. A summary of key findings follows.

1. The ratio of the peak heat release rate to the initial mass of the test specimens as a function of their dry moisture content was consistent with previously published fire measurements on a variety of trees and bushes. A fit to all the data showed that a power law was an adequate representation of the results.
2. The moisture content significantly affected the Douglas fir tree fires. As the tree moisture content increased, the radiative fraction significantly decreased. The radiative fraction of the Douglas fir tree fires was observed to decrease from 0.41 to 0.15 as the dry basis moisture content increased from 6 % to 85 %.
3. The mean radiative fractions for little bluestem, excelsior, and Douglas fir fires were 0.34, 0.33, and 0.29, respectively. Considering the overlapping error bars, there is no statistically significant difference among the fuel types. The average radiative fraction for all the tests was 0.32. Further work is needed to differentiate radiative emission due to gas phase flames as compared to glowing, smoldering combustion for cellulosic fuels.
4. Consideration of the cumulative radiative fraction provides insight on the change in the radiative fraction from a fire’s flaming stage to its smoldering phase. While radiative emission from the hot smoldering materials was smaller than the emission early in the fire when gas phase flames were present, the cumulative radiative fraction during the entire burn including the smoldering period was measurably larger than the cumulative radiative fraction just during the flaming combustion phase. For excelsior, this effect became more significant for higher bulk densities.
5. The soot yield had a high degree of scatter for all sample types with mean values of 0.46 % for bluestem, 0.11 % for excelsior, and 0.24 % for Douglas fir. The CO yield had mean values of 6.2 %, 3.3 %, and 8.9 % for bluestem, excelsior, and Douglas fir, respectively, which were significantly larger than small (10 cm diameter) fires burning simple two and three carbon hydrocarbons. Further work is needed to improve the estimate of the soot yield since it is calculated using a mass-specific extinction coefficient typical of soot and not a value more typical of particulate matter produced during pyrolysis and smoldering combustion.
6. The peak HRR of the excelsior fires was a function of ignition orientation and bulk density. As expected, the upward spreading fires gave rise to larger peak HRRs than those spreading downward. The horizontally oriented fires (Tests 31 and 32) also spread slower and had smaller PHRRs than the upward-spreading fires.

These measurements of global burning properties can provide guidance to the development of wildland fire models. Radiative fractions, CO yields, and soot yields are all typically prescribed in physics-based wildland fire models. Although more work is required to evaluate the full range of relevant vegetation species, these findings provide a starting point and can serve as an indication of which properties may be (relatively) species-independent (but moisture dependent), such as radiant fraction, and those which appear linked to the species, such as CO yield. The degree to which these differences are related to plant chemistry versus plant structure is also open to further exploration. This work also highlights the uncertainties which can be passed from measurement to model when applying techniques established for gaseous and liquid fuels to complex solid fuels like vegetation. For example, using a global radiant fraction in a model of emission from flaming combustion may introduce uncertainties if emission from the solid phase has a significant effect on the global value. Measurement results and the video recordings of the experiments described in this report are available as part of the NIST Fire Calorimetry Database (FCD) [10].

5. References

[1] Hall, S., *Fire Loss in the United States in 2022*, National Fire Protection Association (NFPA), Quincy, MA, November 2023, https://www.nfpa.org/education-and-research/research/nfpa-research/fire-statistical-reports/fire-loss-in-the-united-states.

[2] Wildland Fire Statistics, National Fire Protection Association (NFPA), website accessed on 5/8/2024: https://www.nfpa.org/education-and-research/research/nfpa-research/fire-statistical-reports/wildland-fire-statistics.

[3] Overholt, K. J., Cabrera, J., Kurzawski, A., Koopersmith, M. and Ezekoye, O. A., Characterization of Fuel Properties and Fire Spread Rates for Little Bluestem Grass, *Fire Technology*, ***50***, 9-38, (2014), http://doi.org/10.1007/s10694-012-0266-9.

[4] Overholt, K. J., Kurzawski, A. J., Cabrera, J., Koopersmith, M. and Ezekoye, O. A., Fire Behavior and Heat Fluxes for Lab-Scale Burning of Little Bluestem Grass, *Fire Safety Journal*, ***67***, 70-81, (2014), http://doi.org/10.1016/j.firesaf.2014.05.007.

[5] Marchand, A., Ferriere, S., Collin, A., Boulet, P., Acem, Z., Demeurie, F. and Morel, J. Y., Vegetation Fire Spread Database: 85 Wood Wool Shaving Experiments at Laboratory Scale, *Fire Safety Journal*, ***109***, 102870, (2019), https://doi.org/10.1016/j.firesaf.2019.102870.

[6] Finney, M. A., Cohen, J. D., Grenfell, I. C. and Yedinak, K. M., An Examination of Fire Spread Thresholds in Discontinuous Fuel Bedsa, *International Journal of Wildland Fire*, ***19***, 163-170, (2010), https://doi.org/10.1071/WF07177.

[7] Catchpole, W. R., Catchpole, E. A., Butler, B. W., Rothermel, R. C., Morris, G. A. and Latham, D. J., Rate of Spread of Free-Burning Fires in Woody Fuels in a Wind Tunnel, *Combustion Science and Technology*, ***131***, 1-37, (1998), https://www.tandfonline.com/doi/abs/10.1080/00102209808935753.

[8] Schneider, L., Betting, B., Patterson, M., Skowronski, N. and Simeoni, A., Experimental Study of Fire Spread through Discontinuous Fuels without Flame Contact, *Fire Safety Journal*, ***120***, 103066, (2021), https://doi.org/10.1016/j.firesaf.2020.103066.

[9] Mell, W., Maranghides, A., McDermott, R. and Manzello, S. L., Numerical Simulation and Experiments of Burning Douglas Fir Trees, *Combustion and Flame*, ***156***, 2023-2041, (2009), http://doi.org/10.1016/j.combustflame.2009.06.015.

[10] Fire Calorimetry Database (FCD), National Institute of Standards and Technology, Gaithersburg MD, https://www.nist.gov/el/fcd (accessed on Sep. 1, 2024).

[11] Heskestad, G., SFPE Handbook of Fire Protection Engineering, 5th edition, Society of Fire Protection Engineers, Springer, 2016, https://www.sfpe.org/publications/handbooks/sfpehandbook.

[12] Bigda, K., *Christmas Tree Fire Safety Requirements*, National Fire Protection Association (NFPA), , Quincy, MA, November, 2021, https://www.nfpa.org/news-blogs-and-articles/blogs/2021/11/12/christmas-tree-fire-safety-requirements.

[13] Babrauskas, V., Heat Release Rates, In: SFPE Handbook of Fire Protection Engineering, M. J. Hurley, et al., Springer, New York, NY, (2016), http://doi.org/10.1007/978-1-4939-2565-0_26.

[14] Bryant, R. A. and Bundy, M. F., *The NIST 20 MW Calorimetry Measurement System for Large-Fire Research*, NIST Technical Note 2077, National Institute of Standards and Technology, Gaithersburg, MD, December 2019, https://doi.org/10.6028/NIST.TN.2077.

[15] Otsu, N., A Threshold Selection Method from Gray-Level Histograms, *IEEE transactions on systems, man, and cybernetics*, ***9***, 62-66, (1979), http://doi.org/10.1109/TSMC.1979.4310076.
[16] Di Cristina, G., Falkenstein-Smith, R., Kim, I., Wessies, S., Bundy, M. and Zammarano, M., Towards Fire Safe and Flame-Retardant-Free Upholstered Furniture, *Proceedings of the Combustion Institute*, ***40***, 105399, (2024), https://doi.org/10.1016/j.proci.2024.105399.
[17] Bundy, M., *User's Guide for Fire Calorimetry Database (FCD)*, National Institute of Standards and Technology, Gaithersburg, MD, 2020, https://www.nist.gov/system/files/documents/2020/11/19/FCD_User_Guide_v4a.pdf.
[18] Mulholland, G. W. and Croarkin, C., Specific Extinction Coefficient of Flame Generated Smoke, *Fire and Materials*, ***24***, 227-230, (2000), https://doi.org/10.1002/1099-1018(200009/10)24:5<227::AID-FAM742>3.0.CO;2-9.
[19] Seader, J. D. and Einhorn, I. N., Some Physical, Chemical, Toxicological, and Physiological Aspects of Fire Smokes, *Symposium (International) on Combustion*, ***16***, 1423-1445, (1977), https://doi.org/10.1016/S0082-0784(77)80426-8.
[20] Sung, K., Chen, J., Bundy, M., Fernandez, M. and Hamins, A., *The Thermal Character of a 1 m Methanol Pool Fire*, NIST Technical Note 2083, Rev.1, National Institute of Standards and Technology, Gaithersburg, MD, June 2021, https://doi.org/10.6028/NIST.TN.2083r1.
[21] Modak, A. T., Thermal Radiation from Pool Fires, *Combustion and Flame*, ***29***, 177-192, (1977), https://doi.org/10.1016/0010-2180(77)90106-7.
[22] *Wood Handbook—Wood as an Engineering Material*, General Technical Report FPL-GTR-282, Madison, WI: U.S. Department of Agriculture, Forest Service, Forest Products Laboratory., 2021, https://www.fs.usda.gov/research/treesearch/62200.
[23] Dietenberger, M., Update for Combustion Properties of Wood Components, *Fire and Materials*, ***26***, 255-267, (2002), https://doi.org/10.1002/fam.807.
[24] Simeoni, A., Salinesi, P. and Morandini, F., Physical Modelling of Forest Fire Spreading through Heterogeneous Fuel Beds, *International Journal of Wildland Fire*, ***20***, 625-632, (2011), https://doi.org/10.1071/WF09006.
[25] Safdari, M.-S., Rahmati, M., Amini, E., Howarth, J. E., Berryhill, J. P., Dietenberger, M., Weise, D. R. and Fletcher, T. H., Characterization of Pyrolysis Products from Fast Pyrolysis of Live and Dead Vegetation Native to the Southern United States, *Fuel*, ***229***, 151-166, (2018), https://doi.org/10.1016/j.fuel.2018.04.166.
[26] Leroy, V., Cancellieri, D. and Leoni, E., Relation between Forest Fuels Composition and Energy Emitted during Their Thermal Degradation, *Journal of Thermal Analysis and Calorimetry*, ***96***, 293-300, (2009), https://doi.org/10.1007/s10973-008-9587-9.
[27] Susott, R., Degroot, W. and Shafizadeh, F., Heat Content of Natural Fuels, *Journal of Fire and Flammability*, ***6***, 311-325, (1975).
[28] Parker, W. J. and Levan, S. L., Kinetic Properties of the Components of Douglas-Fir and the Heat of Combustion of Their Volatile Pyrolysis Products, *Wood and Fiber Science*, ***21***, 289-305, (1989), https://wfs.swst.org/index.php/wfs/article/view/1687.
[29] Susott, R. A., Characterization of the Thermal Properties of Forest Fuels by Combustible Gas Analysis, *Forest Science*, ***28***, 404-420, (1982), https://academic.oup.com/forestscience/article-abstract/28/2/404/4656170.

[30] McCarter, R. J. and Broido, A., Radiative and Convective Energy from Wood Crib Fires, In: Pyrodynamics, Gordon & Breach, Science Publishers Ltd., Northern Ireland, (1965), https://apps.dtic.mil/sti/citations/AD0638751.

[31] Weise, D. R., Fletcher, T. H., Johnson, T. J., Hao, W. M., Dietenberger, M., Princevac, M., Butler, B. W., McAllister, S. S., O'Brien, J. J., Louise Loudermilk, E., Ottmar, R. D., Hudak, A. T., Kato, A., Shotorban, B., Mahalingam, S., Myers, T. L., Palarea-Albaladejo, J. and Baker, S. P., Comparing Gas Composition from Fast Pyrolysis of Live Foliage Measured in Bench-Scale and Fire-Scale Experiments, *International Journal of Wildland Fire*, ***33***, (2024), https://doi.org/10.1071/WF23200.

[32] Garg, P., Roche, T., Eden, M., Matz, J., Oakes, J. M., Bellini, C. and Gollner, M. J., Effect of Moisture Content and Fuel Type on Emissions from Vegetation Using a Steady State Combustion Apparatus, *International Journal of Wildland Fire*, ***31***, 14-23, (2022), https://doi.org/10.1071/WF20118.

[33] Johnsson, E. L., Di Christina, G., Mueller, E., Bundy, M., Chakalis, A., Fernandez, M. and Hamins, A., *The Burning Characteristics of 3 m to 6 m Dry Douglas-Fir Trees*, NIST Technical Note 2327, National Institute of Standards and Technology, Gaithersburg, MD, 2025, https://doi.org/10.6028/NIST.TN.2327.

[34] Khan, M. M., Tewarson, A. and Chaos, M., Combustion Characteristics of Materials and Generation of Fire Products, Chapter 36, In: SFPE Handbook of Fire Protection Engineering, 5th Edition, Socierty of Fire Protection Engineers, Springer, (2016), https://www.sfpe.org/publications/handbooks/sfpehandbook.

[35] Cheung, W. K., Zeng, Y., Lin, S. and Huang, X., Modelling Carbon Monoxide Transport and Hazard from Smouldering for Building Fire Safety Design Analysis, *Fire Safety Journal*, ***140***, 103895, (2023), https://doi.org/10.1016/j.firesaf.2023.103895.

[36] Taylor, B. N. and Kuyatt, C. E., *Guidelines for Evaluating and Expressing the Uncertainty of NIST Measurement Results*, NIST Technical Note 1297, National Institute of Standards and Technology, Gaithersburg, MD, September 1994.

[37] Pitts, W. M., Murthy, A. V., De Ris, J. L., Filtz, J.-R., Nygård, K., Smith, D. and Wetterlund, I., Round Robin Study of Total Heat Flux Gauge Calibration at Fire Laboratories, *Fire Safety Journal*, ***41***, 459-475, (2006), https://dx.doi.org/10.1016/j.firesaf.2006.04.004.

[38] National Instruments Inc., *SCXI-1600 User Manual and Specifications*, 2004.

Appendix A. Test Method Details

Table A1 lists the exhaust hood size, load cell model, and heat flux gauge locations used for each test. Refer to Fig. 5 and Fig. B5 which provide schematic diagrams of the experimental configuration. The reference values of *r*, *z*, and *Θ* are the exhaust duct center, the bottom of the specimen, and the opening of the mesh surrounding the test section as seen in the figure.

Table A1. The exhaust hood size, load cell model, and heat flux gauge locations.

Test	Hood size (m, m)	Load Cell*	HF_V0 (r, z, Θ) (m, m, deg)	HF_V1 (r, z, Θ) (m, m, deg)	HF_V2 (r, z, Θ) (m, m, deg)	HF_V3 (r, z, Θ) (m, m, deg)	HF_V4 (r, z, Θ) (m, m, deg)	HF_V5 (r, z, Θ) (m, m, deg)	HF_V6 (r, z, Θ) (m, m, deg)	HF_V7 (r, z, Θ) (m, m, deg)	HF_H1 (r, z, Θ) (m, m, deg)	HF_H2 (r, z, Θ) (m, m, deg)	HF_H3 (r, z, Θ) (m, m, deg)	HF_H4 (r, z, Θ) (m, m, deg)
1	3, 3	P	1.83, 0.02, 135	1.83, 0.41, 135	1.83, 1.03, 135	1.83, 1.65, 135	1.83, 2.24, 135	2.08, 1.03, 225	2.14, 1.03, 315	2.08, 1.03, 45	0.08, 0, 135	0.12, 0, 135	0.39, 0, 135	1.75, 0, 135
2	3, 3	P	1.83, 0.02, 135	1.83, 0.41, 135	1.83, 1.03, 135	1.83, 1.65, 135	1.83, 2.24, 135	2.08, 1.03, 225	2.14, 1.03, 315	2.08, 1.03, 45	0.08, 0, 135	0.12, 0, 135	0.39, 0, 135	1.75, 0, 135
3	3, 3	P	1.83, 0.02, 135	1.83, 0.41, 135	1.83, 1.03, 135	1.83, 1.65, 135	1.83, 2.24, 135	2.08, 1.03, 225	2.14, 1.03, 315	2.08, 1.03, 45	0.08, 0, 135	0.12, 0, 135	0.39, 0, 135	1.75, 0, 135
4	3, 3	P	1.83, 0.02, 135	1.83, 0.41, 135	1.83, 1.03, 135	1.83, 1.65, 135	1.83, 2.24, 135	2.08, 1.03, 225	2.14, 1.03, 315	2.08, 1.03, 45	0.08, 0, 135	0.12, 0, 135	0.39, 0, 135	1.75, 0, 135
5	3, 3	3D-a	1.78, -0.28, 135	1.78, 0.06, 135	1.78, 0.68, 135	1.78, 1.29, 135	1.78, 2.21, 135	2.08, 0.67, 225	2.14, 0.67, 315	2.11, 0.67, 45	0.09, 0, 135	0.13, 0, 135	0.39, 0, 135	0.69, 0, 135
6	3, 3	3D-a	1.78, -0.28, 135	1.78, 0.06, 135	1.78, 0.68, 135	1.78, 1.29, 135	1.78, 2.21, 135	2.08, 0.67, 225	2.14, 0.67, 315	2.11, 0.67, 45	0.09, 0, 135	0.13, 0, 135	0.39, 0, 135	0.69, 0, 135
7	3, 3	3D-a	1.78, -0.48, 135	1.78, -0.14, 135	1.78, 0.48, 135	1.78, 1.09, 135	1.78, 2.01, 135	2.08, 0.47, 225	2.14, 0.47, 315	2.11, 0.47, 45	0.09, -0.21, 135	0.13, -0.21, 135	0.39, -0.21, 135	1.52, -0.21, 135

Test	Hood size (m, m)	Load Cell*	HF_V0 (r, z, Θ) (m, m, deg)	HF_V1 (r, z, Θ) (m, m, deg)	HF_V2 (r, z, Θ) (m, m, deg)	HF_V3 (r, z, Θ) (m, m, deg)	HF_V4 (r, z, Θ) (m, m, deg)	HF_V5 (r, z, Θ) (m, m, deg)	HF_V6 (r, z, Θ) (m, m, deg)	HF_V7 (r, z, Θ) (m, m, deg)	HF_H1 (r, z, Θ) (m, m, deg)	HF_H2 (r, z, Θ) (m, m, deg)	HF_H3 (r, z, Θ) (m, m, deg)	HF_H4 (r, z, Θ) (m, m, deg)
8	3, 3	3D-a	1.78, -0.48, 135	1.78, -0.14, 135	1.78, 0.48, 135	1.78, 1.09, 135	1.78, 2.01, 135	2.08, 0.47, 225	2.14, 0.47, 315	2.11, 0.47, 45	0.09, -0.21, 135	0.13, -0.21, 135	0.39, -0.21, 135	1.52, -0.21, 135
9	3, 3	3D-a	1.78, -0.48, 135	1.78, -0.14, 135	1.78, 0.48, 135	1.78, 1.09, 135	1.78, 2.01, 135	2.08, 0.47, 225	2.14, 0.47, 315	2.11, 0.47, 45	0.09, -0.21, 135	0.13, -0.21, 135	0.39, -0.21, 135	1.52, -0.21, 135
10	3, 3	3D-a	1.78, -0.48, 135	1.78, -0.14, 135	1.78, 0.48, 135	1.78, 1.09, 135	1.78, 2.01, 135	2.08, 0.47, 225	2.14, 0.47, 315	2.11, 0.47, 45	0.09, -0.21, 135	0.13, -0.21, 135	0.39, -0.21, 135	1.52, -0.21, 135
11	3, 3	3D-a	1.78, -0.48, 135	1.78, -0.14, 135	1.78, 0.48, 135	1.78, 1.09, 135	1.78, 2.01, 135	2.08, 0.47, 225	2.14, 0.47, 315	2.11, 0.47, 45	0.09, -0.21, 135	0.13, -0.21, 135	0.39, -0.21, 135	1.52, -0.21, 135
12	3, 3	3D-a	1.78, -0.37, 135	1.78, -0.03, 135	1.78, 0.59, 135	1.78, 1.20, 135	1.78, 2.12, 135	2.08, 0.58, 225	2.14, 0.58, 315	2.11, 0.58, 45	0.09, -0.21, 135	0.13, -0.21, 135	0.39, -0.21, 135	1.52, -0.21, 135
13	3, 3	3D-a	1.78, -0.37, 135	1.78, -0.03, 135	1.78, 0.59, 135	1.78, 1.20, 135	1.78, 2.12, 135	2.08, 0.58, 225	2.14, 0.58, 315	2.11, 0.58, 45	0.09, -0.21, 135	0.13, -0.21, 135	0.39, -0.21, 135	1.52, -0.21, 135
14	3, 3	3D-a	1.78, -0.37, 135	1.78, -0.03, 135	1.78, 0.59, 135	1.78, 1.20, 135	1.78, 2.12, 135	2.08, 0.58, 225	2.14, 0.58, 315	2.11, 0.58, 45	0.09, -0.21, 135	0.13, -0.21, 135	0.39, -0.21, 135	1.52, -0.21, 135
15	3, 3	3D-a	1.78, -0.48, 135	1.78, -0.14, 135	1.78, 0.48, 135	1.78, 1.09, 135	1.78, 2.01, 135	2.08, 0.47, 225	2.14, 0.47, 315	2.11, 0.47, 45	0.09, -0.21, 135	0.13, -0.21, 135	0.39, -0.21, 135	1.52, -0.21, 135
16	3, 3	3D-a	1.78, -0.48, 135	1.78, -0.14, 135	1.78, 0.48, 135	1.78, 1.09, 135	1.78, 2.01, 135	2.08, 0.47, 225	2.14, 0.47, 315	2.11, 0.47, 45	0.09, -0.21, 135	0.13, -0.21, 135	0.39, -0.21, 135	1.52, -0.21, 135
17	3, 3	3D-a	1.78, -0.48, 135	1.78, -0.14, 135	1.78, 0.48, 135	1.78, 1.09, 135	1.78, 2.01, 135	2.08, 0.47, 225	2.14, 0.47, 315	2.11, 0.47, 45	0.09, -0.21, 135	0.13, -0.21, 135	0.39, -0.21, 135	1.52, -0.21, 135

Test	Hood size (m, m)	Load Cell*	HF_V0 (r, z, Θ) (m, m, deg)	HF_V1 (r, z, Θ) (m, m, deg)	HF_V2 (r, z, Θ) (m, m, deg)	HF_V3 (r, z, Θ) (m, m, deg)	HF_V4 (r, z, Θ) (m, m, deg)	HF_V5 (r, z, Θ) (m, m, deg)	HF_V6 (r, z, Θ) (m, m, deg)	HF_V7 (r, z, Θ) (m, m, deg)	HF_H1 (r, z, Θ) (m, m, deg)	HF_H2 (r, z, Θ) (m, m, deg)	HF_H3 (r, z, Θ) (m, m, deg)	HF_H4 (r, z, Θ) (m, m, deg)
18	3, 3	3D-a	1.78, -0.48, 135	1.78, -0.14, 135	1.78, 0.48, 135	1.78, 1.09, 135	1.78, 2.01, 135	2.08, 0.47, 225	2.14, 0.47, 315	2.11, 0.47, 45	0.09, -0.21, 135	0.13, -0.21, 135	0.39, -0.21, 135	1.52, -0.21, 135
19	3, 3	3D-a	1.78, -0.48, 135	1.78, -0.14, 135	1.78, 0.48, 135	1.78, 1.09, 135	1.78, 2.01, 135	2.08, 0.47, 225	2.14, 0.47, 315	2.11, 0.47, 45	0.09, -0.21, 135	0.13, -0.21, 135	0.39, -0.21, 135	1.52, -0.21, 135
20	3, 3	3D-a	1.78, -0.48, 135	1.78, -0.14, 135	1.78, 0.48, 135	1.78, 1.09, 135	1.78, 2.01, 135	2.08, 0.47, 225	2.14, 0.47, 315	2.11, 0.47, 45	0.09, -0.21, 135	0.13, -0.21, 135	0.39, -0.21, 135	1.52, -0.21, 135
21	3, 3	3D-a	1.78, -0.48, 135	1.78, -0.14, 135	1.78, 0.48, 135	1.78, 1.09, 135	1.78, 2.01, 135	2.08, 0.47, 225	2.14, 0.47, 315	2.11, 0.47, 45	0.09, -0.21, 135	0.13, -0.21, 135	0.39, -0.21, 135	1.52, -0.21, 135
22	3, 3	3D-a	1.78, -0.37, 135	1.78, -0.03, 135	1.78, 0.59, 135	1.78, 1.20, 135	1.78, 2.12, 135	2.08, 0.58, 225	2.14, 0.58, 315	2.11, 0.58, 45	0.09, -0.09, 135	0.13, -0.09, 135	0.39, -0.09, 135	1.52, -0.09, 135
23	3, 3	3D-a	1.78, -0.37, 135	1.78, -0.03, 135	1.78, 0.59, 135	1.78, 1.20, 135	1.78, 2.12, 135	2.08, 0.58, 225	2.14, 0.58, 315	2.11, 0.58, 45	0.09, -0.09, 135	0.13, -0.09, 135	0.39, -0.09, 135	1.52, -0.09, 135
24	6, 6	3D-a	na	4.10, 0.86, 45	4.21, 0.86, 135	4.45, 0.86, 225	4.19, 0.86, 315	5.40, 0.86, 340	na	na	na	na	na	na
25	6, 6	3D-a	na	4.10, 0.86, 45	4.21, 0.86, 135	4.45, 0.86, 225	4.19, 0.86, 315	5.40, 0.86, 340	na	na	na	na	na	na
26	6, 6	3D-a	na	4.10, 0.66, 45	4.21, 0.66, 135	4.45, 0.66, 225	4.19, 0.66, 315	5.40, 0.66, 340	na	na	na	na	na	na
27	6, 6	3D-a	na	4.10, 0.36, 45	4.21, 0.36, 135	4.45, 0.36, 225	4.19, 0.36, 315	5.40, 0.36, 340	na	na	na	na	na	na

Test	Hood size (m, m)	Load Cell*	HF_V0 (r, z, Θ) (m, m, deg)	HF_V1 (r, z, Θ) (m, m, deg)	HF_V2 (r, z, Θ) (m, m, deg)	HF_V3 (r, z, Θ) (m, m, deg)	HF_V4 (r, z, Θ) (m, m, deg)	HF_V5 (r, z, Θ) (m, m, deg)	HF_V6 (r, z, Θ) (m, m, deg)	HF_V7 (r, z, Θ) (m, m, deg)	HF_H1 (r, z, Θ) (m, m, deg)	HF_H2 (r, z, Θ) (m, m, deg)	HF_H3 (r, z, Θ) (m, m, deg)	HF_H4 (r, z, Θ) (m, m, deg)
28	6, 6	3D-a	na	4.10, 0.86, 45	4.21, 0.86, 135	4.45, 0.86, 225	4.19, 0.86, 315	5.40, 0.86, 340	na	na	na	na	na	na
29	6, 6	3D-a	na	4.10, 0.86, 45	4.21, 0.86, 135	4.45, 0.86, 225	2.98, 1.25, 315	3.98, 1.25, 340	na	na	na	na	na	na
30	6, 6	3D-a	na	4.10, 0.86, 45	4.21, 0.86, 135	4.45, 0.86, 225	2.98, 1.25, 315	3.98, 1.25, 340	na	na	na	na	na	na
31	6, 6	3D-a	na	4.10, 0.56, 45	4.21, 0.56, 135	4.45, 0.56, 225	2.98, 1.54, 315	3.98, 1.54, 340	na	na	na	na	na	na
32	6, 6	3D-a	na	4.10, 0.56, 45	4.21, 0.56, 135	4.45, 0.56, 225	2.98, 1.54, 315	3.98, 1.54, 340	na	na	na	na	na	na
33	6, 6	3D-a	na	4.10, 0.86, 45	4.21, 0.86, 135	4.45, 0.86, 225	2.98, 1.25, 315	3.98, 1.25, 340	na	na	na	na	na	na
34	6, 6	3D-a	na	4.10, 0.86, 45	4.21, 0.86, 135	4.45, 0.86, 225	2.98, 1.25, 315	3.98, 1.25, 340	na	na	na	na	na	na
35	6, 6	3D-a	na	4.10, 0.66, 45	4.21, 0.66, 135	4.45, 0.66, 225	2.98, 1.44, 315	3.98, 1.44, 340	na	na	na	na	na	na
36	6, 6	3D-a	na	4.10, 0.36, 45	4.21, 0.36, 135	4.45, 0.36, 225	2.98, 1.74, 315	3.98, 1.74, 340	na	na	na	na	na	na
37	6, 6	3D-a	na	4.07, 1.05, 45	4.07, 1.05, 135	4.07, 1.05, 225	4.07, 1.05, 315	5.21, 1.05, 340	na	na	na	na	na	na

Test	Hood size (m, m)	Load Cell*	HF_V0 (r, z, ϴ) (m, m, deg)	HF_V1 (r, z, ϴ) (m, m, deg)	HF_V2 (r, z, ϴ) (m, m, deg)	HF_V3 (r, z, ϴ) (m, m, deg)	HF_V4 (r, z, ϴ) (m, m, deg)	HF_V5 (r, z, ϴ) (m, m, deg)	HF_V6 (r, z, ϴ) (m, m, deg)	HF_V7 (r, z, ϴ) (m, m, deg)	HF_H1 (r, z, ϴ) (m, m, deg)	HF_H2 (r, z, ϴ) (m, m, deg)	HF_H3 (r, z, ϴ) (m, m, deg)	HF_H4 (r, z, ϴ) (m, m, deg)
38	6, 6	3D-a	na	4.07, 1.05, 45	4.07, 1.05, 135	4.07, 1.05, 225	4.07, 1.05, 315	5.21, 1.05, 340	na	na	na	na	na	na
39	6, 6	3D-a	na	4.07, 1.05, 45	4.07, 1.05, 135	4.07, 1.05, 225	4.07, 1.05, 315	5.21, 1.05, 340	na	na	na	na	na	na
40	6, 6	3D-a	na	4.07, 1.05, 45	4.07, 1.05, 135	4.07, 1.05, 225	4.07, 1.05, 315	5.21, 1.05, 340	na	na	na	na	na	na
41	6, 6	3D-a	na	4.07, 1.05, 45	4.07, 1.05, 135	4.07, 1.05, 225	4.07, 1.05, 315	5.21, 1.05, 340	na	na	na	na	na	na
42	6, 6	3D-a	na	4.07, 1.05, 45	4.07, 1.05, 135	4.07, 1.05, 225	4.07, 1.05, 315	5.21, 1.05, 340	na	na	na	na	na	na
43	6, 6	3D-a	na	4.07, 1.05, 45	4.07, 1.05, 135	4.07, 1.05, 225	4.07, 1.05, 315	5.21, 1.05, 340	na	na	na	na	na	na
44	6, 6	R	na	5.30, 1.69, 45	5.29, 1.72, 135	5.32, 1.66, 225	5.26, 1.67, 315	6.00, 1.67, 340	na	na	na	na	na	na
45	6, 6	R	na	4.00, 1.69, 45	4.00, 1.69, 135	4.00, 1.69, 225	4.00, 1.69, 315	4.50, 1.69, 340	na	na	na	na	na	na
46	6, 6	R	na	4.00, 1.69, 45	4.00, 1.69, 135	4.00, 1.69, 225	4.00, 1.69, 315	4.50, 1.69, 340	na	na	na	na	na	na
47	6, 6	R	na	4.00, 1.69, 45	4.00, 1.69, 135	4.00, 1.69, 225	4.00, 1.69, 315	4.50, 1.69, 340	na	na	na	na	na	na

Test	Hood size (m, m)	Load Cell*	HF_V0 (r, z, Θ) (m, m, deg)	HF_V1 (r, z, Θ) (m, m, deg)	HF_V2 (r, z, Θ) (m, m, deg)	HF_V3 (r, z, Θ) (m, m, deg)	HF_V4 (r, z, Θ) (m, m, deg)	HF_V5 (r, z, Θ) (m, m, deg)	HF_V6 (r, z, Θ) (m, m, deg)	HF_V7 (r, z, Θ) (m, m, deg)	HF_H1 (r, z, Θ) (m, m, deg)	HF_H2 (r, z, Θ) (m, m, deg)	HF_H3 (r, z, Θ) (m, m, deg)	HF_H4 (r, z, Θ) (m, m, deg)
48	6, 6	3D-a,b	na	4.00, 0.91, 45	4.00, 0.91, 135	4.00, 0.91, 225	4.00, 0.91, 315	4.50, 0.91, 340	na	na	na	na	na	na
49	6, 6	3D-a,b	na	4.00, 0.91, 45	4.00, 0.91, 135	4.00, 0.91, 225	4.00, 0.91, 315	4.50, 0.91, 340	na	na	na	na	na	na
50	3, 3	3D-a	na	2.07, 0.84, 45	2.09, 0.84, 135	2.11, 0.86, 225	2.13, 0.84, 315	na	na	na	0.13, -0.19, 135	na	na	na
51	3, 3	3D-a	na	2.07, 0.84, 45	2.09, 0.84, 135	2.11, 0.86, 225	2.13, 0.84, 315	na	na	na	0.13, -0.19, 135	na	na	na
52	3, 3	3D-a	na	2.07, 0.84, 45	2.09, 0.84, 135	2.11, 0.86, 225	2.13, 0.84, 315	na	na	na	0.13, -0.19, 135	na	na	na
53	3, 3	3D-a	na	2.07, 0.84, 45	2.09, 0.84, 135	2.11, 0.86, 225	2.13, 0.84, 315	na	na	na	0.13, -0.19, 135	na	na	na
54	3, 3	3D-a	na	2.07, 0.84, 45	2.09, 0.84, 135	2.11, 0.86, 225	2.13, 0.84, 315	na	na	na	0.13, -0.19, 135	na	na	na
55	3, 3	3D-a	na	2.07, 0.84, 45	2.09, 0.84, 135	2.11, 0.86, 225	2.13, 0.84, 315	na	na	na	0.13, -0.19, 135	na	na	na
56	3, 3	3D-a	na	2.07, 0.84, 45	2.09, 0.84, 135	2.11, 0.86, 225	2.13, 0.84, 315	na	na	na	0.13, -0.19, 135	na	na	na

*Load cells:
- **3D**-Interface (ZM3DW): 3D-a (SN:72159), 3D-b (SN:72157)
- **P**-Precisa (XB-6200C)
- **R**-RADWAG (APP 60.R1)

Table A2 lists the Nikon D500 camera location and exposure for each test.

Table A2. Camera (Nikon D500) location and exposure for each test.

Test	Location: (*r*, *z*) (m, m)	Exposure (F, ISO)
1	2.44,1.17	4, 400
2	2.44,1.17	3.2, 3200
3	2, 1.07	3.5, 1600
4	2, 1.07	10, 10000
5	2, 1.07	10, 10000
6	2, 1.07	10, 10000
7	2, 1.07	10, 10000
8	2, 1.07	10, 10000
9	2, 1.07	10, 10000
10	2, 1.07	10, 10000
11	2, 1.07	10, 10000
12	2, 1.07	10, 10000
13	2, 1.07	10, 10000
14	3.1, 0.9	10, 10000
15	3.1, 1.07	10, 10000
16	3.1, 1.07	10, 10000
17	3.1, 1.07	10, 10000
18	3.1, 1.07	10, 10000
19	3.1, 1.07	10, 10000
20	3.1, 1.07	10, 10000
21	3.1, 1.07	10, 10000
22	3.1, 1.07	10, 10000
23	3.1, 1.07	10, 10000
24	5.4, 1.14	10, 10000
25	5.4, 1.14	10, 10000
26	5.4, 1.14	10, 10000
27	5.4, 1.44	10, 10000
28	5.4, 1.44	10, 10000
29	5.4, 1.44	10, 10000
30	5.4, 1.44	10, 10000
31	5.4, 1.44	10, 10000
32	5.4, 1.44	10, 10000
33	5.4, 1.44	10, 10000
34	5.4, 1.44	10, 10000
35	5.4, 1.44	10, 10000
36	5.4, 1.44	10, 10000
37	5.4, 1.44	10, 10000
38	5.4, 1.44	10, 10000
39	5.4, 1.44	10, 10000

Test	**Location: (*r*, *z*) (m, m)**	**Exposure (F, ISO)**
40	5.4, 1.44	10, 10000
41	5.4, 1.44	10, 10000
42	5.4, 1.44	10, 10000
43	5.4, 1.15	10, 10000
44	6.1, 1.45	13, 6400
45	4.5. 1.55	13, 6400
46	4.5. 1.55	13, 6400
47	4.5, 0.96	13, 6400
48	4.4, 1.22	13, 6400
49	4.4, 1.22	13, 6400
50	1.7, 0.3	10, 10000
51	1.7, 0.3	10, 10000
52	1.7, 0.3	10, 10000
53	1.7, 0.3	10, 10000
54	1.7, 0.3	10, 10000
55	1.7, 0.3	10, 10000
56	1.7, 0.3	10, 10000

Appendix B. Uncertainty Analysis

Estimates of uncertainty are evaluated using the method described in Ref. [36]. A series of measurements, denoted by y, can be expressed as a function of its associated independent variables, x_i. The function f contains all quantities that significantly contribute to the measurement: Estimates of uncertainty are evaluated using the method described in Ref. [36]. A series of measurements, denoted by y, can be expressed as a function of its associated independent variables, x_i. The function f contains all quantities that significantly contribute to the measurement:

$$y = f(x_1, x_2, x_3, \cdots, x_N) \tag{B1}$$

In the case that all input variables are uncorrelated, the combined standard uncertainty, $u_c(y)$, is estimated, following *the law of propagation of uncertainty*. The standard deviation of the output estimate, $\sigma_R(y)$ is also considered an uncertainty component. The expanded combined uncertainty, $U_c(y)$, is defined as:

$$U_c(y) = k\sqrt{u_c(y)^2 + \sigma_R(y)^2} \tag{B2}$$

where the coverage factor, k, is taken as equal to 2, so that the expanded (k = 2) combined uncertainty, U_c, defines an interval corresponding to approximately a 95 % confidence level.

B.1. Uncertainty of Mass Loss Measurement

The expanded (k = 2) combined uncertainty of the burning mass loss, $U_c(\Delta m)$, is estimated as below:

$$U_c(\Delta m) = 2\sqrt{u_c(\mathrm{drift})^2 + u_c(\mathrm{cal.})^2} \tag{B3}$$

where u_c(drift) is mass drift due to the core temperature change of the load cell. u_c(cal) is the calibration error, estimated as the slope's error of linear curve fitting. The calibration error of load cell used in each test is listed in Table B1.

Figure B1 shows experimental setup for estimation of signal drift in mass measurements. The collar was heated using a heating tape, which controlled temperature by a transformer. Thermocouples measured the temperature inside the collar and the core temperature of the 3D force sensor (Interface Inc, SN:72157). The water-cooling system in the Fig. B1(a) was turned off during the experiment.

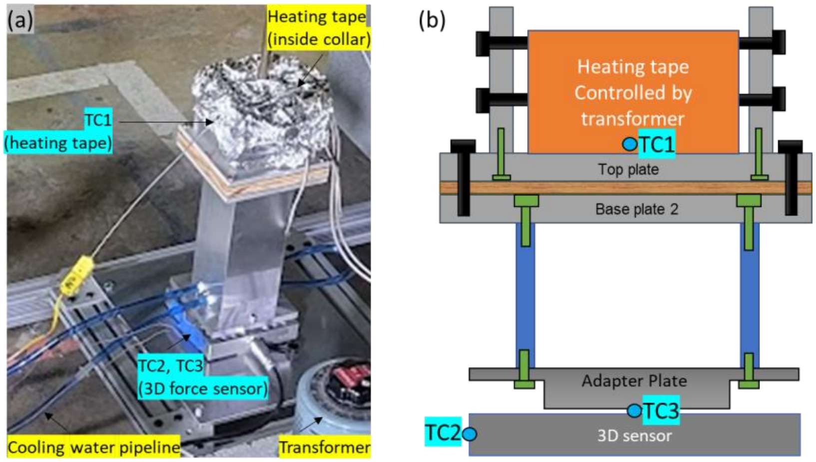

Fig. B1. Experimental setup for estimating signal drift in mass measurements: (a) photograph, (b) schematic diagram.

Figure B2 shows the mass and core temperature of the 3D fore sensor as a function of time. The measured mass is closely correlated with core temperature. Mass drift with the core temperature change was estimated in the heating period of 15 min (highlighted with yellow in Fig. B2).

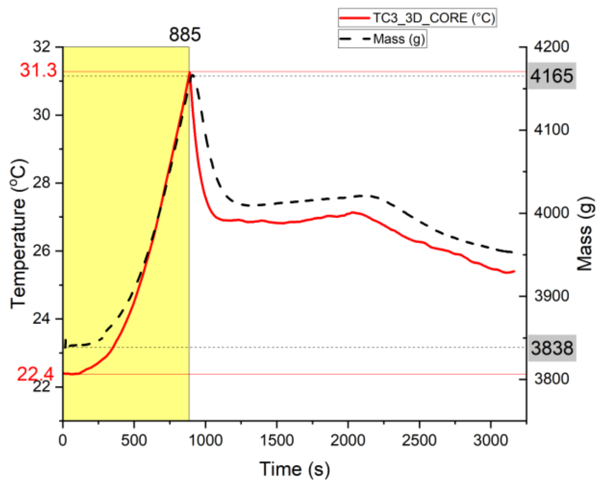

Fig. B2. Mass (solid line) and core temperature of the 3D force sensor (dashed line) as a function of time.

Mass drift (m_{drift}) and core temperature change (ΔT_{core}) are estimated as:

$$m_{drift} = m - m_i$$
$$\Delta T_{core} = T_{core} - T_{core,i} \tag{B4}$$

where, m_i and T_{core} are the initial mass and core temperature at t = 0 s. Figure B3 shows the mass drift as a function of the core temperature change. The mass drift is linearly proportional to the core temperature change. The drift rate of mass ($\dot{m}_{drift}$) is 30.6 g/°C ± 0.06 g/°C when ΔT_{core} is less than 1 °C. For the 3D force sensor, the mass drift was calculated as $\dot{m}_{drift} \times \Delta T_{core}$.

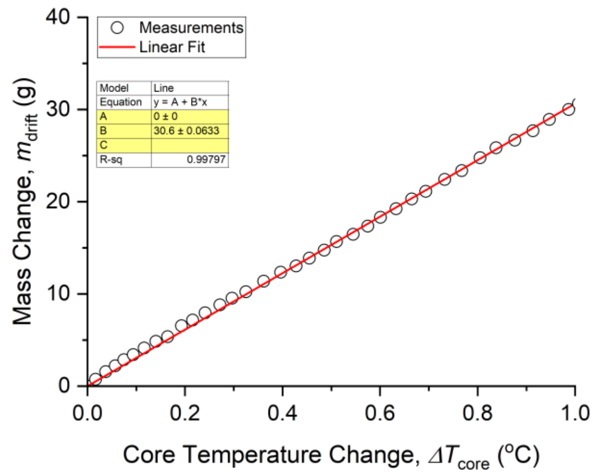

Fig. B3. Mass drift (m_{drift}) as a function of the core temperature change (ΔT_{core}) for the 3D force sensor used in many of the experiments (see Table A1 for details).

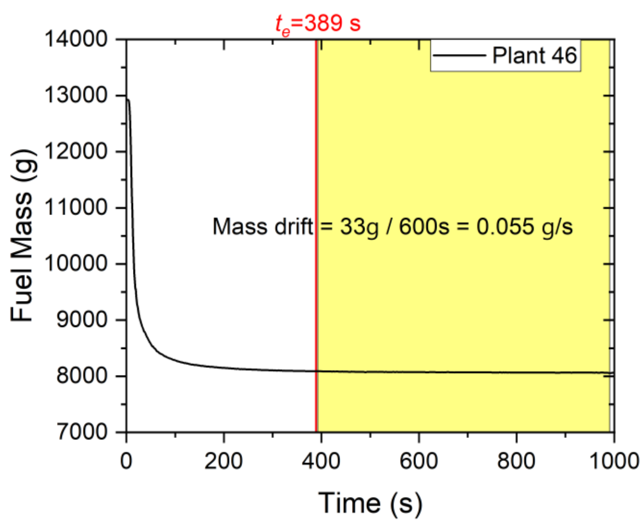

Fig. B4. Mass measured by the RADWAG load cell used in Test 46 as a function of time.

The rate of mass drift ($\dot{m}_{drift}$) of RADWAG (R) and PRECISA (P) load cells was determined by measuring the change in mass over a period of at least 5 min immediately after the fire was extinguished. The $\dot{m}_{drift}$ of RADWAG and PRECISA load cells was 0.055 g/s and 0.003 g/s, respectively. For the RADWAG and PRECISA load cells, the mass drift was calculated as $\dot{m}_{drift} \times t_{burning}$. Table B1 lists the loadcell model, mass drift, core temperature change of load cell, mass loss and uncertainty terms in Eq. (B3).

Table B1. Mass drift, the burning mass loss, and the uncertainties of mass drift and calibration in each test. The expanded (k=2) combined uncertainty of the burning mass loss is also shown.

Test no.	Specimen	Load cell*	$t_{burning}$ (s)	ΔT_{core} (s)	m_{drift} (g)	Δm (g)	u_c(drfit) (%)	u_c(cal) (%)	$U_c(\Delta m)$ (%)
1	bluestem	P	127	na	0.4	80	0.4	0.05	0.9
2	bluestem	P	224	0.04	0.6	68	0.9	0.05	2
3	bluestem	P	146	0.06	0.4	98	0.4	0.05	0.8
4	bluestem	P	133	-0.07	0.4	34	1.1	0.05	2
5	bluestem	3D-a	117	0.04	1.1	24	1.2	0.03	2
6	bluestem	3D-a	120	0.04	1.1	19	1.2	0.03	2
7	excelsior	3D-a	151	0.003	0.1	134	0.1	0.03	0.1
8	excelsior	3D-a	154	0.004	0.1	138	0.1	0.03	0.2
9	excelsior	3D-a	138	0.04	1.1	137	0.8	0.03	2
10	excelsior	3D-a	102	1E-4	0.004	140	0.003	0.03	0.1
11	excelsior	3D-a	142	0.007	0.2	147	0.1	0.03	0.3
12	DF tree	3D-a	64	0.03	0.8	137	0.6	0.03	1
13	DF tree	3D-a	104	0.008	0.2	153	0.2	0.03	0.3
14	DF tree	3D-a	101	0.009	0.3	158	0.2	0.03	0.3
15	excelsior	3D-a	106	0.02	0.5	138	0.4	0.03	0.8
16	excelsior	3D-a	84	0.001	0.04	62	0.1	0.03	0.2
17	excelsior	3D-a	88	0.02	0.6	54	1.1	0.03	2
18	excelsior	3D-a	110	0.002	0.07	56	0.1	0.03	0.3
19	excelsior	3D-a	125	0.003	0.1	57	0.2	0.03	0.3
20	excelsior	3D-a	117	0.009	0.3	55	0.5	0.03	1
21	excelsior	3D-a	78	0.02	0.6	56	1.0	0.03	2
22	DF tree	3D-a	147	0.02	0.7	178	0.4	0.03	0.7
23	DF tree	3D-a	125	0.010	0.3	262	0.1	0.03	0.2
24	bluestem	3D-a	62	0.06	1.8	74	2.4	0.03	5
25	bluestem	3D-a	74	0.02	0.6	76	0.8	0.03	2
26	excelsior	3D-a	77	0.002	0.07	139	0.1	0.03	0.1
27	excelsior	3D-a	74	0.09	2.6	252	1.0	0.03	2
28	bluestem	3D-a	52	9E-4	0.03	48	0.1	0.03	0.1
29	bluestem	3D-a	83	0.06	1.9	93	2.0	0.03	4
30	bluestem	3D-a	37	0.04	1.1	26	4.3	0.03	9
31	excelsior	3D-a	84	0.03	0.8	144	0.6	0.03	1
32	excelsior	3D-a	89	0.1	3.4	143	2.4	0.03	5
33	bluestem	3D-a	116	0.02	0.7	48	1.4	0.03	3
34	bluestem	3D-a	294	0.05	1.7	51	3.3	0.03	7
35	excelsior	3D-a	62	0.02	0.7	89	0.8	0.03	2
36	excelsior	3D-a	62	0.05	1.5	116	1.3	0.03	3
37	DF tree	3D-a	113	0.06	1.8	123	1.5	0.03	3
38	DF tree	3D-a	152	0.04	1.2	194	0.6	0.03	1
39	DF tree	3D-a	142	0.10	3.0	153	1.9	0.03	4

Test no.	Specimen	Load cell*	$t_{burning}$ (s)	ΔT_{core} (s)	m_{drift} (g)	Δm (g)	u_c(drfit) (%)	u_c(cal) (%)	$U_c(\Delta m)$ (%)
40	DF tree	3D-a	119	0.04	1.4	82	1.7	0.03	3
41	DF tree	3D-a	292	0.04	1.2	37	3.1	0.03	6
42	DF tree	3D-a	130	0.04	1.3	77	1.6	0.03	3
43	DF tree	3D-a	166	0.01	0.4	242	0.2	0.03	0.3
44	DF tree	R	306	na	17	4726	0.4	0.03	0.7
45	DF tree	R	369	na	20	3201	0.6	0.03	1
46	DF tree	R	389	na	21	4394	0.5	0.03	1
47	DF tree	R	479	na	26	3614	0.7	0.03	2
48	excelsior	3D-a,b	137	0.04	1.2	139	0.9	0.03	2
49	excelsior	3D-a,b	70	0.1	3.5	137	2.5	0.03	5
50	excelsior	3D-a	215	na	na	190	na	0.03	1**
51	excelsior	3D-a	304	na	na	200	na	0.03	1**
52	excelsior	3D-a	209	na	na	192	na	0.03	1**
53	excelsior	3D-a	252	na	na	211	na	0.03	1**
54	excelsior	3D-a	292	na	na	199	na	0.03	1**
55	excelsior	3D-a	323	na	na	192	na	0.03	1**
56	excelsior	3D-a	27	na	na	27	na	0.03	1**

*Load cells:
- **3D**-Interface (ZM3DW): 3D-a (SN:72159), 3D-b (SN:72157)
- **P**-Precisa (XB-6200C)
- **R**- RADWAG (APP 60.R1)

**assumed as the mean uncertainty in excelsior tests.

B.2. Uncertainty of the Estimation of Flame Height

A 0.5m wide x 1m height checkerboard with 5cm x 5 cm cells was used as the reference to correct image distortion caused by parallax effects due to the camera's viewing angle and position. The image resolution averaged 0.3 cm/pixel across all tests.

The expanded (k=2) combined uncertainty of the peak flame height is estimated as:

$$U_c(L_f) = 2\sqrt{u_c(\text{puff})^2 + u_c(\text{cal})^2} \tag{B5}$$

where $u_c(\text{puff})$ is the uncertainty caused by the flame fluctuation near peak flame height. A 1-second moving average was applied to estimate flame height changes over time. The peak flame height was defined as the average over a 1-second period centered at the peak of the moving average curve. And standard deviation of the flame height in the period was estimated as the uncertainty due to flame puffing ($u_c(\text{puff})$), which averaged 9 % across all tests. $u_c(\text{cal})$ is the uncertainty considering the binary image threshold setting, which is 3 %. The expanded (k=2) combined uncertainty, $Uc(L_f)$, averaged 20 % across all tests.

B.3. Uncertainty of the Heat Flux Measurement and the Estimate of Radiative Fraction

The heat flux gauges were calibrated using a secondary standard gauge in a well-characterized calibration facility [37]. The measurement accuracy of the data acquisition system (DAQ, Model: SCXI-1600), $u_c(\mathrm{DAQ})$, is 0.076 % in the application range used here [38]. The uncertainty $u_c(\mathrm{cal})$of the heat flux gauge calibration procedure is estimated as 4.5 % [37]. The heat flux background signal slightly increased during the steady burning period as the fire continuously heated the surroundings. The measured (uncorrected) heat flux can be affected by the temperature of the surroundings (walls, calorimeter hood, and so on). The background heat flux is subtracted from the measured heat flux as described in Ref. [20]. The uncertainty of the background heat flux, $u_c(\mathrm{bg})$ is about 0.10 % for these fast fires. The combined uncertainty for the heat flux measurement is 4.5 % given by:

$$u_c(\dot{q}'') = \sqrt{u_c(\mathrm{bg})^2 + u_c(\mathrm{cal})^2 + u_c(\mathrm{DAQ})^2} \qquad \text{(B6)}$$

Table B2 lists the total radiative emission (TRE$_i$) estimated from each heat flux gauge as well as the mean and expanded combined uncertainty of the radiative fraction, considering Eq. (3) in Section 2.7. The combined expanded (k = 2) uncertainty of the radiative fraction is estimated as:

$$U_c(\chi_{rad}) = 2\sqrt{u_c(\dot{q}'')^2 + u_c(\mathrm{model})^2 + u_c(r)^2 + u_c\left(H_{c,eff}\right)^2} \qquad \text{(B7)}$$

where the term $u_c(r)$ is the positioning uncertainty of the radial distance, which is 1 % in general. Modak [21] suggests that a distance five times the diameter of a fire is far enough away to use a single-point location estimate of the total radiative flux, assuming isotropy. The results show that the flame's radiative power output, assuming radiative isotropy, tends to underestimate the total radiative energy emitted by the flame, with a bias of about 2 % at *r/D* = 5. This is treated in Eq. (B7) as uncertainty in the single point radiation estimate method, $u_c(\mathrm{model})$. The term $u_c(H_{c,eff})$ is the standard deviation of the effective heat of combustion for each fuel type, as listed in Table 3. The average expanded (k = 2) uncertainty of the radiative fraction $U_c(\chi_{rad})$ for all the tests was 27 %.

Table B2. Total radiative emission (TRE$_i$) estimated from the i^{th} heat flux gauge. The mean radiative fraction and its expanded (k=2) combined uncertainty is also listed.

Test	TRE$_1$ (kJ)	TRE$_2$ (kJ)	TRE$_3$ (kJ)	TRE$_4$ (kJ)	TRE$_5$ (kJ)	$\overline{\chi}_{rad}$ (-)	$U_c(\chi_{rad})$ (-)
1	7.2	5.7	5.0	-	-	0.28	0.09
2	6.7	5.3	5.0	-	-	0.31	0.10
3	10.4	8.7	6.3	-	-	0.32	0.11
4	3.5	3.3	2.6	-	-	0.35	0.12
5	2.9	2.2	2.5	-	-	0.40	0.13
6	1.9	1.8	2.3	-	-	0.40	0.13
7	14.7	14.6	14.4	-	-	0.36	0.07
8	14.9	13.7	15.2	-	-	0.35	0.07

Test	TRE$_1$ (kJ)	TRE$_2$ (kJ)	TRE$_3$ (kJ)	TRE$_4$ (kJ)	TRE$_5$ (kJ)	$\overline{\chi}_{rad}$ (-)	$U_c(\chi_{rad})$ (-)
9	14.9	13.8	14.5	-	-	0.35	0.07
10	15.1	13.7	15.1	-	-	0.35	0.07
11	15.8	13.6	14.3	-	-	0.33	0.07
12	6.6	5.1	7.0	-	-	0.14	0.05
13	18.0	16.5	18.8	-	-	0.37	0.13
14	17.2	15.9	16.4	-	-	0.33	0.11
15	15.1	13.8	14.5	-	-	0.35	0.07
16	5.9	5.3	6.4	-	-	0.31	0.06
17	5.3	5.0	5.9	-	-	0.33	0.07
18	5.7	5.1	5.6	-	-	0.32	0.06
19	6.0	4.9	6.2	-	-	0.33	0.07
20	6.1	5.1	5.6	-	-	0.34	0.07
21	5.5	4.7	5.8	-	-	0.31	0.06
22	25.1	21.7	22.4	-	-	0.41	0.14
23	21.1	16.8	19.3	-	-	0.23	0.08
24	2.1	2.0	1.3	1.1	0.6	0.30	0.10
25	1.9	2.0	2.1	1.8	0.8	0.37	0.12
26	3.1	3.5	3.0	3.3	1.8	0.30	0.06
27	5.5	6.5	5.4	5.8	3.4	0.30	0.06
28	1.4	1.2	0.8	1.3	0.8	0.38	0.13
29	2.6	1.7	2.3	4.1	2.0	0.34	0.12
30	0.7	0.5	0.6	1.2	0.5	0.33	0.11
31	2.9	3.3	2.4	6	3.5	0.27	0.05
32	2.5	3.6	3.3	5.7	3.4	0.29	0.06
33	0.8	1.6	0.9	1.8	1.2	0.33	0.11
34	1.3	1.4	1.0	2.2	1.3	0.35	0.12
35	2.0	2.1	2.0	3.7	2.1	0.29	0.06
36	2.8	2.7	2.7	2.9	1.9	0.26	0.05
37	2.1	2.1	2.5	1.5	1.2	0.19	0.07
38	3.7	4.0	4.4	4.3	2.6	0.25	0.09
39	3.9	3.4	3.7	3.8	2.3	0.29	0.10
40	1.8	1.1	2.2	2.1	1.0	0.26	0.09
41	0.5	1.1	0.3	0.3	0.1	0.15	0.05
42	0.7	0.3	1.3	1.6	0.7	0.15	0.05
43	7.5	3.5	8.3	7.2	4.9	0.38	0.13
44	62.5	65.3	72.7	73.4	52.1	0.29	0.10
45	90.9	85.7	92.2	86.9	68.8	0.32	0.11
46	130.2	124.8	135.3	131.6	102.8	0.34	0.12
47	115.2	105.1	113.9	110.9	86.4	0.35	0.12
48	4.4	3.4	3.1	3.2	2.2	0.29	0.06
49	4.2	4.6	3.3	3.6	2.4	0.32	0.06
50	22.5	20.7	21.0	18.4	-	0.36	0.07

Test	TRE$_1$ (kJ)	TRE$_2$ (kJ)	TRE$_3$ (kJ)	TRE$_4$ (kJ)	TRE$_5$ (kJ)	$\overline{\chi}_{rad}$ (-)	$U_c(\chi_{rad})$ (-)
51	22.6	22.2	20.5	20.9	-	0.35	0.07
52	25.0	24.5	22.7	24.5	-	0.41	0.08
53	25.3	24.6	25.7	23.2	-	0.38	0.08
54	24.6	27.9	26.6	25.4	-	0.43	0.09
55	26.4	26.6	25.7	24.3	-	0.44	0.09
56	2.7	2.4	3.0	2.6	-	0.32	0.06

B.3.1. Local Heat Flux Measurements

Heat flux gauges were installed in different configurations based on the NIST calorimeter's hood size, as seen in Fig. 5 and Fig. B5. Figure B6 and Fig. B7 shows the radiative heat flux to the surroundings as a function of time for each test. A very small airflow (10 cm/s) blew just above the two gauges (HF_H1 and HF_H2) closest to the fire to prevent light ash and embers from depositing on the sensor surface.

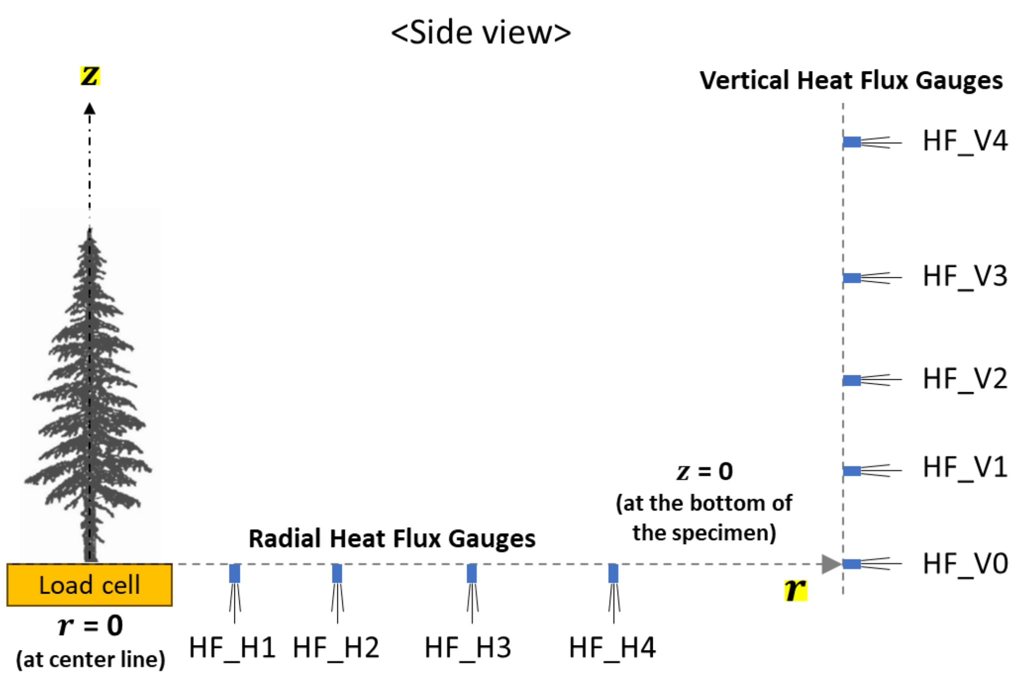

Fig. B5. Schematic diagram of horizontal and vertical arrays of heat flux gauges under a 3 m x 3 m hood.

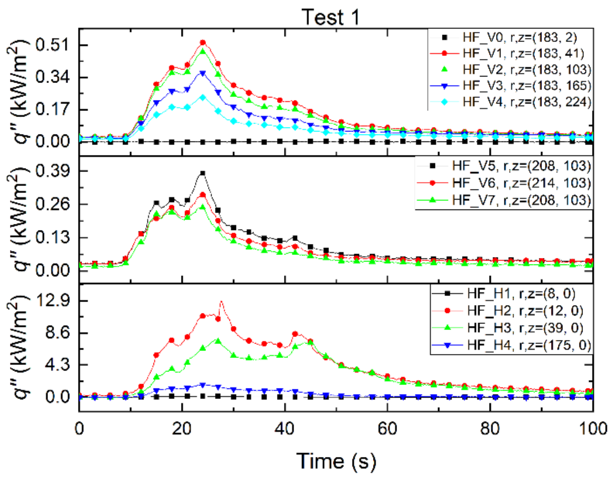
Test 1
HF_V0, r,z=(183, 2)
HF_V1, r,z=(183, 41)
HF_V2, r,z=(183, 103)
HF_V3, r,z=(183, 165)
HF_V4, r,z=(183, 224)
HF_V5, r,z=(208, 103)
HF_V6, r,z=(214, 103)
HF_V7, r,z=(208, 103)
HF_H1, r,z=(8, 0)
HF_H2, r,z=(12, 0)
HF_H3, r,z=(39, 0)
HF_H4, r,z=(175, 0)
q'' (kW/m2)
Time (s)

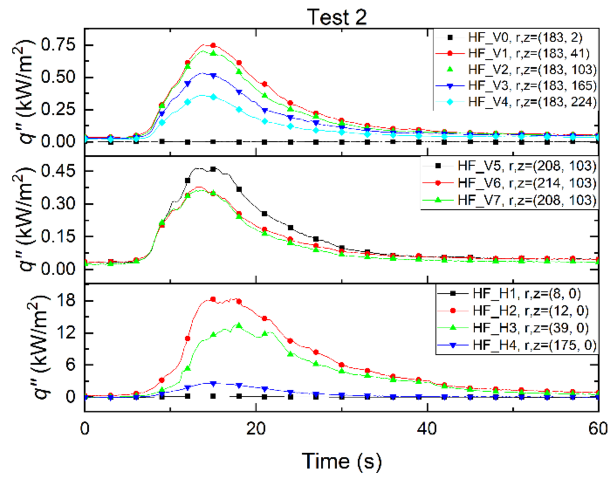
Test 2
HF_V0, r,z=(183, 2)
HF_V1, r,z=(183, 41)
HF_V2, r,z=(183, 103)
HF_V3, r,z=(183, 165)
HF_V4, r,z=(183, 224)
HF_V5, r,z=(208, 103)
HF_V6, r,z=(214, 103)
HF_V7, r,z=(208, 103)
HF_H1, r,z=(8, 0)
HF_H2, r,z=(12, 0)
HF_H3, r,z=(39, 0)
HF_H4, r,z=(175, 0)
q'' (kW/m2)
Time (s)

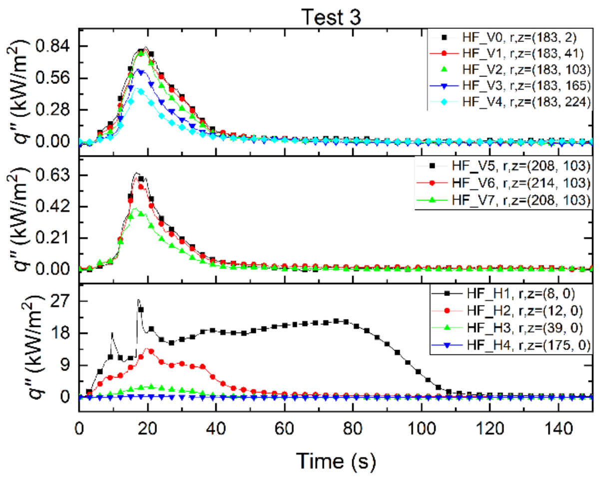
Test 3
HF_V0, r,z=(183, 2)
HF_V1, r,z=(183, 41)
HF_V2, r,z=(183, 103)
HF_V3, r,z=(183, 165)
HF_V4, r,z=(183, 224)
HF_V5, r,z=(208, 103)
HF_V6, r,z=(214, 103)
HF_V7, r,z=(208, 103)
HF_H1, r,z=(8, 0)
HF_H2, r,z=(12, 0)
HF_H3, r,z=(39, 0)
HF_H4, r,z=(175, 0)
q'' (kW/m2)
Time (s)

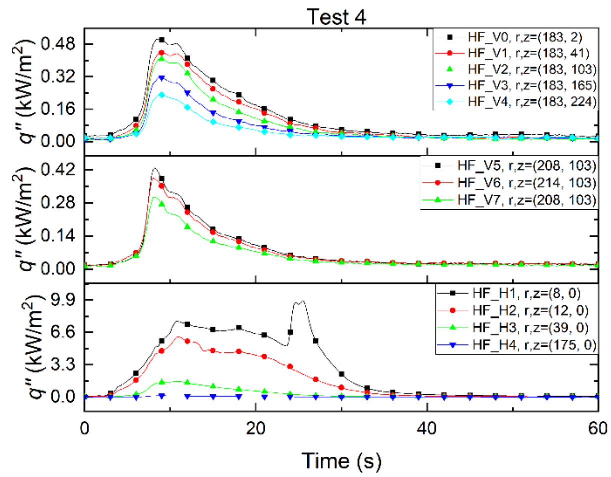
Test 4
HF_V0, r,z=(183, 2)
HF_V1, r,z=(183, 41)
HF_V2, r,z=(183, 103)
HF_V3, r,z=(183, 165)
HF_V4, r,z=(183, 224)
HF_V5, r,z=(208, 103)
HF_V6, r,z=(214, 103)
HF_V7, r,z=(208, 103)
HF_H1, r,z=(8, 0)
HF_H2, r,z=(12, 0)
HF_H3, r,z=(39, 0)
HF_H4, r,z=(175, 0)
q'' (kW/m2)
Time (s)

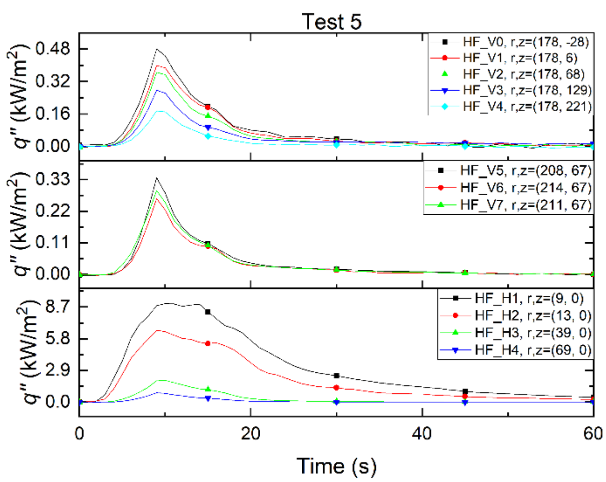
Test 5
HF_V0, r,z=(178, -28)
HF_V1, r,z=(178, 6)
HF_V2, r,z=(178, 68)
HF_V3, r,z=(178, 129)
HF_V4, r,z=(178, 221)
HF_V5, r,z=(208, 67)
HF_V6, r,z=(214, 67)
HF_V7, r,z=(211, 67)
HF_H1, r,z=(9, 0)
HF_H2, r,z=(13, 0)
HF_H3, r,z=(39, 0)
HF_H4, r,z=(69, 0)
q'' (kW/m2)
Time (s)

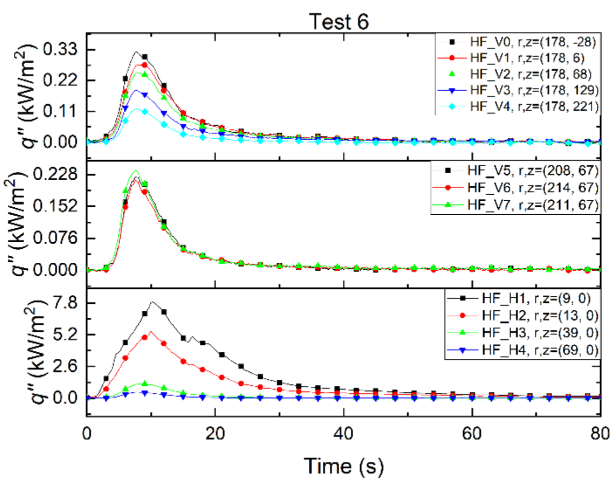
Test 6
HF_V0, r,z=(178, -28)
HF_V1, r,z=(178, 6)
HF_V2, r,z=(178, 68)
HF_V3, r,z=(178, 129)
HF_V4, r,z=(178, 221)
HF_V5, r,z=(208, 67)
HF_V6, r,z=(214, 67)
HF_V7, r,z=(211, 67)
HF_H1, r,z=(9, 0)
HF_H2, r,z=(13, 0)
HF_H3, r,z=(39, 0)
HF_H4, r,z=(69, 0)
q'' (kW/m2)
Time (s)

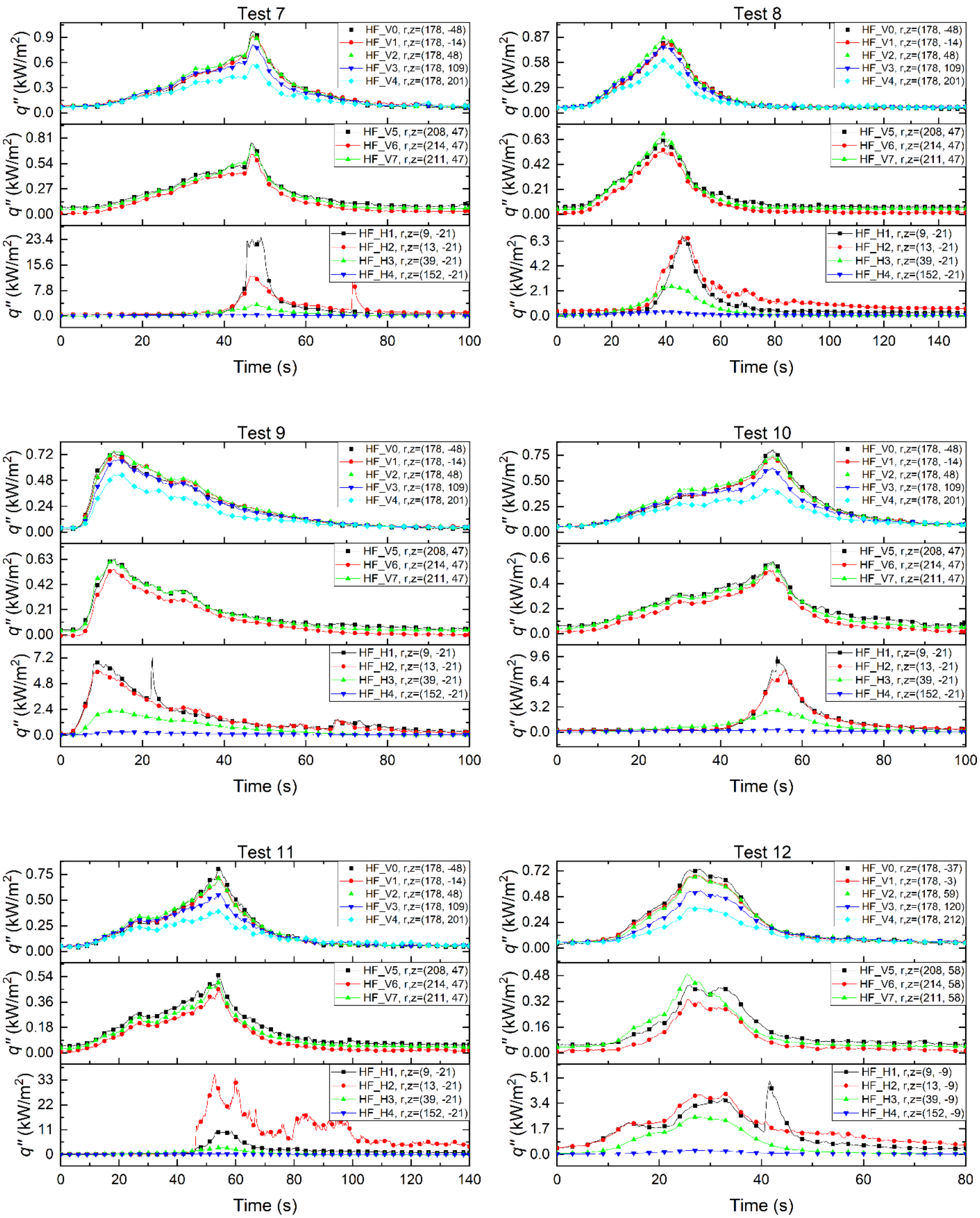
Test 7
HF_V0, r,z=(178, -48)
HF_V1, r,z=(178, -14)
HF_V2, r,z=(178, 48)
HF_V3, r,z=(178, 109)
HF_V4, r,z=(178, 201)
HF_V5, r,z=(208, 47)
HF_V6, r,z=(214, 47)
HF_V7, r,z=(211, 47)
HF_H1, r,z=(9, -21)
HF_H2, r,z=(13, -21)
HF_H3, r,z=(39, -21)
HF_H4, r,z=(152, -21)
q" (kW/m²)
Time (s)
Test 8
HF_V0, r,z=(178, -48)
HF_V1, r,z=(178, -14)
HF_V2, r,z=(178, 48)
HF_V3, r,z=(178, 109)
HF_V4, r,z=(178, 201)
HF_V5, r,z=(208, 47)
HF_V6, r,z=(214, 47)
HF_V7, r,z=(211, 47)
HF_H1, r,z=(9, -21)
HF_H2, r,z=(13, -21)
HF_H3, r,z=(39, -21)
HF_H4, r,z=(152, -21)
q" (kW/m²)
Time (s)
Test 9
HF_V0, r,z=(178, -48)
HF_V1, r,z=(178, -14)
HF_V2, r,z=(178, 48)
HF_V3, r,z=(178, 109)
HF_V4, r,z=(178, 201)
HF_V5, r,z=(208, 47)
HF_V6, r,z=(214, 47)
HF_V7, r,z=(211, 47)
HF_H1, r,z=(9, -21)
HF_H2, r,z=(13, -21)
HF_H3, r,z=(39, -21)
HF_H4, r,z=(152, -21)
q" (kW/m²)
Time (s)
Test 10
HF_V0, r,z=(178, -48)
HF_V1, r,z=(178, -14)
HF_V2, r,z=(178, 48)
HF_V3, r,z=(178, 109)
HF_V4, r,z=(178, 201)
HF_V5, r,z=(208, 47)
HF_V6, r,z=(214, 47)
HF_V7, r,z=(211, 47)
HF_H1, r,z=(9, -21)
HF_H2, r,z=(13, -21)
HF_H3, r,z=(39, -21)
HF_H4, r,z=(152, -21)
q" (kW/m²)
Time (s)
Test 11
HF_V0, r,z=(178, -48)
HF_V1, r,z=(178, -14)
HF_V2, r,z=(178, 48)
HF_V3, r,z=(178, 109)
HF_V4, r,z=(178, 201)
HF_V5, r,z=(208, 47)
HF_V6, r,z=(214, 47)
HF_V7, r,z=(211, 47)
HF_H1, r,z=(9, -21)
HF_H2, r,z=(13, -21)
HF_H3, r,z=(39, -21)
HF_H4, r,z=(152, -21)
q" (kW/m²)
Time (s)
Test 12
HF_V0, r,z=(178, -37)
HF_V1, r,z=(178, -3)
HF_V2, r,z=(178, 59)
HF_V3, r,z=(178, 120)
HF_V4, r,z=(178, 212)
HF_V5, r,z=(208, 58)
HF_V6, r,z=(214, 58)
HF_V7, r,z=(211, 58)
HF_H1, r,z=(9, -9)
HF_H2, r,z=(13, -9)
HF_H3, r,z=(39, -9)
HF_H4, r,z=(152, -9)
q" (kW/m²)
Time (s)

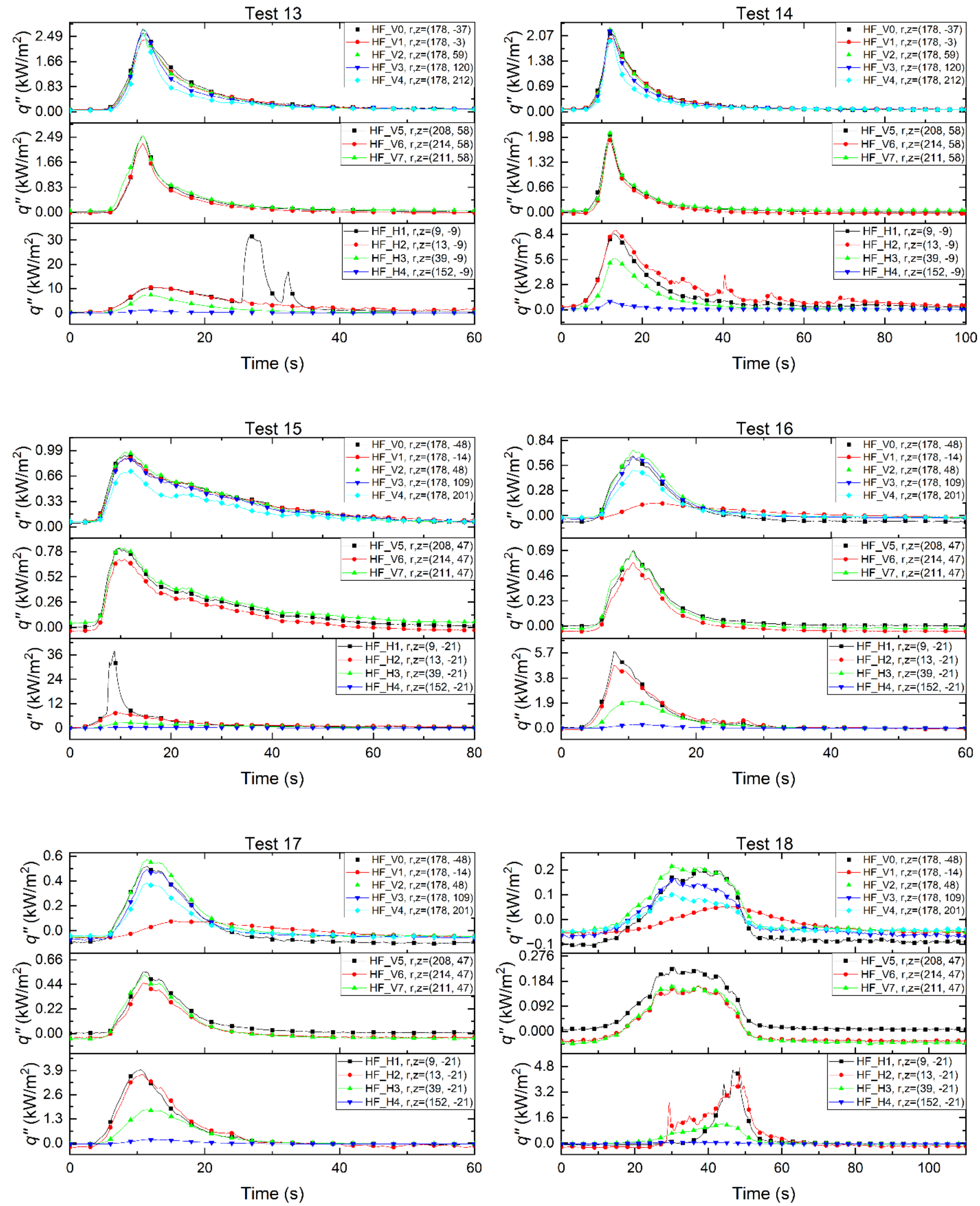
Test 13
HF_V0, r,z=(178, -37)
HF_V1, r,z=(178, -3)
HF_V2, r,z=(178, 59)
HF_V3, r,z=(178, 120)
HF_V4, r,z=(178, 212)
HF_V5, r,z=(208, 58)
HF_V6, r,z=(214, 58)
HF_V7, r,z=(211, 58)
HF_H1, r,z=(9, -9)
HF_H2, r,z=(13, -9)
HF_H3, r,z=(39, -9)
HF_H4, r,z=(152, -9)
q" (kW/m2)
Time (s)
Test 14
HF_V0, r,z=(178, -37)
HF_V1, r,z=(178, -3)
HF_V2, r,z=(178, 59)
HF_V3, r,z=(178, 120)
HF_V4, r,z=(178, 212)
HF_V5, r,z=(208, 58)
HF_V6, r,z=(214, 58)
HF_V7, r,z=(211, 58)
HF_H1, r,z=(9, -9)
HF_H2, r,z=(13, -9)
HF_H3, r,z=(39, -9)
HF_H4, r,z=(152, -9)
Test 15
HF_V0, r,z=(178, -48)
HF_V1, r,z=(178, -14)
HF_V2, r,z=(178, 48)
HF_V3, r,z=(178, 109)
HF_V4, r,z=(178, 201)
HF_V5, r,z=(208, 47)
HF_V6, r,z=(214, 47)
HF_V7, r,z=(211, 47)
HF_H1, r,z=(9, -21)
HF_H2, r,z=(13, -21)
HF_H3, r,z=(39, -21)
HF_H4, r,z=(152, -21)
Test 16
Test 17
Test 18

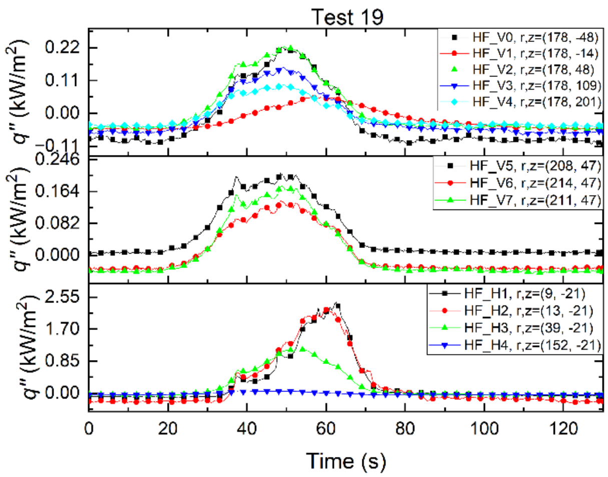
Test 19
HF_V0, r,z=(178, -48)
HF_V1, r,z=(178, -14)
HF_V2, r,z=(178, 48)
HF_V3, r,z=(178, 109)
HF_V4, r,z=(178, 201)
HF_V5, r,z=(208, 47)
HF_V6, r,z=(214, 47)
HF_V7, r,z=(211, 47)
HF_H1, r,z=(9, -21)
HF_H2, r,z=(13, -21)
HF_H3, r,z=(39, -21)
HF_H4, r,z=(152, -21)
q'' (kW/m²)
Time (s)

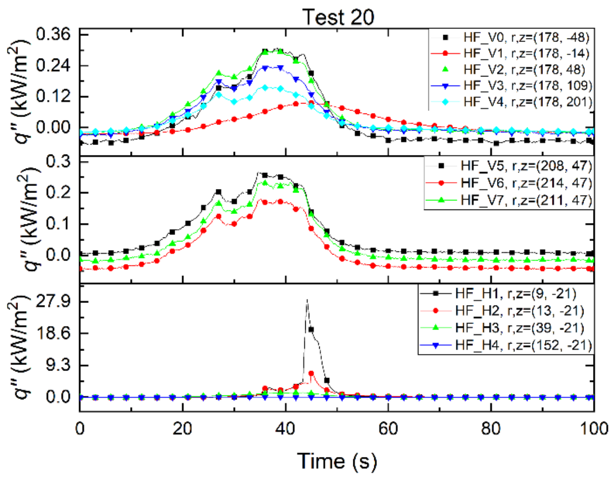
Test 20
HF_V0, r,z=(178, -48)
HF_V1, r,z=(178, -14)
HF_V2, r,z=(178, 48)
HF_V3, r,z=(178, 109)
HF_V4, r,z=(178, 201)
HF_V5, r,z=(208, 47)
HF_V6, r,z=(214, 47)
HF_V7, r,z=(211, 47)
HF_H1, r,z=(9, -21)
HF_H2, r,z=(13, -21)
HF_H3, r,z=(39, -21)
HF_H4, r,z=(152, -21)
q'' (kW/m²)
Time (s)

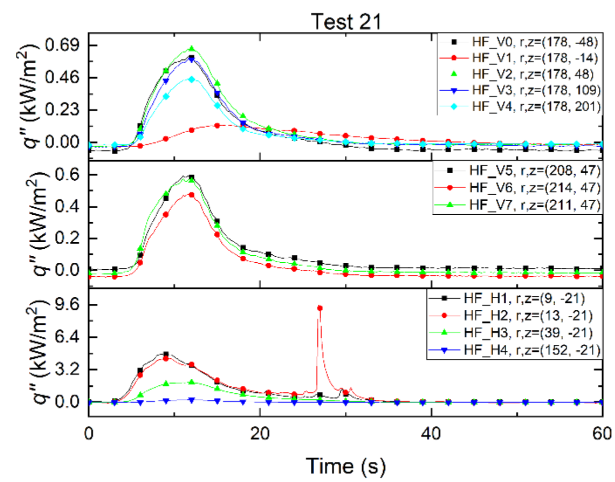
Test 21
HF_V0, r,z=(178, -48)
HF_V1, r,z=(178, -14)
HF_V2, r,z=(178, 48)
HF_V3, r,z=(178, 109)
HF_V4, r,z=(178, 201)
HF_V5, r,z=(208, 47)
HF_V6, r,z=(214, 47)
HF_V7, r,z=(211, 47)
HF_H1, r,z=(9, -21)
HF_H2, r,z=(13, -21)
HF_H3, r,z=(39, -21)
HF_H4, r,z=(152, -21)
q'' (kW/m²)
Time (s)

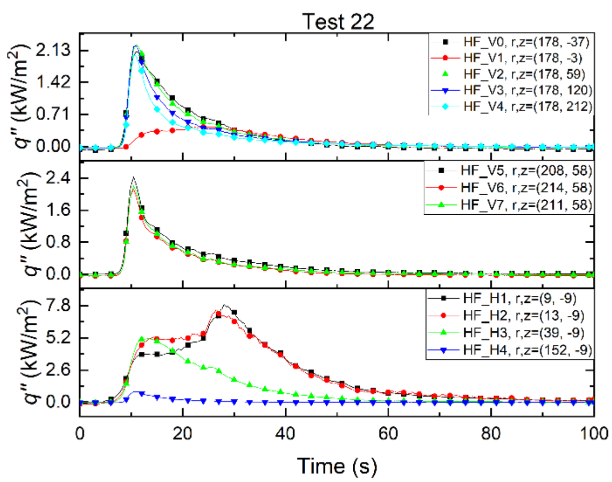
Test 22
HF_V0, r,z=(178, -37)
HF_V1, r,z=(178, -3)
HF_V2, r,z=(178, 59)
HF_V3, r,z=(178, 120)
HF_V4, r,z=(178, 212)
HF_V5, r,z=(208, 58)
HF_V6, r,z=(214, 58)
HF_V7, r,z=(211, 58)
HF_H1, r,z=(9, -9)
HF_H2, r,z=(13, -9)
HF_H3, r,z=(39, -9)
HF_H4, r,z=(152, -9)
q'' (kW/m²)
Time (s)

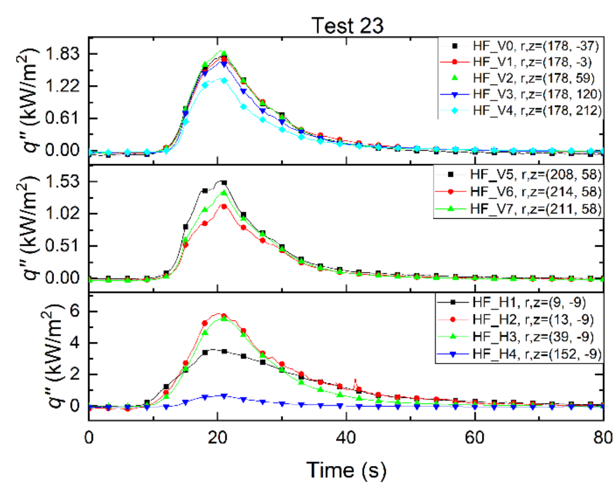
Test 23
HF_V0, r,z=(178, -37)
HF_V1, r,z=(178, -3)
HF_V2, r,z=(178, 59)
HF_V3, r,z=(178, 120)
HF_V4, r,z=(178, 212)
HF_V5, r,z=(208, 58)
HF_V6, r,z=(214, 58)
HF_V7, r,z=(211, 58)
HF_H1, r,z=(9, -9)
HF_H2, r,z=(13, -9)
HF_H3, r,z=(39, -9)
HF_H4, r,z=(152, -9)
q'' (kW/m²)
Time (s)

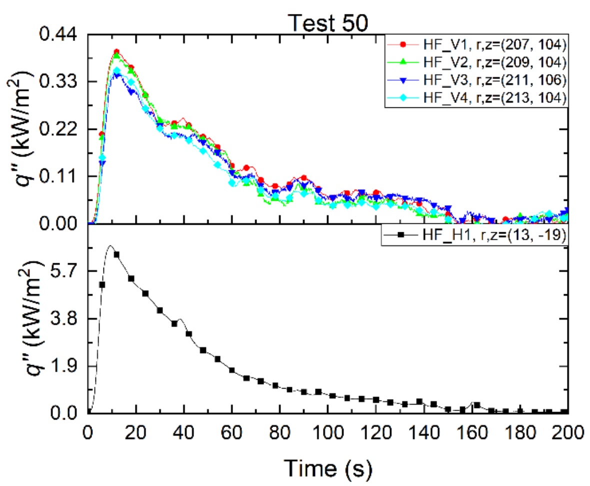
Test 50
HF_V1, r,z=(207, 104)
HF_V2, r,z=(209, 104)
HF_V3, r,z=(211, 106)
HF_V4, r,z=(213, 104)
HF_H1, r,z=(13, -19)
q'' (kW/m²)
Time (s)

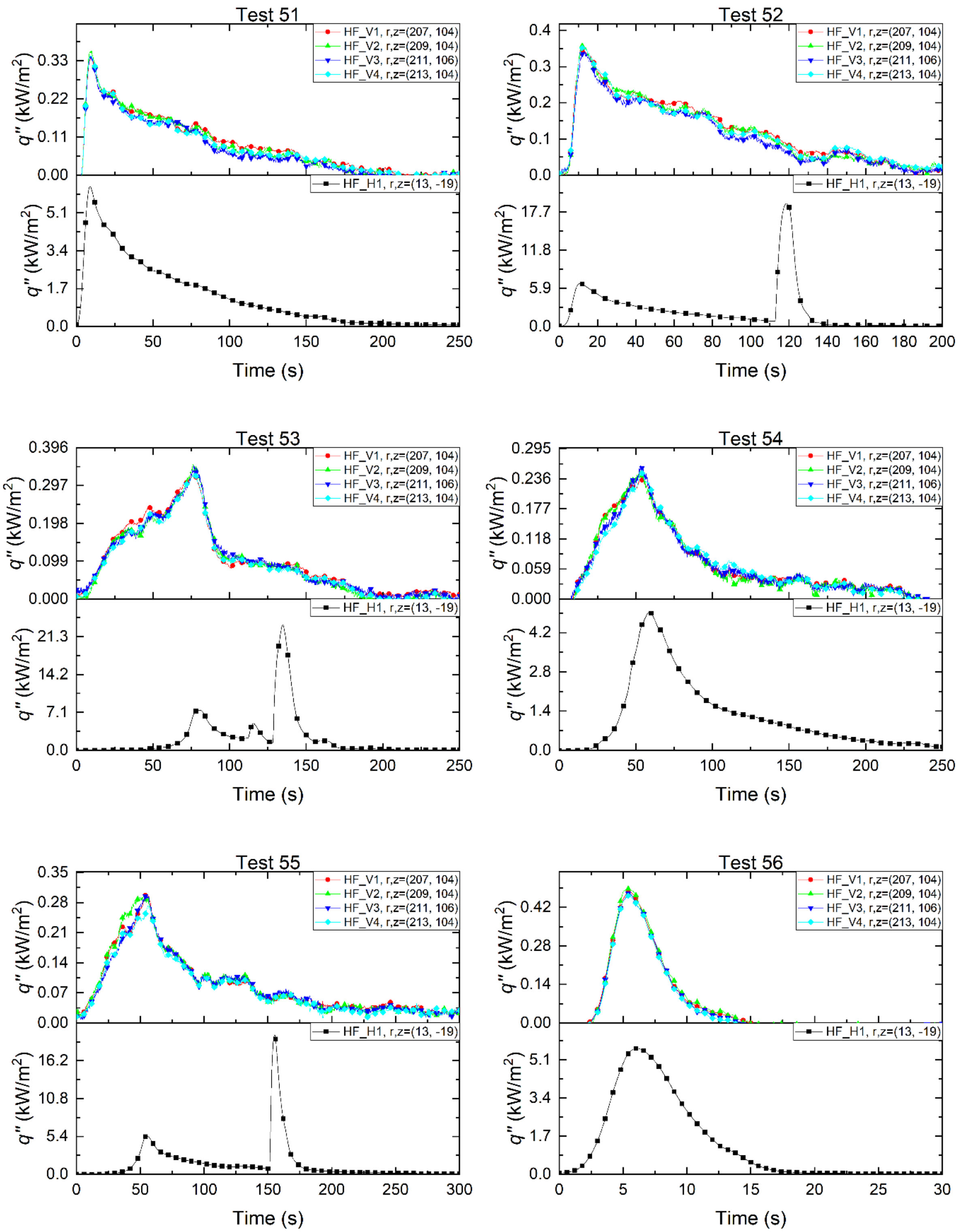

Fig. B6. The local heat flux to the surroundings measured under the 3 m x 3 m hood in Tests 1 to 23 and 50 to 56.

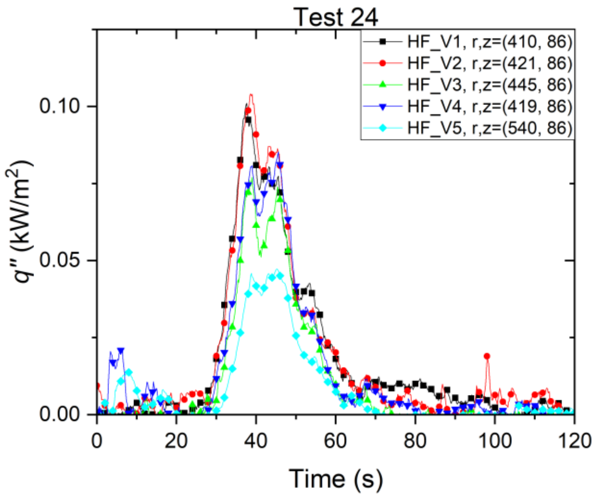
Test 24
HF_V1, r,z=(410, 86)
HF_V2, r,z=(421, 86)
HF_V3, r,z=(445, 86)
HF_V4, r,z=(419, 86)
HF_V5, r,z=(540, 86)
q'' (kW/m²)
Time (s)

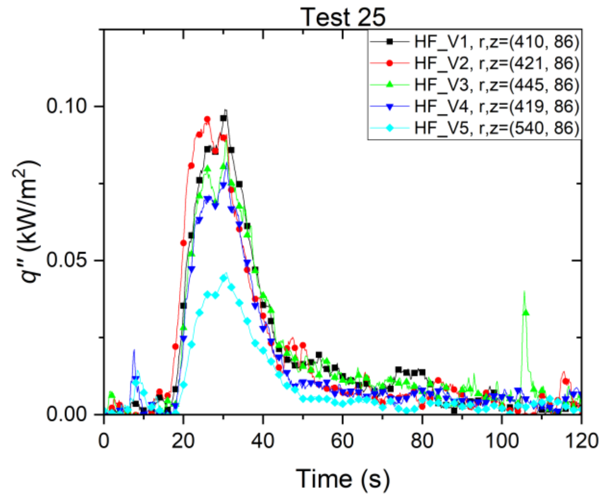
Test 25
HF_V1, r,z=(410, 86)
HF_V2, r,z=(421, 86)
HF_V3, r,z=(445, 86)
HF_V4, r,z=(419, 86)
HF_V5, r,z=(540, 86)
q'' (kW/m²)
Time (s)

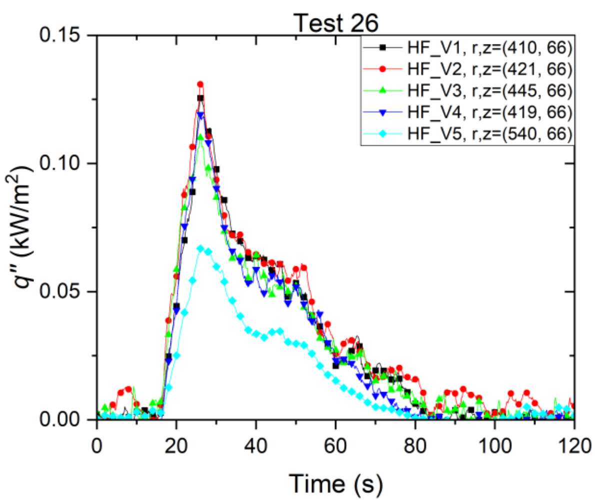
Test 26
HF_V1, r,z=(410, 66)
HF_V2, r,z=(421, 66)
HF_V3, r,z=(445, 66)
HF_V4, r,z=(419, 66)
HF_V5, r,z=(540, 66)
q'' (kW/m²)
Time (s)

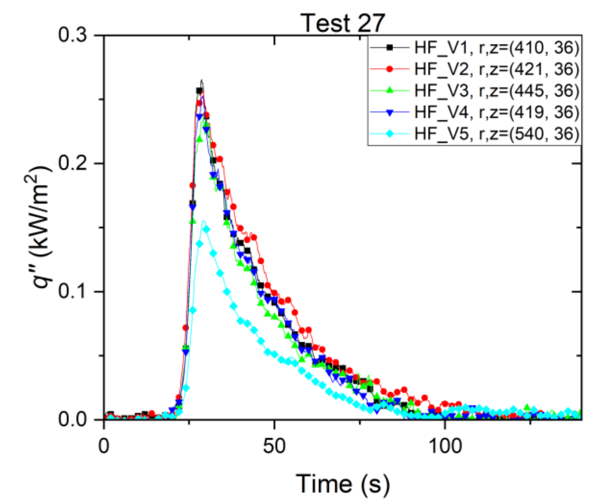
Test 27
HF_V1, r,z=(410, 36)
HF_V2, r,z=(421, 36)
HF_V3, r,z=(445, 36)
HF_V4, r,z=(419, 36)
HF_V5, r,z=(540, 36)
q'' (kW/m²)
Time (s)

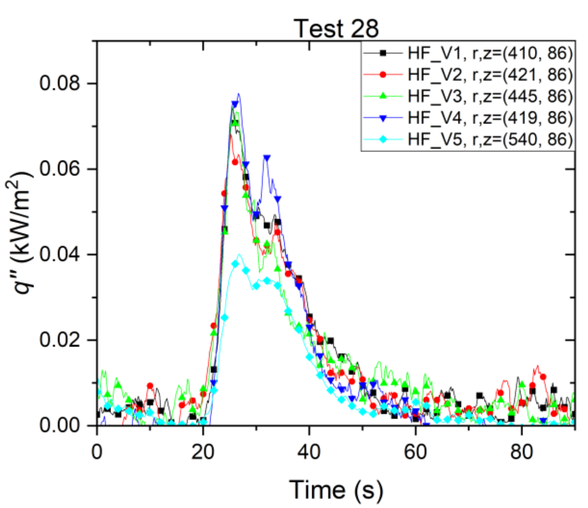
Test 28
HF_V1, r,z=(410, 86)
HF_V2, r,z=(421, 86)
HF_V3, r,z=(445, 86)
HF_V4, r,z=(419, 86)
HF_V5, r,z=(540, 86)
q'' (kW/m²)
Time (s)

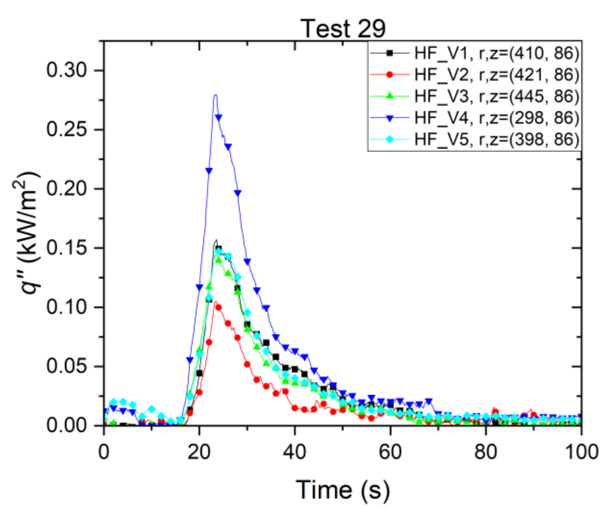
Test 29
HF_V1, r,z=(410, 86)
HF_V2, r,z=(421, 86)
HF_V3, r,z=(445, 86)
HF_V4, r,z=(298, 86)
HF_V5, r,z=(398, 86)
q'' (kW/m²)
Time (s)

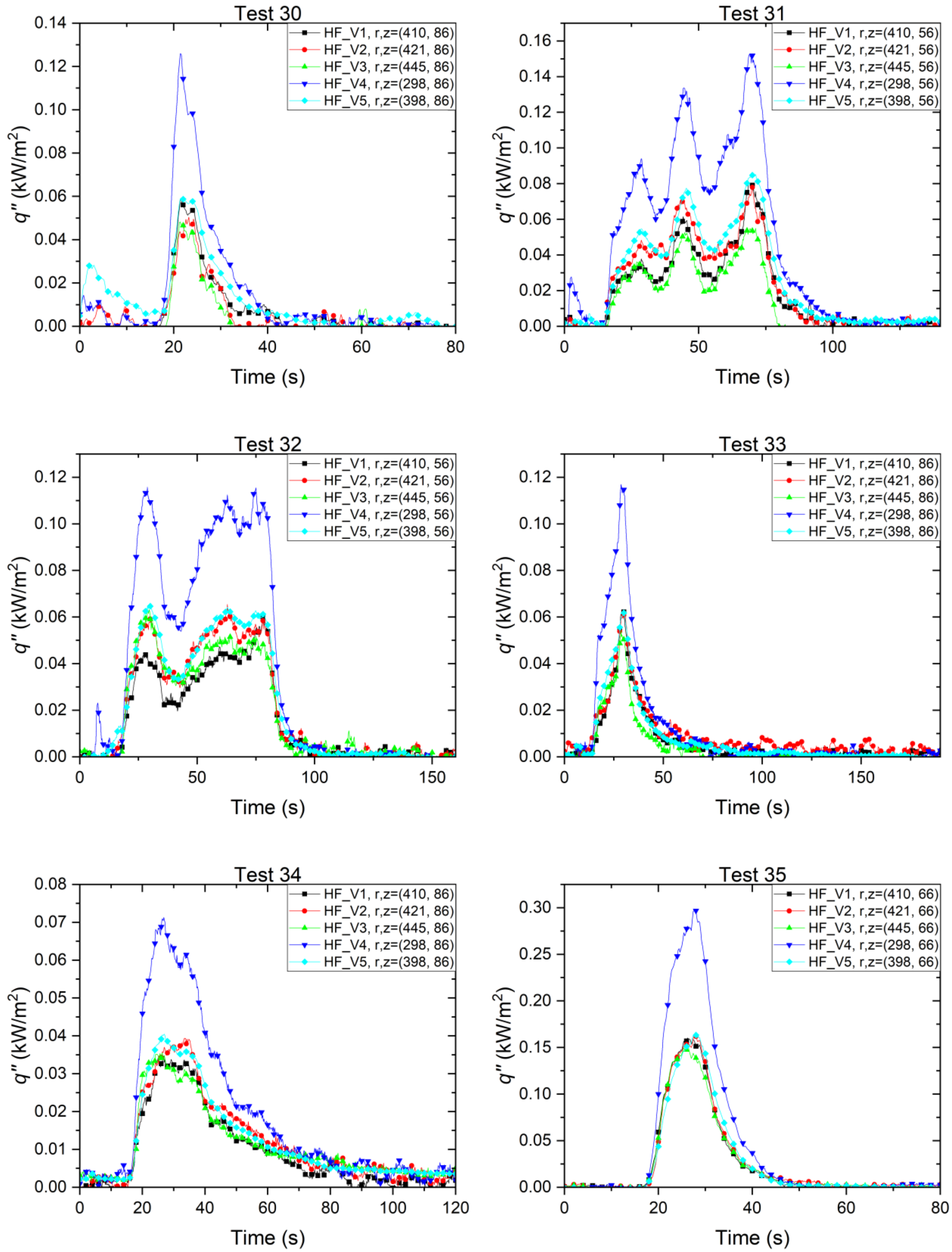
Test 30
HF_V1, r,z=(410, 86)
HF_V2, r,z=(421, 86)
HF_V3, r,z=(445, 86)
HF_V4, r,z=(298, 86)
HF_V5, r,z=(398, 86)
q'' (kW/m2)
Time (s)
Test 31
HF_V1, r,z=(410, 56)
HF_V2, r,z=(421, 56)
HF_V3, r,z=(445, 56)
HF_V4, r,z=(298, 56)
HF_V5, r,z=(398, 56)
q'' (kW/m2)
Time (s)
Test 32
HF_V1, r,z=(410, 56)
HF_V2, r,z=(421, 56)
HF_V3, r,z=(445, 56)
HF_V4, r,z=(298, 56)
HF_V5, r,z=(398, 56)
q'' (kW/m2)
Time (s)
Test 33
HF_V1, r,z=(410, 86)
HF_V2, r,z=(421, 86)
HF_V3, r,z=(445, 86)
HF_V4, r,z=(298, 86)
HF_V5, r,z=(398, 86)
q'' (kW/m2)
Time (s)
Test 34
HF_V1, r,z=(410, 86)
HF_V2, r,z=(421, 86)
HF_V3, r,z=(445, 86)
HF_V4, r,z=(298, 86)
HF_V5, r,z=(398, 86)
q'' (kW/m2)
Time (s)
Test 35
HF_V1, r,z=(410, 66)
HF_V2, r,z=(421, 66)
HF_V3, r,z=(445, 66)
HF_V4, r,z=(298, 66)
HF_V5, r,z=(398, 66)
q'' (kW/m2)
Time (s)

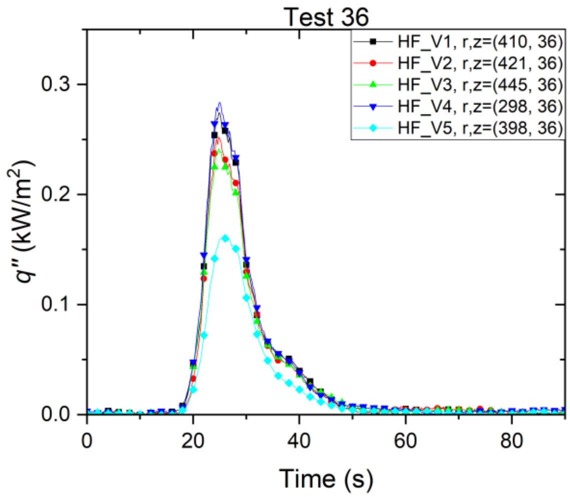
Test 36
HF_V1, r,z=(410, 36)
HF_V2, r,z=(421, 36)
HF_V3, r,z=(445, 36)
HF_V4, r,z=(298, 36)
HF_V5, r,z=(398, 36)
q'' (kW/m2)
Time (s)

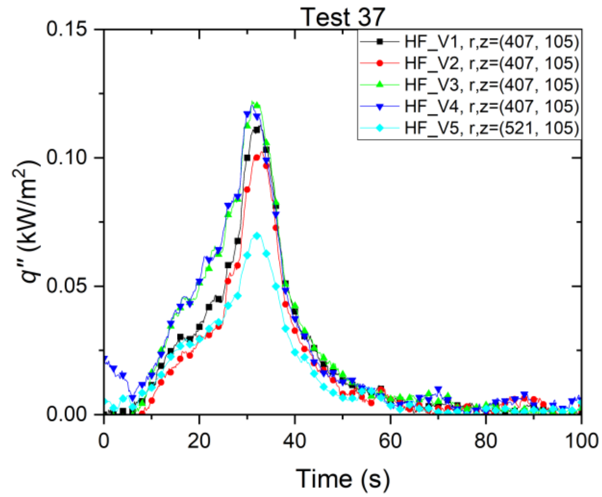
Test 37
HF_V1, r,z=(407, 105)
HF_V2, r,z=(407, 105)
HF_V3, r,z=(407, 105)
HF_V4, r,z=(407, 105)
HF_V5, r,z=(521, 105)
q'' (kW/m2)
Time (s)

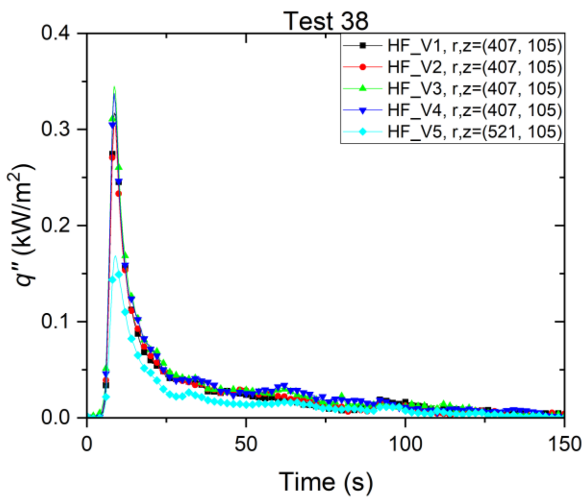
Test 38
HF_V1, r,z=(407, 105)
HF_V2, r,z=(407, 105)
HF_V3, r,z=(407, 105)
HF_V4, r,z=(407, 105)
HF_V5, r,z=(521, 105)
q'' (kW/m2)
Time (s)

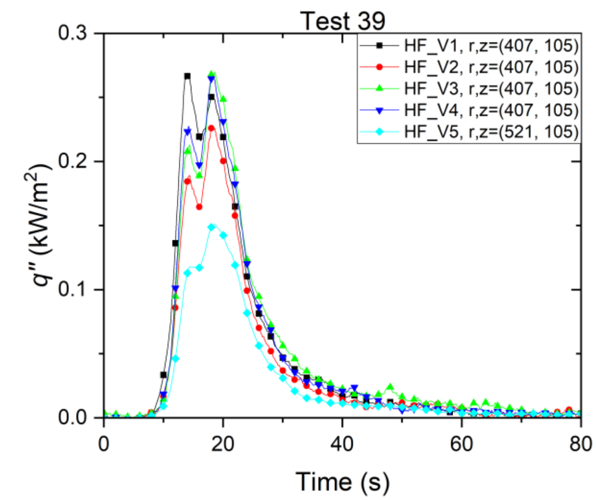
Test 39
HF_V1, r,z=(407, 105)
HF_V2, r,z=(407, 105)
HF_V3, r,z=(407, 105)
HF_V4, r,z=(407, 105)
HF_V5, r,z=(521, 105)
q'' (kW/m2)
Time (s)

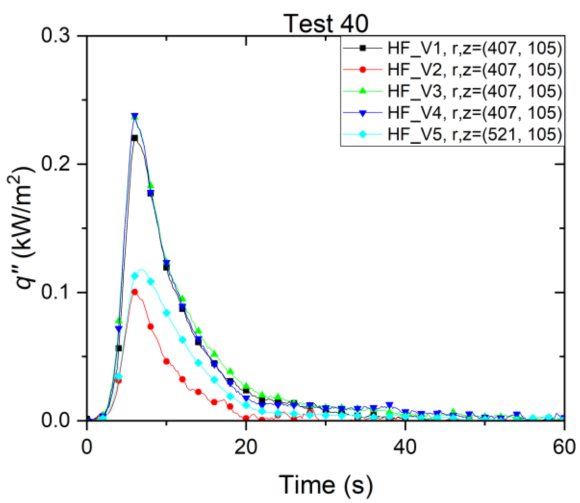
Test 40
HF_V1, r,z=(407, 105)
HF_V2, r,z=(407, 105)
HF_V3, r,z=(407, 105)
HF_V4, r,z=(407, 105)
HF_V5, r,z=(521, 105)
q'' (kW/m2)
Time (s)

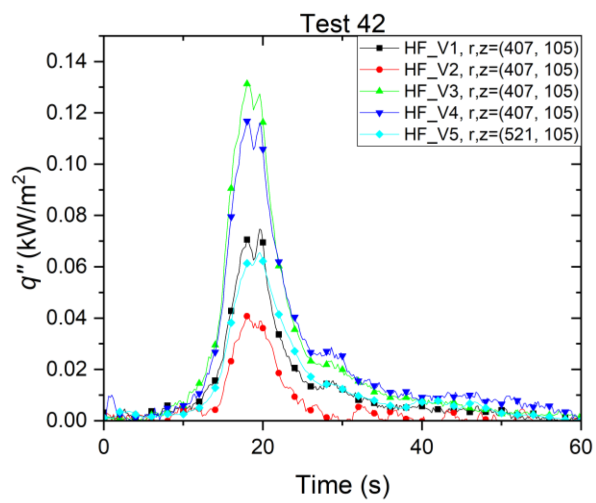
Test 42
HF_V1, r,z=(407, 105)
HF_V2, r,z=(407, 105)
HF_V3, r,z=(407, 105)
HF_V4, r,z=(407, 105)
HF_V5, r,z=(521, 105)
q'' (kW/m2)
Time (s)

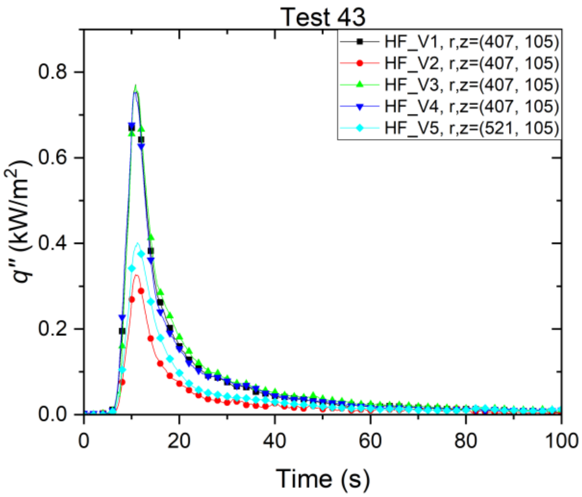
Test 43
HF_V1, r,z=(407, 105)
HF_V2, r,z=(407, 105)
HF_V3, r,z=(407, 105)
HF_V4, r,z=(407, 105)
HF_V5, r,z=(521, 105)
q" (kW/m2)
Time (s)

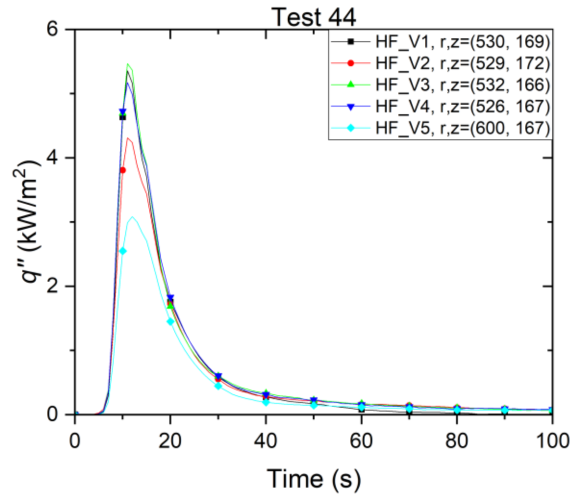
Test 44
HF_V1, r,z=(530, 169)
HF_V2, r,z=(529, 172)
HF_V3, r,z=(532, 166)
HF_V4, r,z=(526, 167)
HF_V5, r,z=(600, 167)
q" (kW/m2)
Time (s)

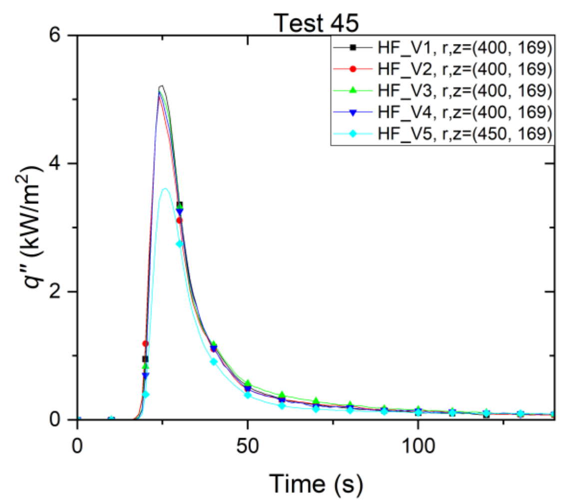
Test 45
HF_V1, r,z=(400, 169)
HF_V2, r,z=(400, 169)
HF_V3, r,z=(400, 169)
HF_V4, r,z=(400, 169)
HF_V5, r,z=(450, 169)
q" (kW/m2)
Time (s)

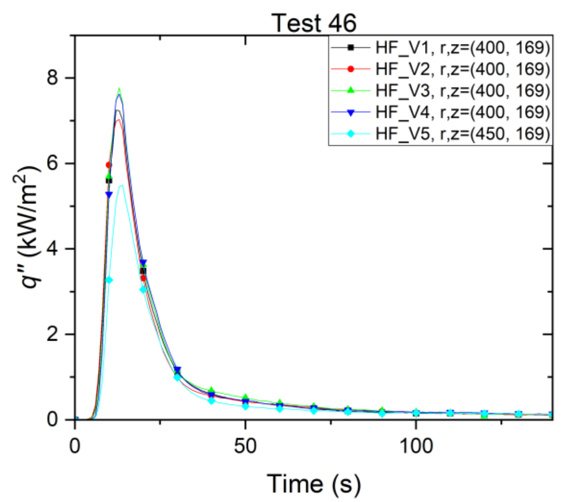
Test 46
HF_V1, r,z=(400, 169)
HF_V2, r,z=(400, 169)
HF_V3, r,z=(400, 169)
HF_V4, r,z=(400, 169)
HF_V5, r,z=(450, 169)
q" (kW/m2)
Time (s)

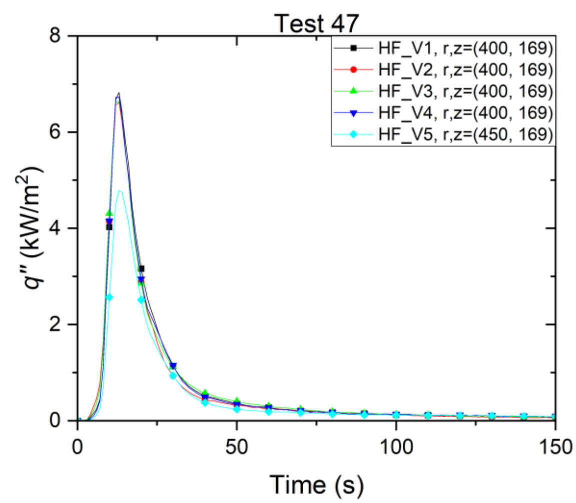
Test 47
HF_V1, r,z=(400, 169)
HF_V2, r,z=(400, 169)
HF_V3, r,z=(400, 169)
HF_V4, r,z=(400, 169)
HF_V5, r,z=(450, 169)
q" (kW/m2)
Time (s)

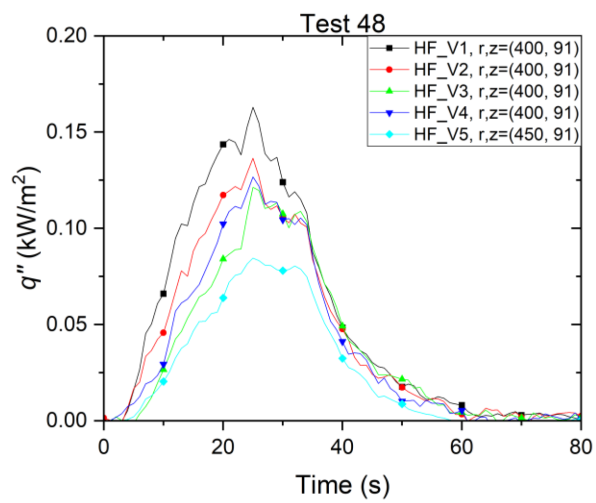
Test 48
HF_V1, r,z=(400, 91)
HF_V2, r,z=(400, 91)
HF_V3, r,z=(400, 91)
HF_V4, r,z=(400, 91)
HF_V5, r,z=(450, 91)
q" (kW/m2)
Time (s)

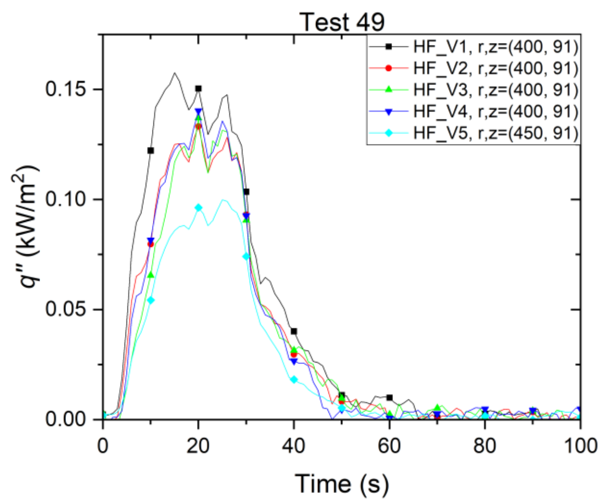

Fig. B7. The local heat flux to the surroundings measured under the 6 m x 6 m hood in Tests 24 to 49.

Appendix C. CO and Soot Yields Measurements

Table C1 lists the CO and soot yields for each test, with expanded uncertainty (k=2) sourced from the NIST Fire Calorimetry Database (FCD) [10].

Table C1. CO and Soot Yields measurements for each test, with expanded (k=2) uncertainty.

Test	Specimen	Y_{CO} (kg/kg x 10^{-3})	Y_{SOOT} (kg/kg x 10^{-3})
1	bluestem	88 ± 3	8.1 ± 1.5
2	bluestem	61 ± 3	2.0 ± 0.4
3	bluestem	57 ± 2	1.7 ± 0.3
4	bluestem	67 ± 3	1.4 ± 0.4
5	bluestem	58 ± 3	1.5 ± 1.0
6	bluestem	68 ± 3	2.5 ± 0.8
7	excelsior	31 ± 1	1.2 ± 0.2
8	excelsior	37 ± 1	1.1 ± 0.2
9	excelsior	30 ± 1	1.8 ± 0.3
10	excelsior	35 ± 1	1.8 ± 0.8
11	excelsior	39 ± 1	NA
12	Douglas fir	92 ± 4	NA
13	Douglas fir	70 ± 3	2.7 ± 0.4
14	Douglas fir	120 ± 5	2.6 ± 0.3
15	excelsior	32 ± 1	2.1 ± 0.4
16	excelsior	35 ± 1	2.3 ± 0.3
17	excelsior	40 ± 2	2.3 ± 0.5
18	excelsior	34 ± 1	1.4 ± 0.2
19	excelsior	40 ± 1	1.5 ± 0.3
20	excelsior	39 ± 2	1.5 ± 0.3
21	excelsior	39 ± 2	1.6 ± 0.3
22	Douglas fir	99 ± 4	3.5 ± 0.5
23	Douglas fir	99 ± 4	1.7 ± 0.2
24	bluestem	45 ± 4	1.7 ± 0.2
25	bluestem	54 ± 2	A
26	excelsior	27 ± 1	1.8 ± 1.3
27	excelsior	34 ± 2	0.52 ± 0.29
28	bluestem	46 ± 2	6.3 ± 5.8
29	bluestem	78 ± 5	4.5 ± 4.3
30	bluestem	42 ± 6	A
31	excelsior	19 ± 1	0.50 ± 1
32	excelsior	20 ± 2	1.7 ± 0.3
33	bluestem	62 ± 5	14 ± 10
34	bluestem	79 ± 8	21 ± 11
35	excelsior	25 ± 1	1.1 ± 0.6
36	excelsior	36 ± 2	0.90 ± 2

Test	Specimen	Y_{CO} (kg/kg x 10^{-3})	Y_{SOOT} (kg/kg x 10^{-3})
37	Douglas fir	85 ± 5	11 ± 16
38	Douglas fir	60 ± 2	3.9 ± 2.1
39	Douglas fir	58 ± 4	2.6 ± 1.6
40	Douglas fir	94 ± 6	1.8 ± 0.2
41	Douglas fir	78 ± 7	3.0 ± 17
42	Douglas fir	93 ± 5	4.8 ± 3.2
43	Douglas fir	73 ± 3	6.2 ± 1.8
44	Douglas fir	98 ± 4	4.4 ± 0.8
45	Douglas fir	100 ± 4	4.1 ± 2.3
46	Douglas fir	96 ± 4	5.3 ± 1
47	Douglas fir	110 ± 4	4.9 ± 0.9
48	excelsior	38 ± 2	A
49	excelsior	27 ± 2	A
50	excelsior	43 ± 6	15 ± 3.2
51	excelsior	85 ± 12	5.2 ± 1.1
52	excelsior	38 ± 5	6.0 ± 1.2
53	excelsior	49 ± 7	11 ± 2.1
54	excelsior	52 ± 7	13 ± 2.4
55	excelsior	54 ± 8	13 ± 2.5
56	excelsior	41 ± 38	1.4 ± 1.3

A. The value is below detectability.

Appendix D. Transient HRR, Radiative Heat Flux, and Optical Extinction Coefficient Measurements

The figures below show the HRR as a function of time (left axis). Also shown (right axis) are the radiative flux and the light extinction coefficient *K* for all of the tests.

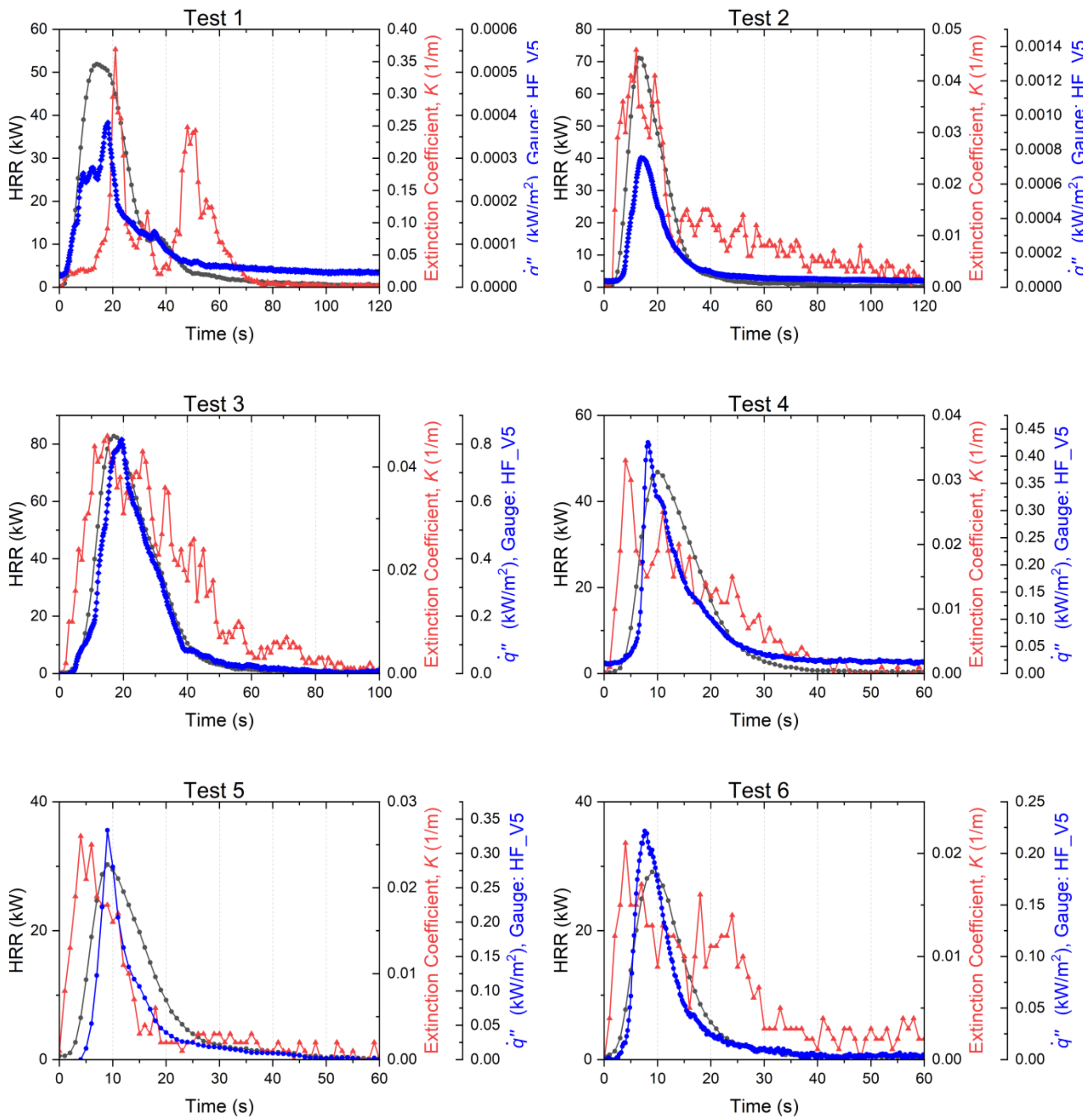

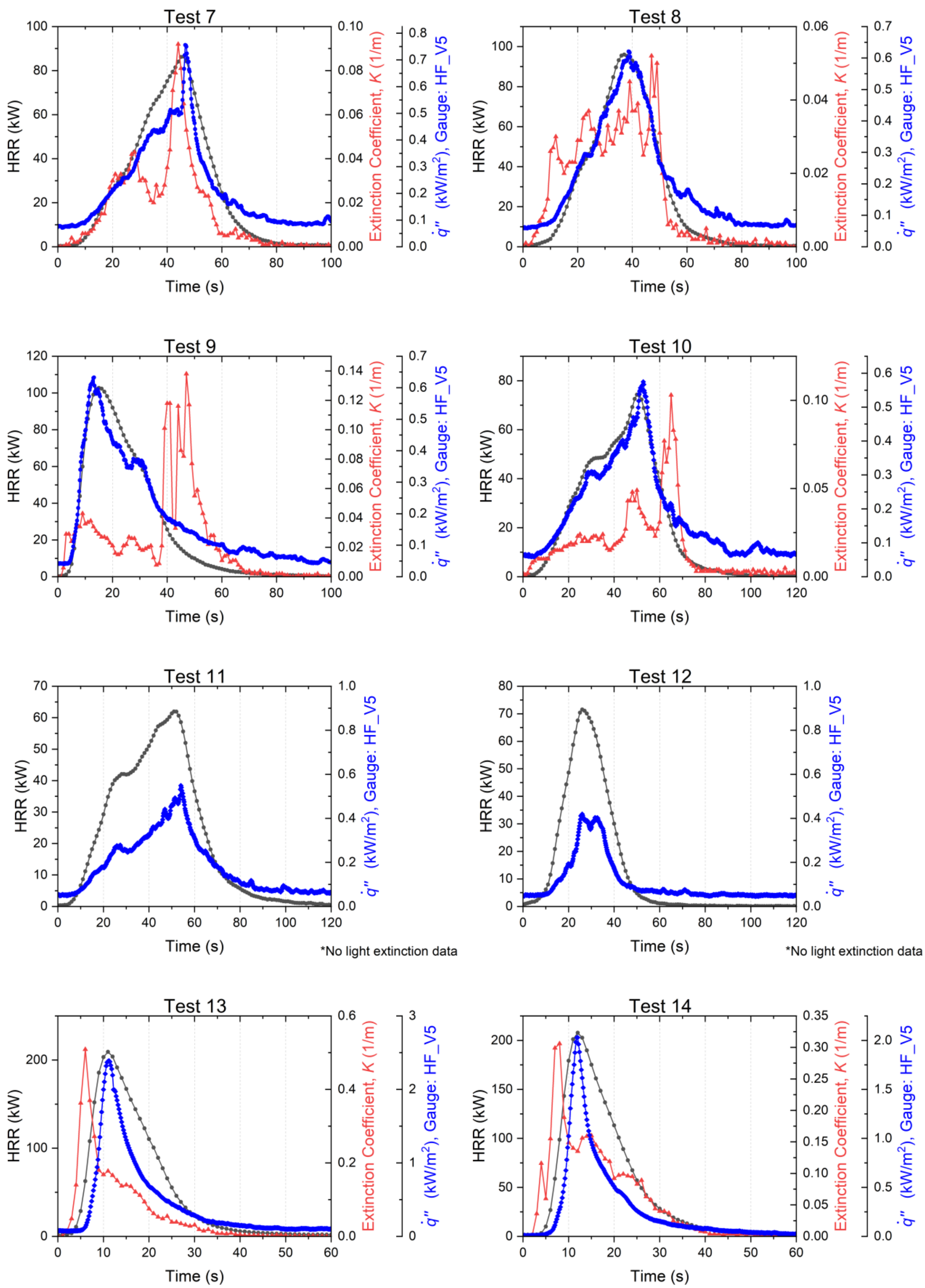
Test 7
Test 8
Test 9
Test 10
Test 11
Test 12
Test 13
Test 14
HRR (kW)
Time (s)
Extinction Coefficient, K (1/m)
$\dot{q}''$ (kW/m^2), Gauge: HF_V5
*No light extinction data
*No light extinction data

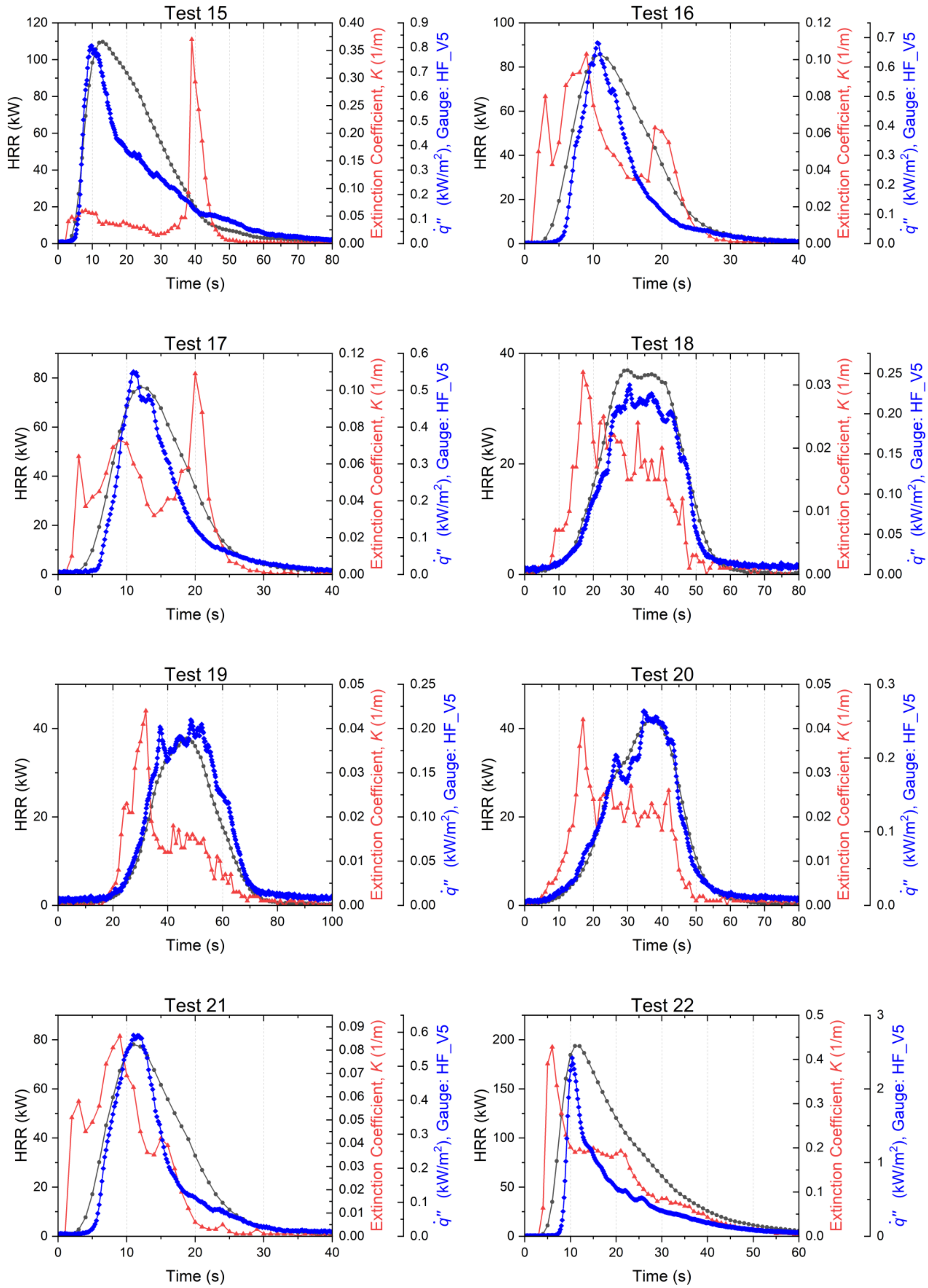
Test 15
Test 16
Test 17
Test 18
Test 19
Test 20
Test 21
Test 22
HRR (kW)
Time (s)
Extinction Coefficient, K (1/m)
$\dot{q}''$ (kW/m^2), Gauge: HF_V5

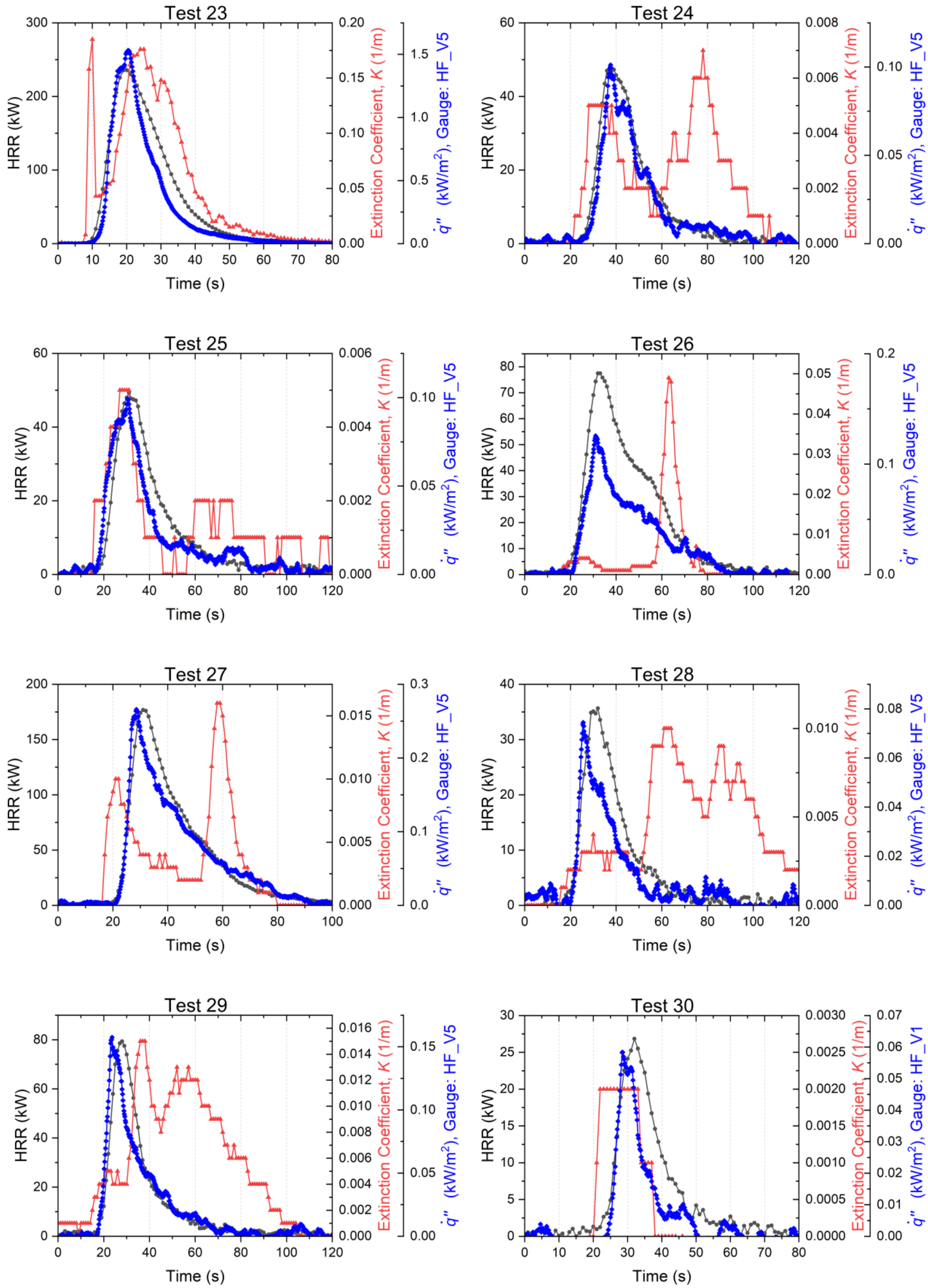
Test 23
Test 24
Test 25
Test 26
Test 27
Test 28
Test 29
Test 30
HRR (kW)
Time (s)
Extinction Coefficient, K (1/m)
q̇" (kW/m²), Gauge: HF_V5
q̇" (kW/m²), Gauge: HF_V1

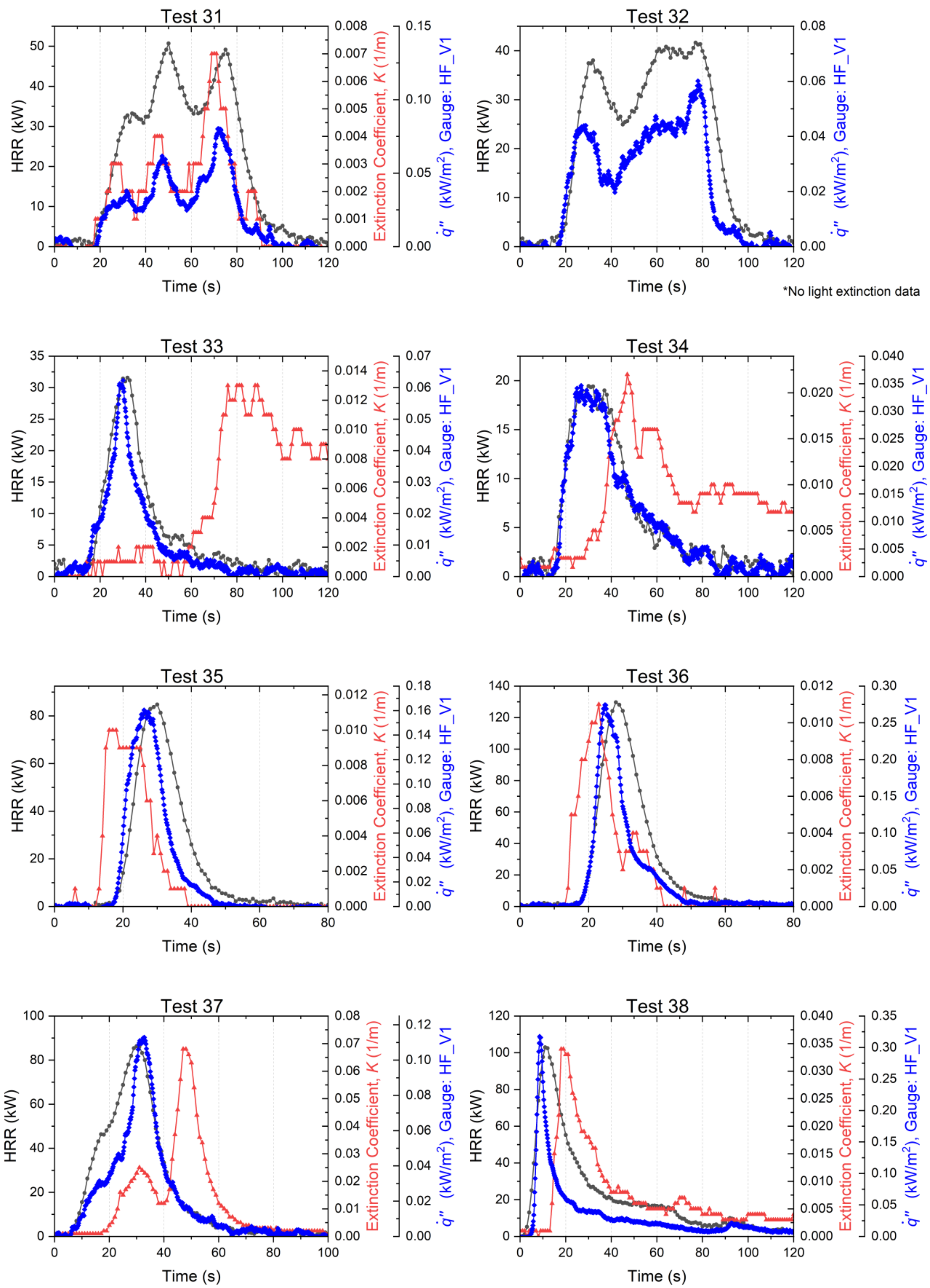
Test 31
Test 32
*No light extinction data
Test 33
Test 34
Test 35
Test 36
Test 37
Test 38
HRR (kW)
Time (s)
Extinction Coefficient, K (1/m)
q̇'' (kW/m²), Gauge: HF_V1

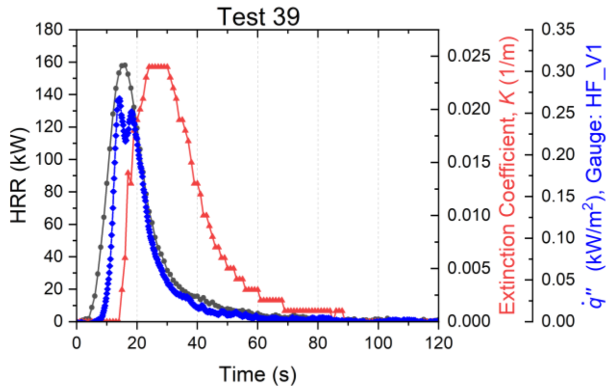
Test 39
HRR (kW)
Extinction Coefficient, K (1/m)
$\dot{q}''$ (kW/m^2), Gauge: HF_V1
Time (s)

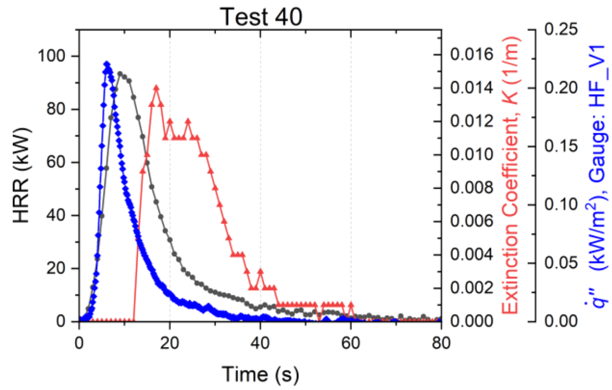
Test 40
HRR (kW)
Extinction Coefficient, K (1/m)
$\dot{q}''$ (kW/m^2), Gauge: HF_V1
Time (s)

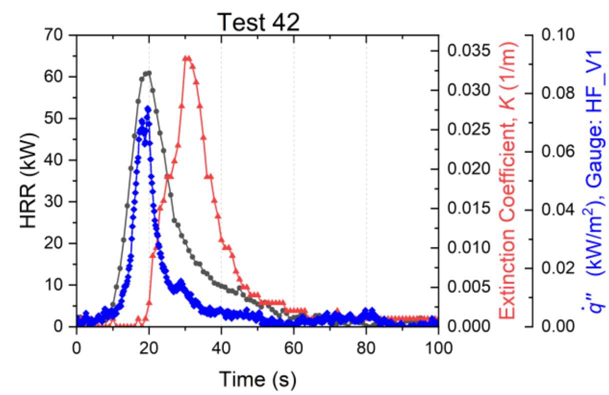
Test 42
HRR (kW)
Extinction Coefficient, K (1/m)
$\dot{q}''$ (kW/m^2), Gauge: HF_V1
Time (s)

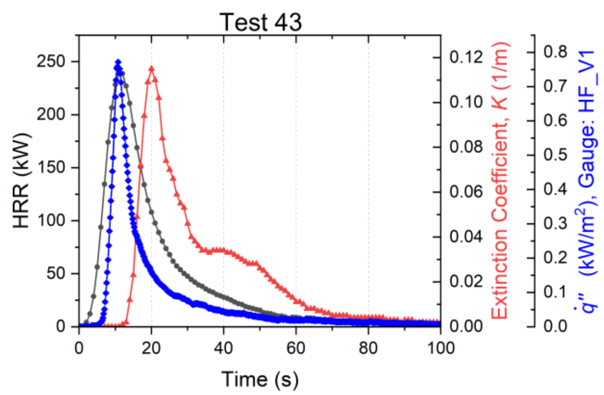
Test 43
HRR (kW)
Extinction Coefficient, K (1/m)
$\dot{q}''$ (kW/m^2), Gauge: HF_V1
Time (s)

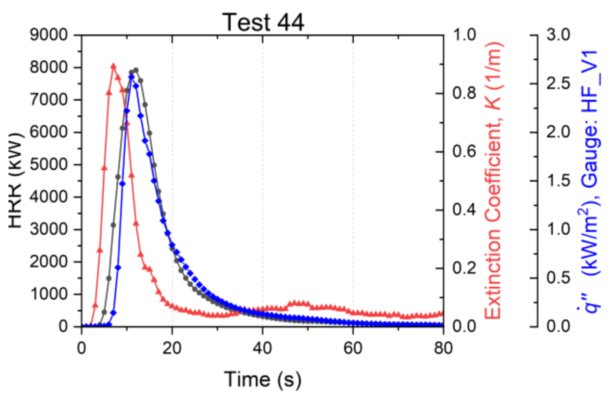
Test 44
HRR (kW)
Extinction Coefficient, K (1/m)
$\dot{q}''$ (kW/m^2), Gauge: HF_V1
Time (s)

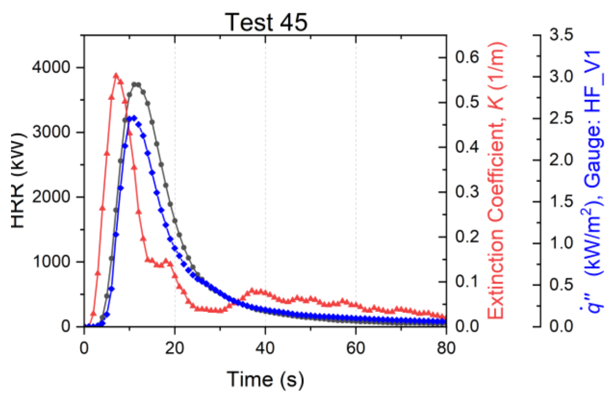
Test 45
HRR (kW)
Extinction Coefficient, K (1/m)
$\dot{q}''$ (kW/m^2), Gauge: HF_V1
Time (s)

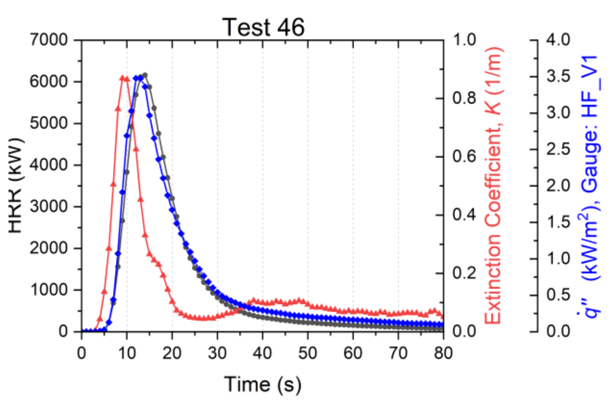
Test 46
HRR (kW)
Extinction Coefficient, K (1/m)
$\dot{q}''$ (kW/m^2), Gauge: HF_V1
Time (s)

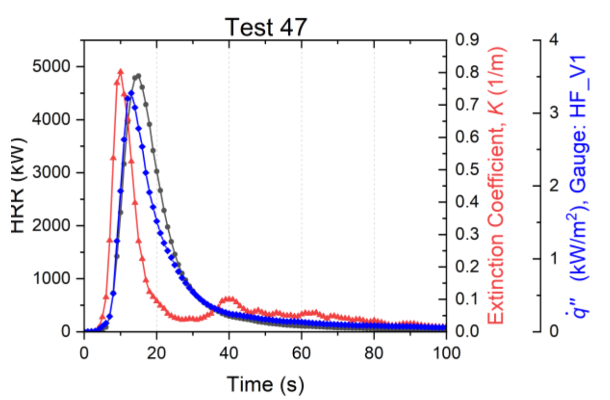
Test 47
HRR (kW)
Extinction Coefficient, K (1/m)
$\dot{q}''$ (kW/m^2), Gauge: HF_V1
Time (s)

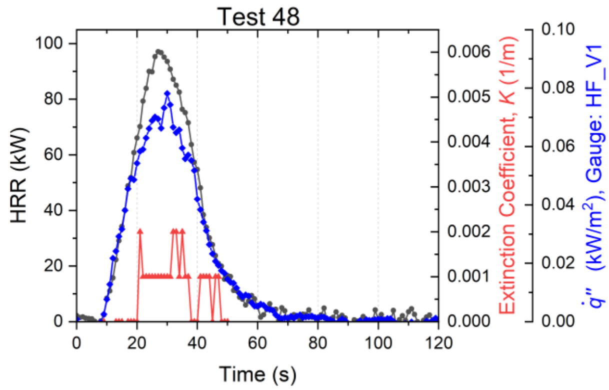
Test 48
HRR (kW)
Extinction Coefficient, K (1/m)
q̇'' (kW/m²), Gauge: HF_V1
Time (s)

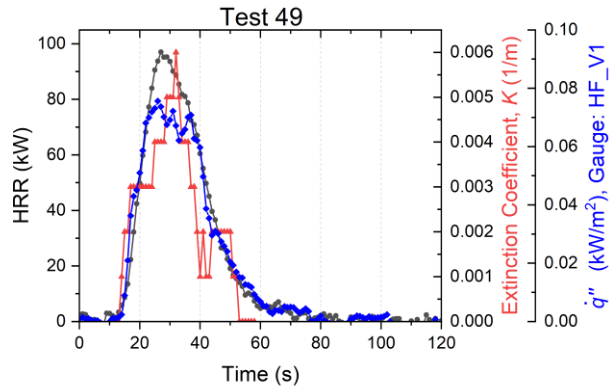
Test 49
HRR (kW)
Extinction Coefficient, K (1/m)
q̇'' (kW/m²), Gauge: HF_V1
Time (s)

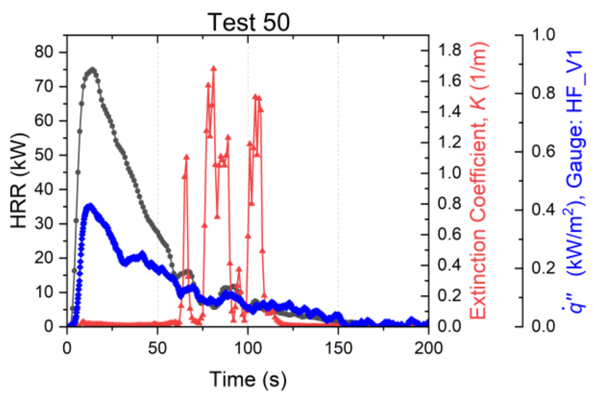
Test 50
HRR (kW)
Extinction Coefficient, K (1/m)
q̇'' (kW/m²), Gauge: HF_V1
Time (s)

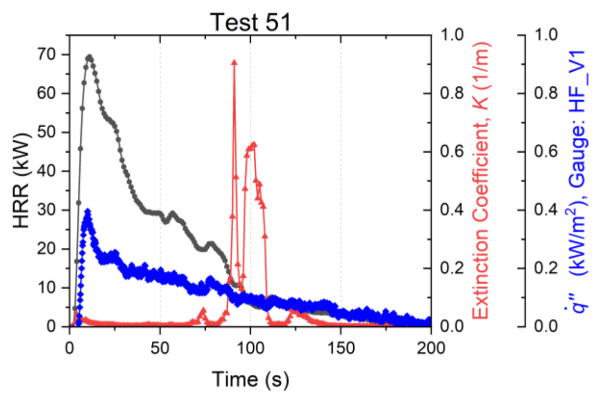
Test 51
HRR (kW)
Extinction Coefficient, K (1/m)
q̇'' (kW/m²), Gauge: HF_V1
Time (s)

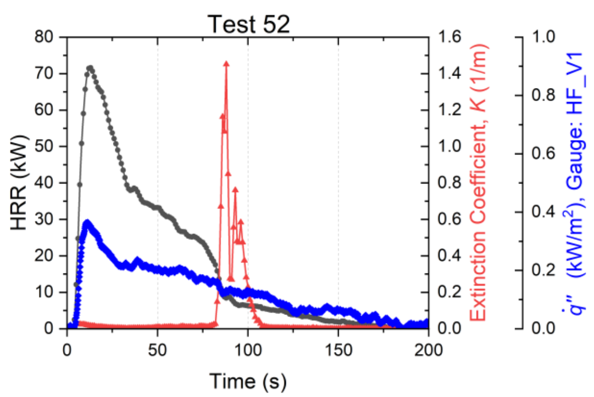
Test 52
HRR (kW)
Extinction Coefficient, K (1/m)
q̇'' (kW/m²), Gauge: HF_V1
Time (s)

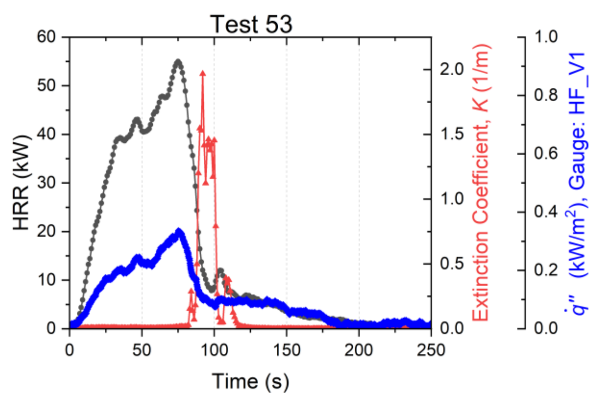
Test 53
HRR (kW)
Extinction Coefficient, K (1/m)
q̇'' (kW/m²), Gauge: HF_V1
Time (s)

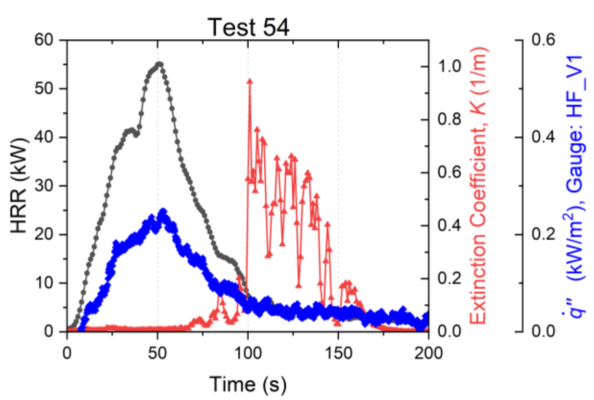
Test 54
HRR (kW)
Extinction Coefficient, K (1/m)
q̇'' (kW/m²), Gauge: HF_V1
Time (s)

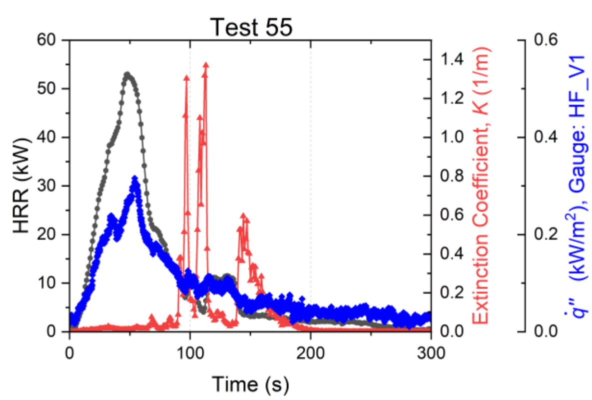
Test 55
HRR (kW)
Extinction Coefficient, K (1/m)
q̇'' (kW/m²), Gauge: HF_V1
Time (s)

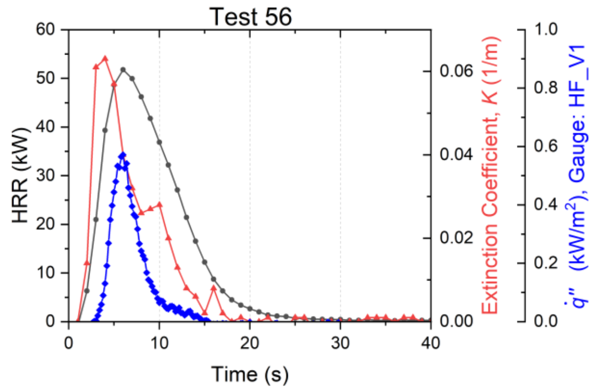

Fig. D1. Heat release rate as a function of time (left axis), with the radiative heat flux ($\dot{q}''$) and light extinction coefficient (K) shown on the right axis.